# TOWARD A NOVEL TISSUE ENGINEERING METHOD FOR REPAIRING CRITICALLY SIZED CRANIOFACIAL BONE DEFECTS

by

Ben Pen Jui Hung

A dissertation submitted to the Johns Hopkins University in conformity with the requirements for the degree Doctor of Philosophy

Baltimore, Maryland

March 2016

# Abstract

Non-healing craniofacial bone defects are a major clinical problem. Tissue engineering has the potential to provide a next-generation solution, but specific focus on clinical translatable technologies is needed. A translatable approach combining using enhanced bone marrow and decellularized trabecular bone scaffolds is first investigated. The drawbacks of this approach, including difficulty of scaffold production and invasive cell harvesting, prompted the development of a new approach in which 3D printing of scaffolds is combined with adipose-derived stem cells signaled with platelet-derived growth factor BB. 3D printing was successfully used to create porous, anatomically shaped scaffolds with polycaprolactone. The lack of osteoinductive properties of polycaprolactone was addressed by development of a hybrid material consisting of bone extracellular matrix particles embedded in polycaprolactone and this material was demonstrated to be both printable and bioactive. Platelet-derived growth factor BB was examined as a suitable biomolecule for bone engineering by investigation of its osteoinductive effects on both marrow-derived and adipose-derived mesenchymal stem cells. Platelet-derived growth factor BB was found to be osteoinductive to adipose-derived but not to marrow-derived mesenchymal stem cells with both correlative and loss-of-function evidence, the latter of which made use of a reducible delivery vehicle developed specifically for siRNA delivery. Finally, the fate of transplanted cells is addressed by investigation of chemical exchange saturation transfer magnetic resonance imaging, found to be suitable for non-invasive and longitudinal in vivo monitoring.

# Thesis committee

**Warren L. Grayson, PhD** (*primary advisor, reader*)

Associate Professor, Department of Biomedical Engineering

Johns Hopkins University School of Medicine

**Jordan J. Green, PhD**

Associate Professor, Department of Biomedical Engineering

Johns Hopkins University School of Medicine

**Jennifer H. Elisseeff, PhD**

Professor, Department of Biomedical Engineering

Johns Hopkins University School of Medicine

**Amir H. Dorafshar, MBChB** (*reader*)

Associate Professor, Department of Plastic and Reconstructive Surgery

Johns Hopkins University School of Medicine

**Assaf A. Gilad, PhD**

Associate Professor, Department of Radiology

Johns Hopkins University School of Medicine

# Acknowledgments

A complete list of everyone I'd like to acknowledge is nigh-impossible. So many people have offered their support over the years I've studied at Johns Hopkins, and this work would not have been remotely possible without them all. That being said, I would still like to highlight a few key figures during my doctoral journey.

I had the good fortune of working with many talented and friendly people in the Grayson Lab for Craniofacial and Orthopaedic Tissue Engineering. I would like to thank two post-doctoral fellows, Dr. Pinar Yilgor Huri and Dr. Christina Holmes, for their advice and wisdom. The first doctoral student to graduate from the lab, Dr. Daphne Hosmane, was instrumental both directly and indirectly to the outcomes of my thesis. I would also like to acknowledge Erin Salter and Colin Cook, our two graduated Master's students, for both their advice and their friendship. It was also a pleasure working with the many undergraduate students in the lab, most notably Josh Temple, Miguel Dias, and Bilal Naved. I greatly appreciate their tireless efforts and I wish them the best. As for the other doctoral students – Justin Morrissette-McAlmon, Jordie Gilbert-Honick, Ethan Nyberg, Sarah Somers, Lexi Rindone, and Ashley Farris – I thank you for your help and support and hope your careers thrive after this thesis is complete.

Outside the Grayson lab, I collaborated a great many wonderful people whom I want to acknowledge here. In the Green Group, I was fortunate to work with Dr. Stephany Tzeng, Dr. Corey Bishop, and Kristen Kozielski – these three talented individuals were great collaborators and amazing friends. In the early part of my doctoral studies, I worked with Dr. Sol Mundinger and Dr. Xiaofeng Jia, both of whom spent much time giving me advice and hands-on help with my studies. In the later years of my

doctoral studies, I worked with Dr. Ethel Ngen and Dr. Lina Alon, who also spent time and effort helping me get my last block of experiments off the ground.

Next, I would of course like to acknowledge my thesis committee – Dr. Warren Grayson, Dr. Jordan Green, Dr. Jennifer Elisseeff, Dr. Amir Dorafshar, and Dr. Assaf Gilad. Their guidance throughout my doctoral years was instrumental not only to my degree, but also to my maturation as a scientist and engineer. I learned much during my time at Johns Hopkins and I hope to make my committee proud as I leave.

I am also very grateful to my funding sources during my doctoral years. My last two years were supported by the NIH Ruth L. Kirschstein National Research Service Award F31 DE024922 and the Russell Military Scholar Award.

Finally, I must thank my family and friends. My parents, as always, encouraged me throughout my studies and never lost faith in my future. My extended family, though across the world from me, never ceased to offer their support in my endeavors. And I am certain I could never have completed this work without the support of my friends, both old and new, both near and far. I am ever grateful for their friendship.

# Table of contents

# List of tables

# List of figures

# Chapter 1: introduction

This chapter draws from the following publications: (1) Nyberg EL, Farris AL, Hung BP, Dias M, Garcia JR, Dorafshar AH, and Grayson WL. 2016. "3D-printing technologies for craniofacial rehabilitation, reconstruction, and regeneration." (under review); (2) Hung BP, Salter EK, Temple JP, Mundinger GS, Brown EN, Brazio P, Rodriguez ED, and Grayson WL. 2013. "Engineering bone grafts with enhanced bone marrow and native scaffolds." Cells Tissues Organs 198: 87-98.

## 1.1. Craniofacial bone defects

Craniofacial defects arise as a direct result of trauma [1, 2], oncological resection, or congenital differences (e.g. cleft lip [3]). They result in soft tissue or bone deficits, or as a combination of both leading to composite tissue defects. For bone specifically, a critically sized defect is defined as 2 cm or larger in humans; a defect 6 cm or larger requires a vascularized implant [4-6]. Such defects significantly impact the patient's quality of life. Non-healing defects in the calvarial region compromise the ability of the skull to protect the brain and mandibular defects compromise the patient's ability to speak and eat. Craniofacial bones also give the face its shape and structure; therefore, craniofacial bone defects lead to compromised facial aesthetics and negatively impact the individual's psychosocial well-being. Approximately one million fractures requiring bone transplantation occur annually in the United States, with more than 200000 of these in the craniofacial region [7]. These incur an annual economic burden in excess of $3 billion [7]. As such, there is a large need for a treatment modality for such defects.

1.2. Current treatments for craniofacial bone defects

Several methods and strategies have emerged currently to treat critically sized craniofacial bone defects; however, each has its own limitations. For small cases, local tissue rearrangement may be used [8]. This method is generally insufficient, however, for the large defects discussed here. Another technique that can be used for reconstruction of defects in the craniofacial region is grafting: transferring a particular tissue type from one area of the body to another without a blood supply. The lack of blood supply causes increased susceptibility to infection and resorption and necessitates a well-vascularized recipient region. In cases of even larger defects, microsurgical transfer of tissue containing its own vascular supply is the technique of choice [9, 10]. The advantage of this technique is that an adequate supply of well-vascularized tissue can be transferred, which can better withstand infection and resorption especially in the more hostile recipient bed. The disadvantages of these techniques are that they do not exactly match the recipient structures. For example, the current gold standard in surgical reconstruction, the transfer of a fibula bone as a vascularized bone flap [11, 12], never matches exactly to a maxilla or mandible to retain normal structure and function.

Prosthetic materials, such as titanium [13], bioglasses [14-17], and bio-inert plastics [18], may be used in cases where successful surgical reconstruction is not a viable option. These materials generally feature biocompatibility, appropriate mechanical properties, and the ability to be 3D-printed into anatomical shapes to fit the craniofacial skeleton. Despite these myriad prosthetics, however, this strategy also has several key drawbacks. The synthesis of some bio-inert plastics, such as poly[methyl methacrylate] (PMMA), occurs under highly exothermic conditions, which may lead to tissue necrosis

around the area of implantation [19]. The use of metals, such as titanium, carries with it high costs and low osseous integration [20]. In general, prosthetic implants have also been associated with soft tissue necrosis adjacent to the implantation site. Additionally, the use of prosthetic implants in younger patients, whose bones continue to grow, necessitates multiple surgeries over time. These considerations prompt the development of a next-generation method for treating critically sized craniofacial bone defects.

### 1.3. Tissue engineering for craniofacial defects

Tissue engineering holds the potential to overcome the various challenges associated with surgical reconstruction and use of prosthetics. In the classical tissue engineering paradigm, cells are housed in a scaffold and signaled with bioactive factors [21]. The cells regenerate tissue as signaled by the bioactive factors, while the scaffold provides structural and geometric support. This would result in the rebuilding of native tissue without the use of autografts, greatly reducing donor-site morbidity. An appropriately shaped scaffold would match the required geometry of the defect rather than restrict the clinician to the geometry of other, non-matching anatomical sites such as the fibula. Finally, a successful tissue engineered construct is biologically active and would grow and adapt with the patient, a feat metal and plastic prosthetics cannot achieve.

For bone engineering, several components have been widely studied. For scaffolds, this is the decellularized trabecular bone (DCB) scaffold. The most widely studied cell type is the marrow-derived mesenchymal stem cell (MSC). Finally, the most osteoinductive biomolecule known is bone morphogenetic protein 2 (BMP2).

*1.3.1. Decellularized trabecular bone scaffolds*

DCB scaffolds have been widely investigated for bone engineering applications due to osteoinductive cues present within the matrix, namely BMP2 [22, 23], as well as its mechanical properties [24]. Decellularized and demineralized bone scaffolds have also been used in conjunction with MSCs to great effect in creating bone [25, 26] and osteochondral [27-29] constructs. These scaffolds can also be milled into customized, patient-specific geometries, making them useful for complex bone defects such as those found in the craniofacial skeleton [30].

*1.3.2. Marrow-derived mesenchymal stem cells*

While primary osteoblasts are the main bone-forming cell type in bone, obtaining clinically relevant numbers of osteoblasts to populate and grow replacement tissue is a challenge. This is why investigators have studied progenitor populations, especially the MSC, in detail. It was shown in a well-known study by Pittenger et al. [31] that MSCs can (1) differentiate into bone-forming cells, staining positive for mineral formation via Alizarin Red S; and (2) be expanded clonally without loss of potency to a greater extent than can primary mature cell types, allowing for the population of large constructs as would be found clinically.

MSCs are isolated from bone marrow aspirate and are characterized by positive CD44 (receptor for a variety of ligands, such as hyaluronic acid and collagen), CD73 (enzyme that converts nucleotides to nucleosides), CD90 (marker for thymocytes), and CD105 (part of the transforming growth factor (TGF) β1) expression; at the same time

they are negative for CD34 (hematopoietic marker involved in cell-cell adhesion), CD45 (hematopoietic marker involved in lymphocyte receptor signaling), and the major histocompatibility complex class II [32-35]. One drawback to MSC use is the fairly rare occurrence of MSCs in bone marrow; MSCs comprise less than 0.01% of the nucleated population. As such, there is interest in developing new methods of concentrating the MSC population in harvested tissue. One method of accomplishing this is discussed in Chapter 2.

### *1.3.3. Bone morphogenetic proteins*

BMPs were first discovered by characterization of the osteoinductive properties of demineralized bone extract [22, 23, 36], prompted by the observation that demineralized bone matrix promoted ectopic bone formation when implanted intramuscularly in rabbits. Since then, they have been widely investigated in experimental models. MSCs engineered to express BMP2 in conjunction with vascular progenitors were able to induce vascularized bone regeneration in a critically sized rat calvarial defect [37]. In another study, BMP2 incorporated into electrospun nanofibers enhanced scaffold osteoinductivity in terms of regenerated bone within 8 weeks post-implantation, also in rat calvarial defects [38]. Importantly, BMP2 and BMP7 have undergone clinical trials [39] and been approved for clinical use [40, 41]; however, their use necessitates injection of supraphysiological doses, on the order of milligrams per milliliter [39, 42]. This has led to several safety concerns as well as high costs of therapy [43].

## 1.4. Thesis goal: development of a clinically relevant bone engineering strategy

Bone engineering relies on, but is not limited to, the synergetic combination of scaffolds, cells, and bioactive factors as discussed thus far. For instance, it is important to develop a bone engineering strategy conducive to clinical translation. While there have been many successes in engineering bone (and other tissues) in vitro, in vitro cultivation protocols are not ideal for the clinic as (1) in vitro culture leads to safety concerns as it is unknown how culture conditions may affect the patient post-implantation or the biological and chromosomal properties of the cells being cultivated and (2) tissue engineering protocols often require a long culture period, contributing to high costs. It is estimated that a fully in vitro bioengineered bone construct utilizing bioreactor technology would cost more than $10000 per construct [44]. In addition, there is significantly less known about how tissue engineered constructs develop and integrate in vivo. This is important for clinical translation as the fate of implanted constructs must be well-understood. For example, the in vivo action of MSCs is a subject of some controversy. The classical thought, and the intended use of MSCs, is that they will differentiate into osteoblasts, thereby producing new bone to fill the defect. It has been proposed, however, that MSCs may have an indirect, paracrine signaling effect [45]. As such, another consideration for translation of bone engineering technologies is the development of an in vivo monitoring approach to ascertain the behavior of engineered constructs post-implantation.

With these considerations in mind, the goal of this dissertation is to develop a clinically relevant bone engineering approach in which autologous cells are implanted in a bioactive scaffold and the resulting construct is implanted immediately. The bioactive

scaffold will thus signal the cells to form bone post-implantation, bypassing the need for in vitro culture. To determine the validity of this hypothesis of the construct's mechanism, an in vivo imaging modality will also be explored.

In Chapter 2, the tools discussed here are combined to develop a bone engineering construct in an attempt to achieve this thesis goal. The results and potential improvements will be discussed. Chapters 3 and 4 will explore these improvements in further detail. Chapter 5 will address the in vivo imaging component. Finally, Chapter 6 will outline future directions after the completion of this thesis.

# Chapter 2: enhanced bone marrow and decellularized trabecular bone

This chapter draws from the following publication: Hung BP, Salter EK, Temple JP, Mundinger GS, Brown EN, Brazio P, Rodriguez ED, and Grayson WL. 2013. "Engineering bone grafts with enhanced bone marrow and native scaffolds." Cells Tissues Organs 198: 87-98.

## 2.1. Introduction

The current standard for treating long-bone non-unions involves intramedullary reaming and nailing [46]. Many years ago it was hypothesized that the debris from this reaming process could contain various osteoinductive factors, including cells and matrix components that could aid in bone healing [47]. This hypothesis was further supported when it was shown that debris is deposited into bone defects during surgery [48] and may aid in the healing of fractures; furthermore, a high density of cells resembling MSCs were found in reaming debris [46]. The development of a new system, the reamer-irrigator-aspirator (RIA; Synthes, West Chester, PA), allowed surgeons to avoid the elevated temperatures and pressures traditionally associated with intramedullary reaming, thereby decreasing necrosis in both the patient's bone and in the reaming debris [49].

Clinical case studies using RIA debris, also termed eBM due to its origin in the marrow cavity and the presence of minute bone chips, showed its high potential for bone repair even in cases where both intramedullary nailing and iliac crest bone autografting failed [50]. As such, eBM has attracted much interest in bone engineering as a potentially

abundant source of osteoprogenitor or stem cells. Recent research into the cells present in eBM has shown that there are indeed MSC or MSC-like cells within eBM [51]. Additionally, many more stem cells can be isolated from eBM compared to similar volumes of iliac crest bone marrow aspirate [51].

We hypothesized that DCB scaffolds, discussed in section 1.3.1, could provide osteoinductive factors and mechanical support for seeded eBM, further enhancing the potential of eBM to regenerate bone de novo in non-healing defects. In this chapter, we characterized the eBM tissue extracted from the femurs of Yorkshire pigs and investigated its potential for engineering bone grafts by combining the eBM with DCB scaffolds. We focused on developing techniques for effectively seeding eBM into channels drilled into the scaffolds and utilized collagen gel coatings to direct cell migration into the trabecular pore spaces. Following cultivation in osteogenic conditions, we evaluated cell viability and proliferation, as well as the ability to induce uniform tissue development.

## 2.2. Materials and methods

### *2.2.1. Experimental design (Figure 2.1)*

The eBM was harvested via intramedullary reaming of porcine femurs as described below. Collected eBM was assessed to determine its tissue and stem cell composition, as well as its potential for use in conjunction with scaffolds to engineer bone grafts. Tissue composition was determined using micro-computed-tomography (micro-CT) imaging of the whole tissue followed by paraffin embedding and sectioning for histological analysis. In a second experiment, cells present in the eBM were released

by collagenase digestion and assessed for colony-forming unit potential as well as multilineage differentiation capabilities. Finally, in the third experiment, eBM was seeded into DCB scaffolds and cultured under osteogenic conditions in vitro to create bone grafts. Bone scaffolds were 9 mm in diameter and 4 mm in height, with central channels 3 mm in diameter within which the eBM was initially seeded (**Figure 2.1**, **B**). Two groups were evaluated: scaffolds were either untreated or, in the second group, scaffold pores were coated with a thin film of collagen to promote cell migration. After 4 weeks, both groups were evaluated for cell distribution, viability, proliferation, and new bone formation.

*2.2.2. Surgery and harvesting of eBM*

An RIA device was used to extract eBM from the medullary canals of porcine femurs of 3 pigs immediately post-euthanasia (**Figure 2.2**). Pigs were euthanized with intravenous injection of potassium chloride at a minimum concentration of 1 mmol/kg. After sterile preparation of the surgical site, the distal femur was exposed via an incision lateral to the patella. A burr was used to access the femoral medullary canal through the articular surface of the distal femur, and the RIA device was inserted into the femoral canal under fluoroscopic guidance following assembly of the device and selection of an appropriately sized drill head according to the manufacturer's instructions. The medullary contents were then aspirated from the femoral canal while continuously irrigating the canal with sterile normal saline. The aspirated bone and bone marrow were collected and isolated from the irrigation solution using a 500 μm mesh filter under sterile conditions.

*2.2.3. Micro-CT scanning of eBM*

Fresh whole eBM was scanned using micro-CT to determine the presence of bone within the tissue. Each sample was placed in a polystyrene foam tube and mounted vertically in the Skyscan 1172 (Skyscan, Kontich, Belgium) scanner sample chamber. Micro-CT imaging was done at 50 kV and 200 µA at medium camera resolution (2000-1000 pixel field width). The scanner was set to distinguish spatial resolution at 10 µm. Data was analyzed using Skyscan CTAn software with the bone window set to a fixed threshold.

*2.2.4. Histological assessment of eBM*

After micro-CT scanning, eBM was fixed with 3.7% formalin, embedded in paraffin, and sliced into 5 µm sections for histology. Sections were stained with haematoxylin & eosin and Masson's Trichrome stain (all reagents from Sigma Aldrich, St. Louis, MO). Safranin O (ScholAR Chemistry, West Henrietta, NY) was used to confirm the presence of cartilage.

*2.2.5. eBM digestion and cell isolation*

After harvesting, 1 g of eBM was digested in a 0.2% w/v collagenase (Worthington Biochemicals, Lakewood, NJ) solution prepared in high-glucose Dulbecco's Modified Eagle's Medium (DMEM; Invitrogen, Carlsbad, CA) supplemented with 100 U/mL penicillin and 100 µg/mL streptomycin (Cellgro, Manassas, VA) and 10% v/v fetal bovine serum (FBS; Atlanta Biologicals, Flowery Branch, GA). The tissue was digested for 1 h at 37 °C while being continuously agitated. The medium was then

collected and cells were isolated by first passing supernatant through a 100 μm cell strainer and then centrifuging the filtered isolate at 300 RCF for 5 min. The cells were resuspended in growth medium (DMEM with high glucose, 100 U/mL penicillin and 100 μg/mL streptomycin, 10% v/v FBS, and 1 ng/mL basic fibroblast growth factor; PeproTech, Rocky Hill, NJ) and expanded for 1 passage before using for the colony-forming unit fibroblast assay and multilineage differentiation.

*2.2.6. Colony-forming unit fibroblast assay*

Previously expanded cells were plated in 100 mm Petri dishes at 15/cm$^2$ as previously described [52]. By 9 days, large colonies were evident throughout the dish and the culture was fixed with 3.7% formalin. 0.05% v/v crystal violet solution (Sigma Aldrich) was applied to the fixed culture for 30 min to visualize colonies. The crystal violet was washed off with tap water and colonies were manually quantified.

*2.2.7. Multilineage differentiation*

Differentiation of extracted cells along osteogenic, chondrogenic, adipogenic, and vasculogenic lineages were performed using passage 2 cells following published protocols. Osteogenic differentiation was achieved by seeding cells at an initial density of 5000 /cm$^2$ and culturing for 4 weeks in osteogenic medium, which was comprised of low-glucose DMEM supplemented with 10% v/v FBS, 100 U/mL penicillin and 100 μg/mL streptomycin, 10 mM β-glycerophosphate (Sigma Aldrich), 100 nM dexamethasone (Sigma Aldrich) and 50 μM ascorbic acid (Sigma Aldrich) [30]. Cultures were assayed

for osteogenic differentiation by staining protein-associated calcification with Alizarin Red S (Sigma Aldrich).

Chondrogenic differentiation was achieved by growing cells in pellet culture (500000 cells per pellet) in high-glucose DMEM supplemented with 100 U/mL penicillin and 100 µg/mL streptomycin, 1 µM dexamethasone, 10 ng/mL transforming growth factor β3 (PeproTech), 50 µM ascorbic acid, 110 µg/mL sodium pyruvate (Sigma Aldrich), 40 µg/mL L-proline (Sigma Aldrich), and ITS (10 µg/mL bovine insulin, 5.5 µg/mL human transferrin, 6.7 ng/mL selenium; Sigma Aldrich) [29]. At the end of 4 weeks, pellets were embedded in paraffin, sectioned with a microtome, and assayed for chondrogenic differentiation by staining glycosaminoglycans with Safranin O.

Adipogenic differentiation was performed by seeding the cells at 10000 /cm$^2$ in tissue culture flasks and culturing for 4 weeks in high-glucose DMEM supplemented with 10% v/v FBS, 100 U/mL penicillin and 100 µg/mL streptomycin, 5 µg/mL recombinant human insulin (Invitrogen), 1 µM dexamethasone (Sigma Aldrich), 200 µM indomethacin (Sigma Aldrich), and 500 µM 3-isobutyl-1-methylxanthine (Sigma Aldrich) [31]. Cultured were assayed for adipogenic differentiation by staining lipid droplets with Oil Red O (Sigma Aldrich).

Endothelial growth was induced by seeding cells at an initial density of 20000 /cm$^2$ and culturing for 4 weeks in EGM-2 (Lonza, Walkersville, MD) [53]. Cultures were assayed for the presence of endothelial markers by RT-PCR on CD31, von Willebrand factor (vWF), and vascular endothelial growth factor receptor 2 (VEGFR). Primer sequences are shown in **Table 2.1**.

*2.2.8. Decellularization of bovine trabecular bone*

DCB scaffolds were prepared as described previously [53]. Trabecular bone cores 9 mm in diameter and 4 mm in height were taken from the subchondral region in the ling bones of 0.5- to 4-month-old calves. Cellular material was first removed by washing with a high velocity jet of water. The remaining cellular material was removed through sequential detergent washes. Briefly, the scaffolds were washed for 1 h in phosphate-buffered saline (PBS; Cellgro) containing 0.1% w/v ethylenediaminetetraacetic acid (EDTA; Sigma Aldrich) at room temperature. Following that, they were washed overnight at 4 °C in PBS containing 0.1% w/v EDTA and 10 mM Tris (Sigma Aldrich). Scaffolds were washed in PBS forma another hour before being washed with PBS containing 10 mM Tris and 0.5 w/v sodium dodecyl sulfate (Sigma Aldrich) for 24 h at room temperature. After removing the sodium dodecyl sulfate with PBS washes, the scaffolds were washed with PBS containing 10 mM Tris, 50 U/mL DNAse (Roche Applied Science, Indianapolis, IN), and 1 I/mL RNAse (Roche Applied Science) for 5 h. Enzyme solutions were removed by extensive washes with water. Scaffolds were the sterilized with an overnight wash in 70% ethanol and rinsed with PBS before use.

*2.2.9. Implantation of eBM into DCB scaffolds*

Channels with a diameter of 3 mm were drilled axially through the scaffolds and eBM was packed into these channels. In half of the scaffolds, the trabecular pore spaces were coated with collagen to enhance cell migration and distribution throughout the scaffold. Rat-tail collagen (Sigma Aldrich) was mixed with sodium hydroxide and PBS to dilute the mixture to 2.5 mg/mL and raise the pH such that the collage would form a gel.

Before gelation, 20 μL of collagen solution was pipetted into and out of the trabecular pores several times to ensure the scaffold walls were completely coated with collagen. Excess gel was lightly aspirated so that the pore spaces were not clogged. The collagen coating was allowed to solidify for 10 min at room temperature before seeding with eBM.

### *2.2.10. Evaluation of bone constructs*

Constructs were cultured in osteogenic medium for 28 days. At this time point, three constructs from each group (control vs. collagen coated) were stained with a live-dead kit (Invitrogen) to assess cell viability and distribution. Live/dead imaging was done using confocal microscopy. After imaging, constructs were fixed in a 3.7% formalin solution overnight. Fixed constructs were scanned using micro-CT as described above to assess new mineralization. After micro-CT scanning, constructs were demineralized in 10% EDTA in Tris buffer for 1 week before dehydration and embedding for haematoxylin/eosin staining. Three scaffolds from each group were also assayed for DNA content using the Quant-iT PicoGreen dsDNA Assay Kit (Invitrogen) to determine the extent of cell proliferation over the culture time.

### *2.2.11. Statistics*

Unless otherwise noted, statistical analyses consisted of Student's t-tests with post-hoc Bonferroni correction. Statistical significance was determined at $p<0.05$.

## 2.3. Results

### *2.3.1. Cell and tissue characterization*

The reaming procedure produced up to 25 mL of eBM per pig. Whole tissue analysis revealed evidence of fat, cartilage, bone, and vascular tissues in various regions of the eBM (**Figure 2.3**). Digestion of 1 g of eBM in collagenase yielded approximately 62 million cells, most of which morphologically resembled non-adherent erythrocytes. After plating in monolayer for expansion, the adherent cells were grossly examined and showed heterogeneity throughout the population, with at least four distinct apparent morphologies (**Figure 2.4**, **A-D**). The population became morphologically homogenous after two additional passages (**Figure 2.4**, **E-F**). The colony-forming unit fibroblast assay revealed large colonies throughout the dish, which were readily apparent through crystal violet staining after 9 days of culture. There was an average of 95 colonies per dish. Passage 2 cells could be readily differentiated along osteogenic, chondrogenic, and adipogenic lineages as determined by Alizarin Red S, Safranin O, and Oil Red O staining, respectively. In response to treatment with angiogenic factors, cells showed upregulation in expression of endothelial genes CD31, vWF, and VEGFR (**Figure 2.5**).

### *2.3.2. Cell distribution and osteogenesis in DCB scaffolds*

Scaffolds seeded with eBM were cultured under osteogenic conditions for 4 weeks and the harvested. To investigate whether the collagen coating had an effect on cell proliferation and distribution throughout the bone scaffolds, DNA content was quantified, cell distribution was asses using histologic sectioning, and live/dead imaging was performed. Cell numbers in collagen-coated scaffolds were statistically higher than

they were in control scaffolds. In control scaffolds, the cell numbers increased 1.28 ± 0.06 fold relative to day 0 values, while cells in collagen-coated scaffolds increased 1.66 ± 0.1 fold. Live/dead imaging (**Figure 2.6**) and histological analysis (**Figure 2.7**) indicated that besides having more cells, the number of cells that migrated out of the central channels and into the pore spaces was also higher in response to collagen coating.

Finally, we assayed the mineral content within the seeded scaffolds via micro-CT analysis (**Figure 2.8**). Qualitative and quantitative assessments indicated that collagen-coated scaffolds had increased mineral content in the scaffold periphery as compared to both day 0 and to non-coated scaffolds, though differences between coated and non-coated scaffolds were not statistically significant. For quantitative analysis, percent bone volume, trabecular number, and trabecular spacing were calculated in both the scaffold periphery and in the central channel. In the periphery, collagen-coated scaffolds showed statistically higher percent bone volume and trabecular number and statistically lower trabecular spacing relative to day 0 scaffolds after 4 weeks of osteogenic culture. Control scaffolds did not have significantly more bone content than did scaffolds at day 0. No statistically significant differences were found in the above three parameters within the central channel between groups.

## 2.4. Discussion: investigation of eBM and DCB scaffolds

One of the major obstacles limiting the translation of tissue engineering approaches to the clinic is the availability of a suitable source of multipotent cells, and the low incidence of MSCs in bone marrow aspirates has inspired searches for alternative cell sources. eBM tissue has significant potential to address this challenge by providing a

large quantity of tissue to fill the defect site. Additionally, eBM contains high concentrations of osteoprogenitor cells. In this study, we analyzed both the cellular and whole tissue characteristics of eBM in vitro to provide further insight into the clinical potential of this tissue for regenerating bone without the complicating factors of an in vivo study.

Whole-tissue analysis of eBM revealed the presence of various tissue types, including fragments of fat, cartilage, bone, and intact pieces of vasculature. During the reaming process, the reamer head passes through the articular surface of the distal femur, through subchondral bone, and then into the marrow cavity. Consequently, it is not surprising that these four tissue types would be aggregated within the debris. While it is unclear how the presence of these various tissues influences the stem cell populations, eBM has been successfully used for bone regeneration [50] and so we speculate that the environment is at least conducive to osteogenic differentiation of the stem cells.

We investigated the use of eBM in DCB scaffolds in an in vitro model of bone engineering, which to our knowledge has not been previously investigated. In contrast to the single-cell suspensions studied previously, in order to implant the solid eBM putty into the bone scaffolds, it was necessary to drill channels into the scaffolds. This seeding method intrinsically resulted in tissue inhomogeneities since the peripheral trabecular regions are initially acellular. Hence, it was essential to stimulate cell outgrowth into the scaffold pore spaces to enable the development of uniform bone tissues. We investigated methods to enhance cell migration throughout the scaffold, hypothesizing that collagen coating would provide cells with more attachment sites for migration throughout the scaffold. Type I collagen is a predominant constituent of bone [54] as well as the most

abundant extracellular matrix protein in the body. Due to its ability to enhance cell attachment and influence differentiation, collagen gels have been widely used for enhancing bone engineering, though their low mechanical strength requires them to be combined with other materials, such as calcium phosphate [55] or hydroxyapatite [56] scaffolds. We found that coating the scaffold pores with collagen did indeed enhance cell migration and proliferation in the scaffolds, resulting in more uniform tissue distribution in the grafts after 4 weeks of culture. This correlated with quantitatively higher mineral deposition in the trabecular regions of the collagen-coated scaffolds compared to control scaffolds after 4 weeks of osteogenic culture. It is unlikely that the collagen coating itself promoted osteogenesis, as previous work into MSC differentiation in collagen gels suggests the collagen itself cannot induce osteogenesis without other osteogenic cues [57]. A more reasonable explanation is that the increased osteogenic outcome may simple be the result of having a greater number of cells.

Interestingly, no differences were observed between initial and final timepoints or different experimental groups in levels of mineral deposition in the central channels where the eBM was originally seeded. There is a high mineral content in this original tissue due to the bone chips reamed from the endosteal surface of the long bone. The apparent inability of stem cells or osteoprogenitors to deposit more mineral throughout the culture period may be due to the limitations in mass transport through the densely packed eBM within the scaffold center. Such limitations would restrict the exposure of cells to both nutrients as well as to osteoinductive supplements in the medium. This limitation does not initially exist in the scaffold periphery where the open pore spaces facilitate infusion of culture medium. Improving cell outgrowth into the surrounding

scaffold by encapsulation of pro-migratory cytokines into the hydrogel may alleviate this inhibitory effect in the construct center.

Our study also investigated the characteristics and capabilities of cells present within the eBM in order to gain some mechanistic insight into the regenerative potential of the tissues. We extracted cells from eBM to compare their multilineage capabilities with findings presented in the literature, which have mostly focused on characterizing MSC or MSC-like cells within eBM [46, 51, 58]. The distinct morphologies of extracted cells suggested significant phenotypic heterogeneity. This correlated with the observation of a variety of tissue types present within eBM. A portion of extracted cells exhibited the potential to form colonies, suggesting that naïve populations are present. We found large colonies present by 9 days post-seeding, which is considerably earlier than the traditional assessment timepoint of 14 days post-seeding [59, 60]. Previous work has shown that eBM contains a higher density of stem cells than traditional bone marrow aspirate does [51], so some colonies may have merged in our assay making them visible earlier.

We speculate that these colony-forming cells were the subpopulations that maintained the potential to differentiate down the three classic mesenchymal lineages. Our cells showed robust differentiation along the osteogenic and chondrogenic lineages, but very weak adipogenic potential. A key observation was the upregulation of three different endothelial markers in response to angiogenic factors compared to cells grown under expansion conditions. It is not clear if this indicated “differentiation” of a stem cell population or “selective expansion” of a pre-existing endothelial progenitor subpopulation in response to VEGF and basic fibroblast growth factor. To our knowledge, this potential for endothelial capacity has not been previously demonstrated,

but raises exciting possibilities about the potential of engineering pre-vascularized bone grafts using eBM.

The eBM can be harvested in large amounts and used intraoperatively. It has significant clinical utility, which can be further enhanced by combining it with osteoinductive scaffolds capable of immediately providing mechanical integrity to the defect site. As we have demonstrated, eBM contains relatively high concentrations of stem cells, which can be guided to work in tandem with existing cell populations to develop complex tissue grafts. While we focused on in vitro cultivation of eBM for our study, eBM can in fact be implanted in situ during surgery, as its high concentration of stem cells allows it to be used without in vitro expansion. Scaffolds can also be prepared beforehand, making this system very relevant clinically. Compared to current approaches involving autologous bone grafts, this approach results in lower donor-site morbidity.

## 2.5. Discussion: limitations and potential improvements

With the method developed in the current study using components more widely studied, DCB scaffolds would be prepared and milled into patient-specific geometries. eBM would then be packed into the scaffolds, creating a bone graft that can be implanted. While this system has its strengths as discussed, it suffers from key limitations that will be addressed in upcoming chapters.

First, the preparation of DCB scaffolds, as outlined in section 2.2.8, is difficult and labor-intensive. A continuous block of trabecular bone larger than the defect must be obtained for scaffold preparation, and for the critically sized defects discussed in Chapter 1, section 1.1, this may not always be possible. Even if it were, this block of bone must

be subject to the decellularization protocol, which requires transport of water and detergents into the tissue center as well as transport of cellular material out. For large blocks of bone, this becomes difficult without specialized equipment. Finally, assuming decellularization is successful, CNC milling of the bone must be used to produce anatomical geometries, which is a challenging step, especially if the shape has overhangs that cannot be easily reached with the machine's cutting tool.

Second, eBM harvesting, as outlined in section 2.2.2 and depicted in **Figure 2.2**, is an extremely invasive procedure despite invoking less donor-site morbidity compared to autologous bone grafting. The patient runs the risk of fracture during reaming and, in particular, the articular cartilage is severely damaged. The inability of cartilage to heal is well-documented in the literature; as such, a procedure to repair bone that results in cartilaginous damage is not ideal.

Potential improvements to scaffold fabrication involve the use of 3D printing technologies, while adipose-derived stem cells (ASCs) may provide an alternative cell source that is less invasively harvested than is bone marrow. The advantages of these methods are discussed here before they are implemented to overcome the limitations with the current approach outlined above.

### *2.5.1. 3D printing of synthetic scaffolds*

3D printing, though a term encompassing a wide variety of methods, generally consists of building up a structure layer-by-layer. 3D printing technology has evolved to where just about any 3D geometry can be fabricated, including craniofacial scaffolds. 3D printing is thus a method which can build shapes that would be very challenging to

produce using a CNC mill; furthermore, high-resolution printers can achieve finely controlled pore architecture and porosity, factors known to affect resident cells and which cannot be controlled using naturally derived scaffolds.

One early method of 3D printing was the inkjet/binder system, in which a nozzle dispenses a binder solution onto a powder bed. Powder that contacts the binding solution is bound together, while the remaining powder remains free and serves as support. For bone, the powder is generally the mineral β-tricalcium phosphate to mimic the mineral phase of bone. The binder is generally some type of acid, such as citric acid [61] or phosphoric acid [62]. While this method does not require support structures, allowing easy printing of overhangs, the low viscosity of the acid binder solutions results in low resolution and residual acid trapped within large scaffolds can compromise cell viability. The mechanical integrity of scaffolds printed by this method also depends highly on the interaction between the binder and the powder; in general, the resulting properties fall on the brittle side. One key advantage of the inkjet/binder method, however, is the ability to print structures at room temperature, allowing for the direct incorporation of cells or growth factors.

A somewhat similar technique is selective laser sintering (SLS), which retains the powder bed but uses a laser to sinter the particles together. The resolution is much better than with the binder solution, as there are no problems associated with viscosity and flow. In SLS, the resolution depends on the diameter of the laser, which is usually on the order of hundreds of micrometers [63, 64], enough to produce struts and pores of comparable sizes to that found in native trabecular bone. SLS, like its inkjet/binder counterpart, does not require support structures as the un-sintered powder acts as support; however, the

high temperatures required to sinter particles preclude the addition of bioactive molecules or living cells.

3D printing has also been performed using extrusion of a viscous liquid from a nozzle and allowing that liquid to solidify, thereby building a structure up layer-by-layer. Extrusion-based methods require support structures, unlike with powder-based methods. One such method uses a special class of materials with the thixotropy property, in which the material has low viscosity when under shear (i.e. while being pressure-extruded out the nozzle) but becomes much more resistant to flow under static conditions. 3D printing of thixotropic materials has the benefit of not requiring high temperatures, as the flow properties of the materials are only shear-dependent; however, materials with this property are uncommon and are restricted to certain types of porous glass [16, 65] or mixtures of polymers with organic solvents [66]. Also, the compressive stress the scaffold may experience while in the body may be problematic if the scaffold begins to deform due to the thixotropy property.

Another extrusion method uses a molten thermoplastic. Once extruded, the thermoplastic cools and solidifies. This technique is known as melt extrusion and is commonly used for poly[ε-caprolactone] (PCL) [67], which has a low melting point of 60 °C [68]. This property is important because the polymer must cool and solidify quickly once it has been extruded; otherwise, it will be impossible to stack the printed layers on top of each other. Consequently, polymers with melting points closer to room temperature work best for melt extrusion. The resolution of this method depends on both the thermoplastic's thermal properties (e.g. viscosity at print temperature) and the diameter of the nozzle. Generally, the resolution of melt extrusion allows the production

of pores and struts on the order of 0.5 – 1 mm, comparable to that of native trabecular bone. Melt extrusion is very versatile, as any material that can be melted and extruded is suitable to this method. As such, melt extrusion 3D printing was selected to produce scaffolds to overcome the limitations of DCB scaffolds; this is outlined in Chapter 3.

### *2.5.2. Adipose-derived stem cells*

ASCs are harvested from lipoaspirate and represent a larger population than do the MSCs within bone marrow; ASCs make up approximately 5% of nucleated cells in the stromal vascular fraction obtained from lipoaspirate [69, 70]. As such, ASCs alleviate the problem of MSC rarity, similar to eBM. Additionally, it has been shown that ASCs can undergo differentiation to the three classical mesenchymal lineages [71], similar to MSCs. Finally, more recent studies have indicated that the ASC population contains a mature endothelial population, allowing for heterotypic interactions that can lead to vascularized tissue formation [72]. Given that liposuction is a less invasive procedure than is intramedullary reaming, combined with these considerations, ASCs were investigated further in subsequent studies in this thesis.

In utilizing ASCs as the stem cell population of interest, a recent study asked the question of what biomolecule could promote both the bone-differentiating ability of ASCs as well as the innate vascular-forming population within ASCs [73]. This study focused on platelet-derived growth factor BB (PDGF-BB), a biomolecule known to enhance bone regeneration when injected in a bone defect [74] and to promote the stability of nascent vasculature via attraction of pericytes [75, 76]. It was shown that, interestingly, PDGF-BB did enhance both bone-forming and vascular-forming

capabilities of ASCs. In particular, it was able to do so at 20 ng/mL, a physiologically relevant concentration. In contrast, BMP2 was unable to elicit a vascular-stabilizing effect, nor was it able to elicit more bone formation, at this concentration. With this observation and the potential for a biomolecule that can elicit bioactive effects at low concentrations, PDGF-BB was investigated further in terms of its osteoinductive effects on ASCs in Chapter 4.

## 2.6. Overview of new approach

The first attempt at developing a clinically relevant bone engineering method, as outlined at the beginning of this chapter, utilized eBM and DCB scaffolds. With the considerations outlined subsequently, the new approach will utilize ASCs and 3D printed scaffolds with incorporation of PDGF-BB. The investigation of these components will be the topic of the following two chapters.

# Tables: Chapter 2

| Gene | Forward primer sequence | Reverse primer sequence |
|---|---|---|
| GAPDH | 5′ ATG GTG AAG GTC GGA GTG AAC 3′ | 5′ CGT GGG TGG AAT CAT ACT GGA A 3′ |
| CD31 | 5′ CGG CAA GGT GGT CAA GAG AAG 3′ | 5′ TGG TAG GAA ATG GGC GAG GTT 3′ |
| VEGFR | 5′ CAG ATG ACA GCC AGA CAG ACA 3′ | 5′ AGA TGC CAC AGA CTC CTT GC 3′ |
| vWF | 5′ TGT GGA GAA GAG ACG CTT GG 3′ | 5′ CCG ATG ATG GAG AAG GAG TGT 3′ |

**Table 2.1**: Primer sequences for endothelial real-time polymerase chain reaction on isolated enhanced bone marrow.

# Figures: Chapter 2

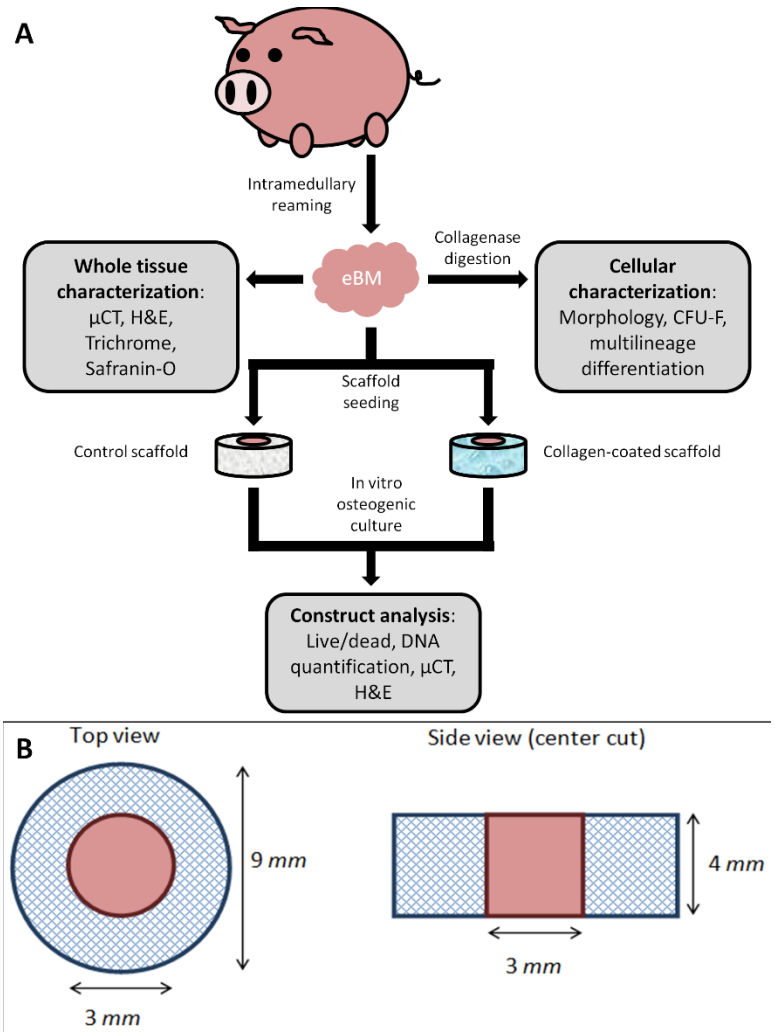


**Figure 2.1**: Experimental design for characterization of enhanced bone marrow and decellularized trabecular bone scaffolds (**A**). eBM was studied as a whole tissue and cells were extracted from eBM for characterization. eBM was also seeded into decellularized trabecular bone scaffolds with the dimensions depicted in (**B**).

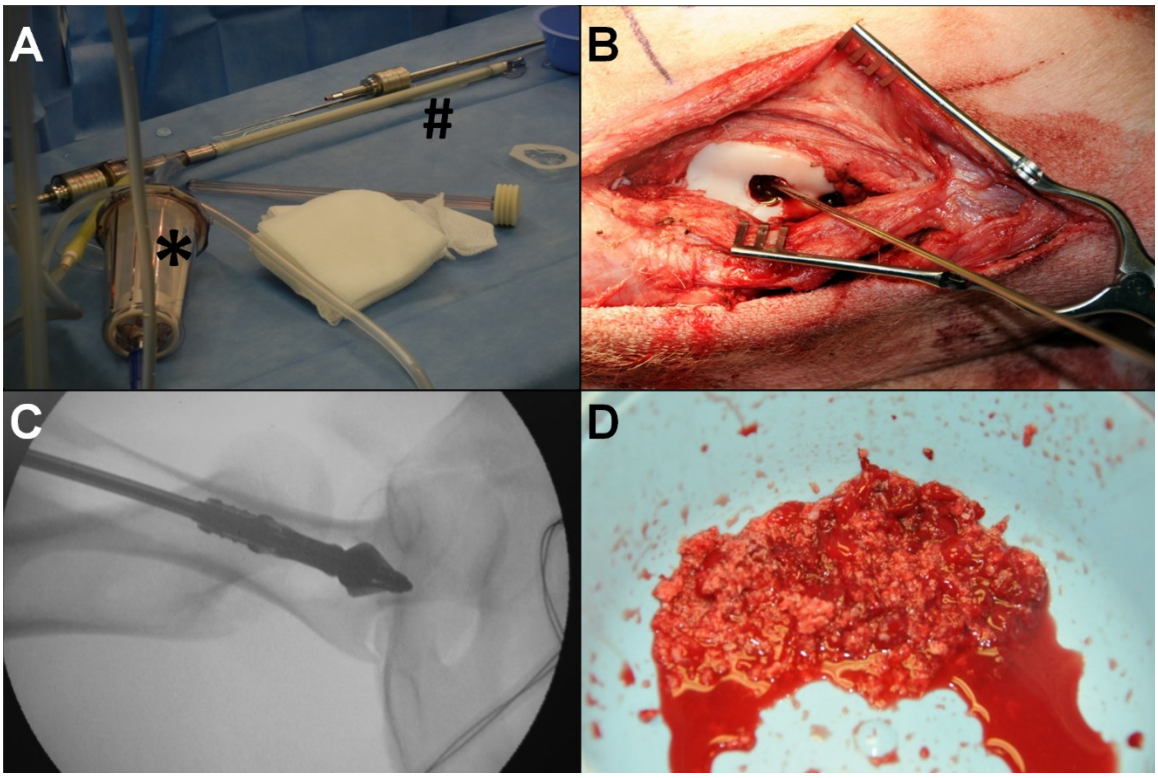


**Figure 2.2**: eBM harvest. (**A**) The RIA system, including the reamer head (#) and collecting filter (*). (**B**) Insertion of the reaming guide through the exposed femoral condyle. (**C**) Representative fluoroscopic image illustrating the drill head in the femoral canal and associated radiolucent areas of extracted canal marrow. (**D**) Harvested porcine eBM putty.

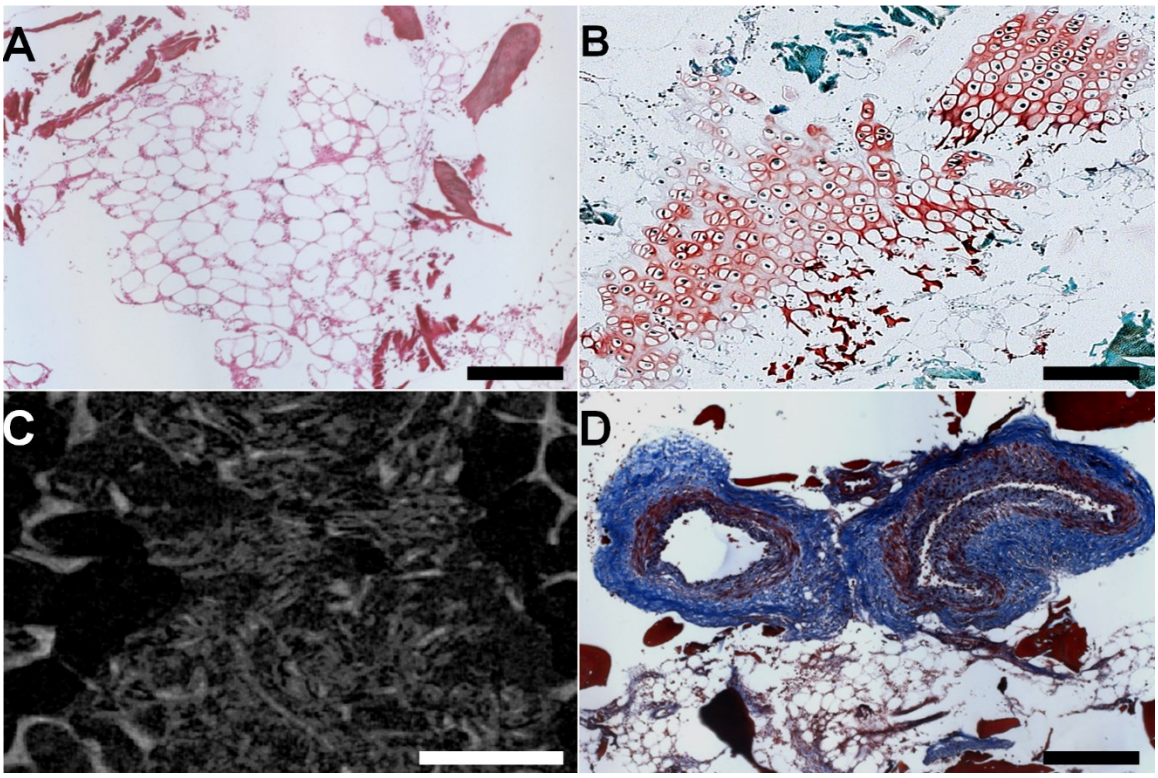


**Figure 2.3**: Histological tissue characterization. (**A**) Fat "ghosts" are evident via haematoxylin/eosin staining. (**B**) Safranin O (red) staining showed presence of glycosaminoglycan around chondrocyte lacunae indicating the presence of cartilage tissue. (**C**) Micro-CT image of the eBM immediately after implantation into the central channel of the DCB scaffold. The numerous bone particulates (grey) in the eBM are evident. (**D**) Masson's Trichrome staining of a section through the eBM shows the presence of vascular structures. Scale bars: 100 µm (**A**, **B**, **D**) and 1 mm (**C**).

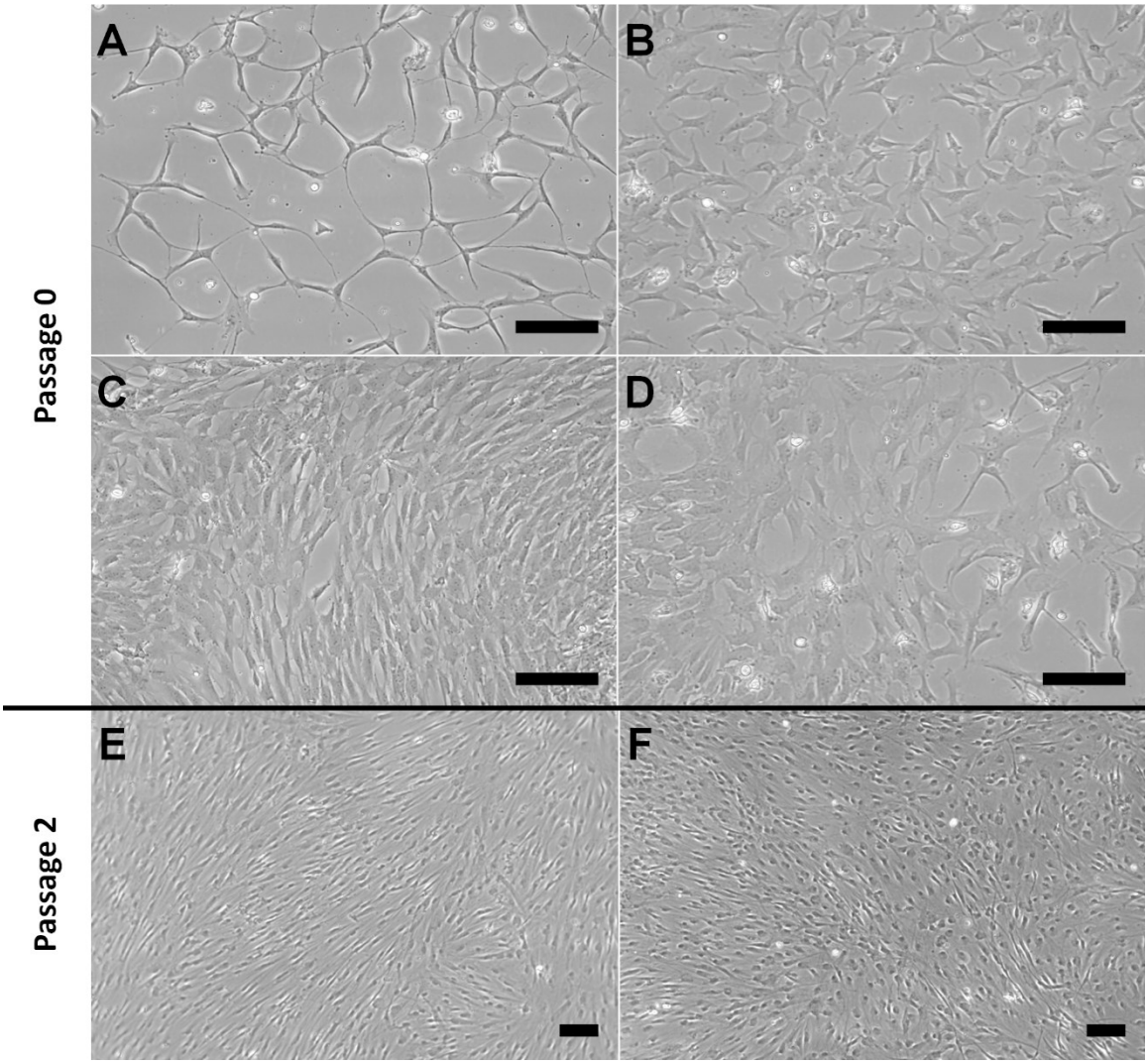


**Figure 2.4**: Phase contrast images of extracted cells. (**A**-**D**) Monolayer culture of passage 0 cells extracted from collagenase-digested eBM appeared morphologically heterogeneous. (**E**, **F**) After two passages, cell morphology became more homogeneous and spindle shaped. Scale bars: 100 µm.

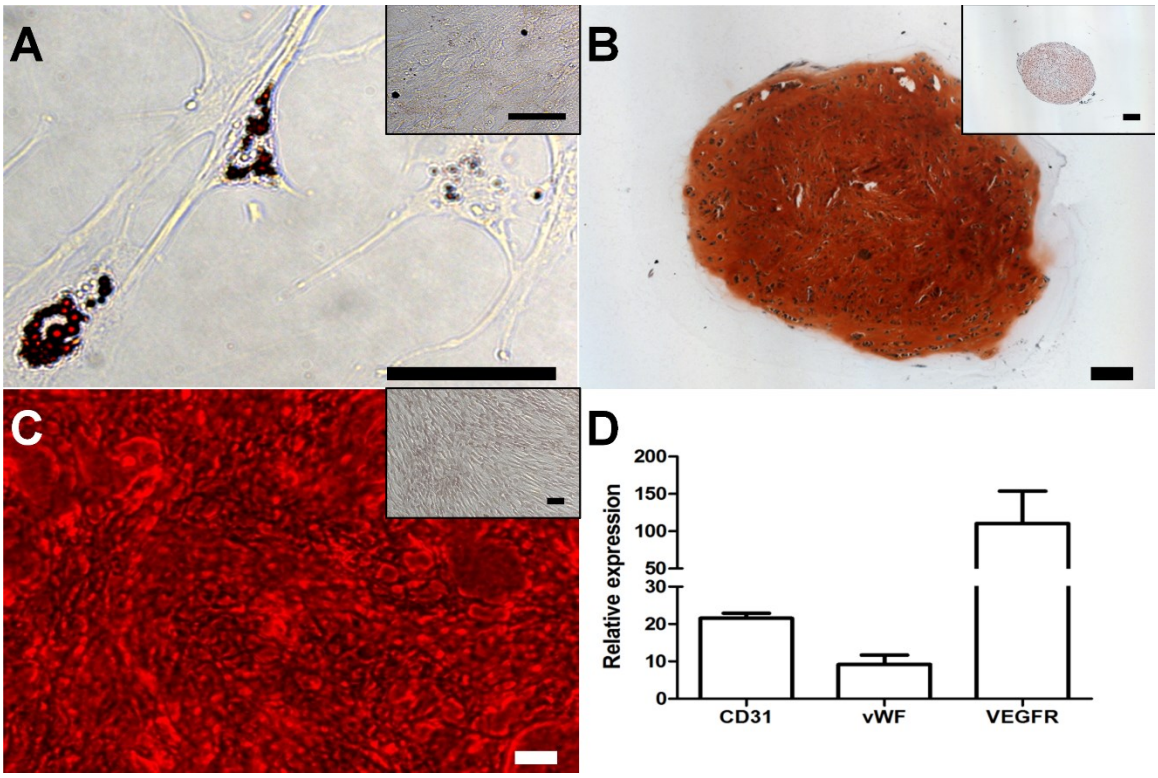


**Figure 2.5**: Multilineage differentiation potential of passage 2 cells. (**A**) Oil Red O staining showing the presence of adipocytes. (**B**) Safranin O staining of cell pellets indicates robust chondrogenesis. (**C**) Alizarin Red S stains indicate osteogenesis. (Insets) Negative (undifferentiated) controls. Scale bars: 100 µm. (**D**) Endothelial gene expression levels of cells cultured with angiogenic supplements. Expression was normalized to control cultures.

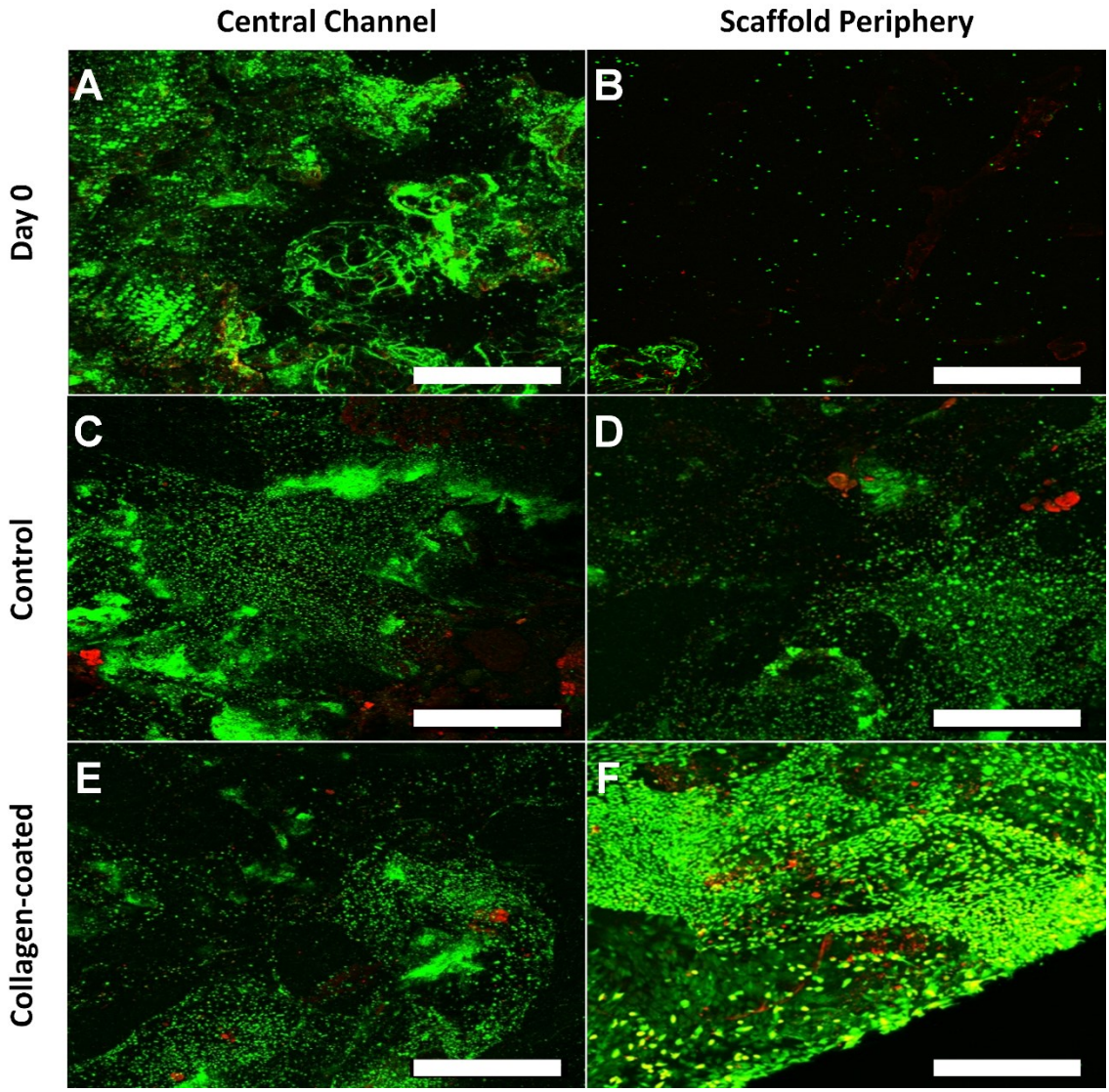


**Figure 2.6**: Live/dead maximum intensity projections. These were used to assess the presence of viable cells in the construct. On day 0 there were cells in the central channel (**A**) but negligible quantities of cells in the construct periphery (**B**). At 4 weeks, there were considerably fewer cells in the periphery of control scaffolds (**D**) relative to the collagen-coated scaffolds (**F**). Scale bar: 500 μm.

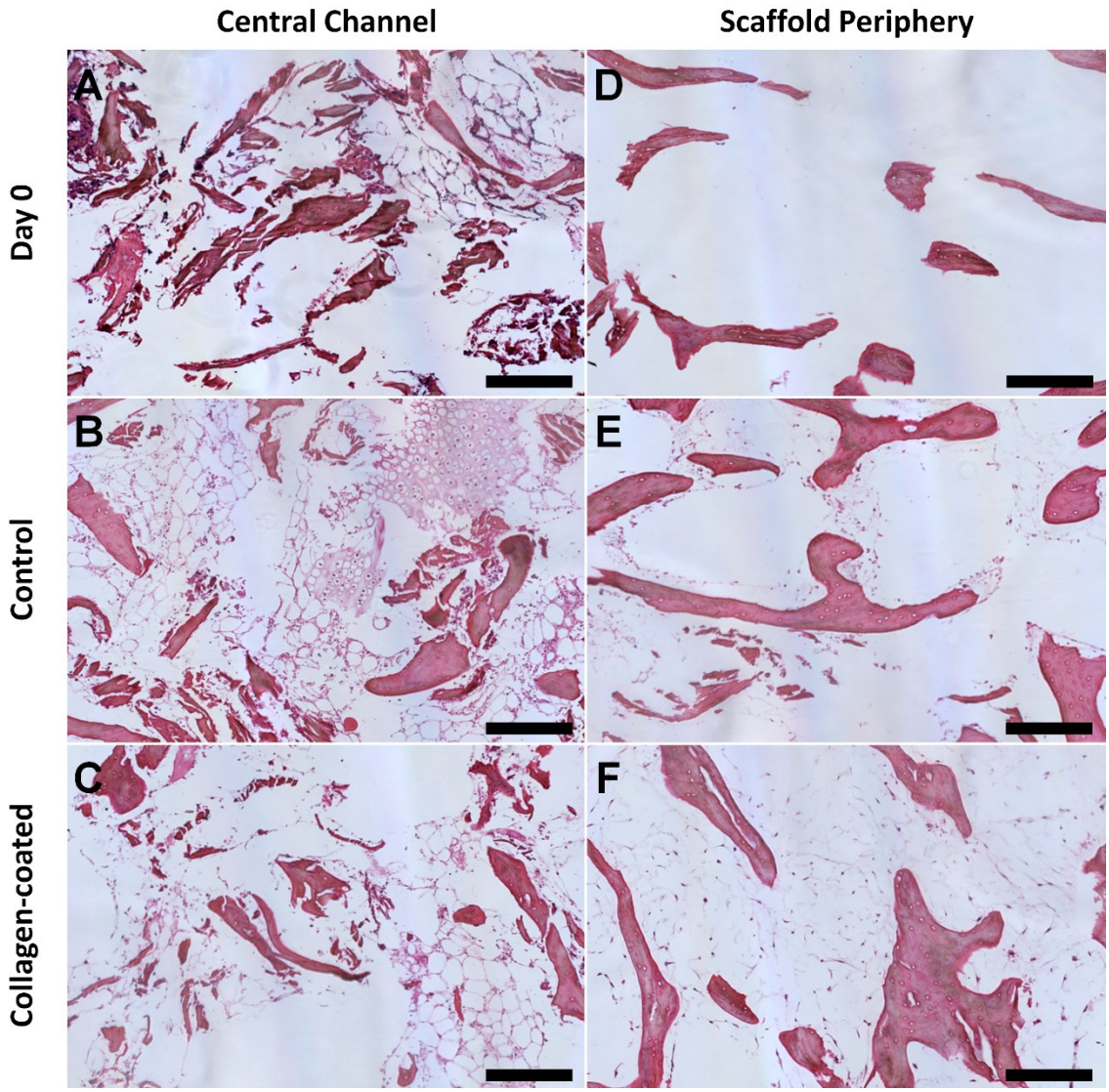


**Figure 2.7**: Cell migration into trabecular construct periphery. Haematoxylin/eosin staining indicated that cells were present in dense tissues in the central channel at day 0 (**A**) and at week 4 in both groups (**B**, **C**). There are almost no cells in the periphery at day 0 (**D**). There were significantly fewer cells in the periphery of control scaffolds (**E**) relative to collagen-coated scaffolds (**F**) after 4 weeks. Scale bar: 100 µm.

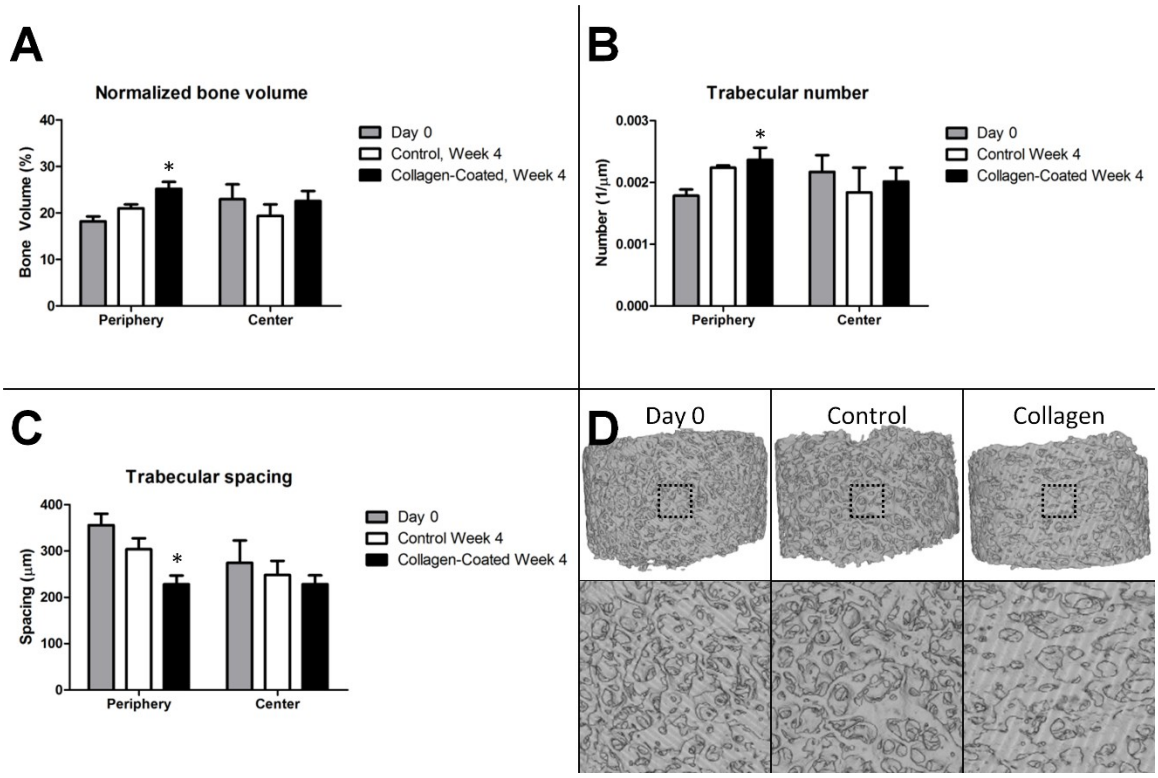


**Figure 2.8**: Micro-CT of bone constructs. Micro-CT analysis of constructs after 4 weeks of osteogenic culture demonstrate that in the scaffold periphery collagen-coated scaffolds showed higher normalized bone volume (i.e. bone volume/tissue volume; (**A**)) and trabecular number (**B**), and lower trabecular spacing (**C**). (**D**) Qualitative 3D reconstructions corroborate these findings ($n$ = 3; *$p<0.05$ from day 0). No statistical differences were found for mineral content or structural parameters in the central channels.

# Chapter 3: 3D printing of scaffolds for bone engineering

This chapter draws from the following publications: (1) Temple JP*, Hutton DL*, Hung BP, Yilgor PY, Cook CA, Kondragunta R, Jia X, and Grayson WL. 2014. "Engineering anatomically shaped vascularized bone grafts with hASCs and 3D-printed scaffolds." J Biomed Mater Res A 102: 4317-4325; (2) Hung BP, Naved BA, Nyberg EL, Dias M, Holmes CA, Elisseeff JH, Dorafshar AH, and Grayson WL. 2016. "Three-dimensional printing of bone extracellular matrix for craniofacial regeneration." (under review).

## 3.1. Development of a 3D printer

In the first part of this chapter, we present a method for 3D printing anatomically shaped PCL scaffolds with varying internal pore structures using a custom-designed 3D printer. PCL has emerged as a favorable polymer for scaffold fabrication; besides the advantage of low melting point as discussed in Chapter 2, section 2.5.1., it is biocompatible and safely breaks down in the body [77]. As such, PCL was chosen as the biomaterial to engineer porous, 3D printed scaffolds.

### *3.1.1. Construction of the custom 3D printer*

To construct the 3D printer, we converted a Syil X4 CNC mill (Syil America, Coos Bay, OR) into a 3D printer by attaching a custom hot-melt pressure extruder to the spindle of the mill. An Ultimus V (Nordson EFD, Providence, RI) regulator controlled the extruder pressure and a nozzle heater maintained the melt temperature at a set value. The printer was run at a linear speed of 2.7 mm/s (determined through optimization

studies). PCL (Capa 6400; Perstorp, Perstorp, Sweden) was used in pellet form for printing. The printer dispensed PCL through a 460 μm diameter nozzle onto a heated bed. The temperature of the bed was maintained at roughly 40 °C to ensure that the bottom layer of PCL remained attached to the printed surface and did not warp as the print cooled. A 120 mm fan was used to cool the scaffold during printing. Initially, cuboidal scaffolds (15 by 15 by 5 mm) were generated as computer-aided design models, exported as stereolithography (STL) files, and imported into Slic3r, an open-source program used to generate machine g-code. We varied the infill density from 20% to 80% to generate scaffold with varying pore sizes.

*3.1.2. Analysis of scaffold micro-architecture*

Pores were analyzed using scanning electron microscopy (SEM). Samples were sputter-coated with platinum and imaged at 25X and 55X magnifications on a JEOL 6700F microscope (JEOL USA, Peabody, MA). The 25X magnification images were used to measure the pore size.

*3.1.3. 3D printing of anatomical shapes*

A computerized tomography (CT) head scan of a child was imported into Mimics (Materialise, Leuven, Belgium) and 3D models of the maxilla and mandible were segmented by hand using the default bone thresholding setting. Models were smoothed and wrapped to fill any large holes, while ensuring that important surface details were not lost. The models were exported as STL files and g-code was generated in Slic3r using an infill density of 40%. Both models were printed with automatically generated support

structure. All support structure was printed with the same PCL material. The support structures were trimmed away after the completion of the print.

## 3.2. Results: 3D printing of PCL scaffolds

### *3.2.1. Scaffold characterization*

Scaffolds at all porosities were rectangular, although higher infill densities yielded more geometrically accurate scaffolds (**Figure 3.1**). At low infill densities, the fiber being printed had fewer attachment points to the layer beneath it, meaning it could easily be displaced when the printer made rapid movements. This can be observed in the top left corner of the 20% scaffold.

### *3.2.2. Anatomically shaped scaffolds*

After trimming away the support structures, the anatomically shaped scaffolds closely resembled the 3D models from which they were printed (**Figure 3.2**). All gross anatomical features were replicated in the scaffolds, with consistent, regular pores maintained throughout.

## 3.3. Discussion: 3D printing of PCL scaffolds

The 3D printing technology was applied to clinically relevant geometries for craniofacial bone. In particular, we explored the potential to generate porous scaffolds that replicated the incredibly complex anatomies of the mandible and maxilla. These scaffolds faithfully replicated complicated geometric features on each of these bones such as the temporomandibular joint (TMJ) condyle and the maxillary opening to the nasal

cavity observed in the 3D models; furthermore, the anatomically shaped scaffolds maintained the same level of porosity observed in the rectangular scaffolds, allowing for potential cell seeding.

The fabrication of these scaffolds demonstrates the advantages of 3D printing technology over DCB scaffold production. In particular, the structures printed are much larger than are structures that can be obtained from trabecular bone; furthermore, the generation of 3D printer g-code is far easier than is the generation of CNC milling g-code for these geometries. The drawback of this approach is the lack of osteoinductivity of PCL, as compared to the bioactivity of DCB scaffolds. This limitation is shared among all synthetic polymers used in 3D printing of scaffolds, such as poly[lactic acid] or poly[glycolic acid] [78].

Functionalizing synthetic scaffolds to impart bioactivity, such as by incorporating appropriate osteoinductive growth factors [79] or incorporation of mineral phases [80-83], have had some success in overcoming this challenge; however, despite often requiring supraphysiological doses of factors, these approaches do not recapitulate the full bioactivity of bone. Namely, they do not include the collagenous phase of bone, which has been shown to enhance osteogenesis in dogs when combined with tricalcium phosphate implants compared with tricalcium phosphate alone [84]. The eBM/DCB study outlined in Chapter 2 using collagen resulted in increased cell migration throughout the scaffold [85]. In this next part of the chapter, we hypothesized that by incorporating DCB particles into PCL, we could create a hybrid DCB:PCL material that incorporates both mineral and collagenous bioactive phases of bone, maintains the osteoinductive and osteoconductive properties of DCB, and is readily manufactured by 3D printing. The

objectives of this study were to (1) evaluate print quality of 3D printed hybrid scaffolds at different DCB:PCL ratios, (2) determine the mechanical properties of hybrid scaffolds, (3) characterize the ability of human ASCs to adhere to the DCB:PCL hybrid material, (4) assess the ability of DCB:PCL scaffolds to differentiate resident ASCs to bone, and (5) assess the ability of the DCB:PCL material to regenerate bone in an orthotopic cranial defect.

## 3.4. Materials and methods: hybrid material studies

### *3.4.1. Creation of hybrid material*

Trabecular bone was obtained from the subchondral region of 0.5- to 4-month-old calves. Decellularization proceeded as previously described [53, 85]. Bone was first subject to a high-pressure water jet to wash out the marrow. Then, bones were washed with phosphate-buffered saline (PBS; Cellgro, Manassas, VA) containing 0.1% w/v ethylenediaminetetraacetic acid (EDTA; Sigma Aldrich, St. Louis, MO) for one hour at room temperature and them overnight with PBS containing 0.1% w/v EDTA and 10 mM Tris (Sigma Aldrich) at 4 °C. Bones were then washed for another hour in PBS before being subjected to a wash consisting of PBS with 10 mM Tris and 0.5% sodium dodecyl sulfate (SDS; Sigma Aldrich) for 1 day at room temperature. The SDS was removed with extensive PBS washes and then the bones were washed with PBS containing 10 mM Tris, 50 U/mL DNAse (Roche Applied Science, Indianapolis, IN), and 1 U/mL RNAse (Roche Applied Science) for 5 hours at room temperature. Enzymes were removed with extensive PBS and water washes before storage via lyophilization.

Decellularized trabecular bone was pulverized using a SPEX SamplePrep 6770 cryo-mill (SPEX SamplePrep, Metuchen, NJ) at a frequency of 10 cycles per second for 15 minutes to obtain bone particles. The particles were then run through a 40 μm cell strainer to confine maximum particle size to 40 μm, a step performed to minimize risk of particle aggregation and clogging of the printer nozzle. This size of particles was confirmed via scanning electron microscopy (SEM; **Figure 3.3**). Resulting bone particles were mixed with PCL powder with molar mass 43000 – 50000 g/mol (Polysciences Incorporated, Warrington, PA) for printing.

*3.4.2. Scaffold fabrication and evaluation of print quality*

Hybrid mixtures consisting of 0%, 5%, 30%, 70%, and 85% bone by mass were created and printed at 80 °C into 0.644-mm height (2-layer), 4-mm diameter scaffolds of 60% porosity using our custom 3D printer [86]. These parameters resulted in strut diameters of 460 μm and pore sizes were approximately 800 μm. This geometry was chosen to be consistent with the geometry required for the in vivo studies outlined below. Scaffold pore size was selected due to optimizations performed in a previous study in which 60% porosity was shown to yield the most uniform cell distribution during seeding [86]. Scaffolds were stained with Alizarin Red S (Sigma Aldrich) to confirm the presence of mineralized particles and imaged under brightfield and SEM. Low-magnification brightfield images of scaffolds were compared pixel-by-pixel to a computer-generated ideal lattice. The percentage of pixels that matched between the two images was normalized to 50% to account for random matching and this numerical score, ranging from 0 to 100, was taken as a measure of print quality.

*3.4.3. Raman spectroscopy*

To determine the molecular constituents of the hybrid material and confirm the presence of both the mineral and collagen phases of the DCB particles, Raman spectroscopy was utilized as previously described [87]. Briefly, a 830 nm laser (Process Instruments, Salt Lake City, UT) was used to deliver light to a sheet consisting of 30% bone by mass. Background subtraction and normalization was performed using a barium sulfate spectrum and wavenumber assignment was performed using a Tylenol spectrum. As controls, the spectra of pure PCL and a block of DCB were also obtained.

*3.4.4. Atomic force microscopy*

To determine the surface roughness of the hybrid material, atomic force microscopy (AFM) was performed on printed sheets of 0%, 30%, and 70% bone by mass using a Dimension 3100 AFM (Bruker Nano, Santa Barbara, CA) in tapping mode with Bruker Nano probe model RTESPW. The root mean square roughness of nine 2 μm by 2 μm square regions on each sample surface was measured at 15 Hz and averaged to determine the roughness of that sample.

*3.4.5. Mechanical testing*

Solid cubes of 0%, 30%, and 70% bone by mass, 1.25 cm on all sides, were printed and subjected to unconfined compression using an EnduraTEC ELF 3200 system (Bose Corporation, Framingham, MA). As the specimens were solid, mechanical properties were assumed to be isotropic and compression of up to 5% static strain was

applied along the print axis, termed the *z*-axis, to determine compressive modulus of the bulk material. Resulting expansion along the perpendicular *x*-axis was also measured to determine Poisson's ratio.

To measure scaffold properties, porous cubes of 60% porosity and 1.25 cm on all sides were also printed. Due to the print layers, the properties along the *z*-axis differ from that of the other two axes; thus, the mechanical properties were assumed to be transversely isotropic. As such, compressive moduli were measured in both the *z*- and *x*-directions. Shear moduli were also measured with respect to the *x*-face along the *z*-direction.

### *3.4.6. Measurement of cell adhesion strength*

As a measure of cell interaction with the hybrid material, the strength of cell adhesion to the hybrid material was quantified by a modification of a centrifugation assay described previously [88, 89]. Briefly, fluorescently-labeled cells were allowed to adhere to printed sheets of 0%, 30%, and 70% bone by mass for 24 hours. Sheets were affixed onto a glass microscope slide using cyanoacrylate glue with the cells facing away from the slide. Slides were then immersed in PBS and subject to centrifugation at different speeds. The position of the sheet on the slide relative to the centrifuge rotor as well as the centrifugation speed determined the shear stress applied to the cells [88]:

$$\sigma = \|\vec{\omega}\|^2 y r_r (\Delta\rho) \tag{3.1}$$

where $\sigma$ is shear stress, $\vec{\omega}$ is angular velocity of the centrifuge where double bars denote vector magnitude, $y$ is the average height of adhered cells as determined by microscopy, $r_r$ is the distance from the rotor of the centrifuge, and $\Delta\rho$ is the difference in density between a cell and the surrounding PBS. The fraction of remaining cells after each spin was plotted against the shear stress applied during that spin and this data was fit to a variable-slope concentration response model (VSCR; Eqn. (3.2), [88, 90, 91]) to obtain a value for $\sigma_{50}$, the shear required for 50% of the cells on the sheet to detach:

$$f = \frac{\sigma^a}{\sigma^a + \sigma_{50}^a} \tag{3.2}$$

where $f$ is the fraction of cells adhered and $a$ is a cooperativity coefficient of detachment. Sheets composed of each DCB concentration ($n$ = 4) were tested and the 4 values of $\sigma_{50}$ were averaged for each material composition.

*3.4.7. Measurement of osteoinductivity*

To measure the ability of hybrid scaffolds to induce resident cells to undergo osteogenesis, human ASCs of passage 2 were seeded into fibrin gels at 20 million cells per milliliter and 5 μL gels were implanted into scaffolds of 0%, 30%, and 70% DCB by mass. Seeding proceeded as previously described with fibrinogen concentration 10 mg/mL, thrombin concentration 10 U/mL, and volume ratio 4:1 fibrinogen : thrombin for a final fibrinogen concentration of 8 mg/mL and a final thrombin concentration of 2 U/mL. Scaffolds were 0.644 mm in height, 4 mm in diameter, and had 60% porosity. Scaffolds were sterilized by ethanol wash for 1 hour at room temperature. ASCs were

obtained as described previously [92, 93]. All lipoaspirate obtained to isolate ASCs were obtained under Institutional Review Board approved protocols with patient consent. Briefly, lipoaspirate was digested with 1 mg/mL collagenase I (Worthington Biochemical Corporation, Lakewood, NJ) for 1 hour at 37 °C. The released cells were centrifuged to obtain the stromal vascular fraction pellet and plated. Adherent cells were termed ASCs and expanded for the current study. Expansion conditions consisted of Dulbecco's Modified Eagle Medium (DMEM; Life Technologies, Frederick, MD) with 4.5 g/L glucose, 10% v/v fetal bovine serum (FBS; Atlanta Biologicals, Flowery Branch, GA), 100 U/mL penicillin and 100 µg/mL streptomycin (Cellgro), and 1 ng/mL basic fibroblast growth factor (PeproTech, Rocky Hill, NJ).

After seeding the scaffolds of 0%, 30%, and 70% DCB by mass, constructs were cultured for 1 and 3 weeks under control conditions: DMEM with 1 g/L glucose, 100 U/mL penicillin and 100 µg streptomycin, and 6% v/v FBS. The absence of osteoinductive factors ensured that only the scaffold could induce osteogenesis within resident cells. After the culture periods, cells were digested with TRIzol (Life Technologies) and isolated mRNA was used to produce cDNA. cDNA was subject to real-time polymerase chain reaction (RT-PCR) for osteogenic genes Runx2, osteocalcin (OCN), and osteonectin (ON). For analysis, the delta-delta Ct method was used in which β-actin served as the housekeeping gene and gene expression under pure PCL scaffolds served as the control group.

As an additional measure of osteoinductivity, constructs were also cultured for 3 weeks under osteogenic conditions, which consisted of control conditions supplemented with 10 mM β-glycerophosphate (Sigma Aldrich) and 50 µM ascorbic acid (Sigma

Aldrich). These constructs were subject to the Quant-iT PicoGreen dsDNA assay (Invitrogen, Carlsbad, CA) and the Stanbio LiquiColor calcium assay (Stanbio, Boerne, TX) to determine calcium content normalized to cell number.

*3.4.8. In vivo assessment of bone regeneration*

To determine the effect of the hybrid scaffolds in vivo, the critically sized murine calvarial defect model was used as previously described [94, 95]. All procedures were reviewed and approved by the Johns Hopkins Animal Care and Use Committee. Briefly, a 4-mm circular knife (Medicon, Tuttiligen, Germany) was used to excise a 4-mm disk of calvaria between the coronal and lambdoid sutures and 1 mm lateral to the sagittal suture with care taken to preserve the underlying dura mater. This size has been shown previously to be non-healing [94, 95]. Constructs consisting of ASCs seeded in fibrin inside scaffolds of 0%, 30%, and 70% bone by mass created as in the previous section were immediately implanted into the resulting defect. A total of 12 mice were operated on with $n = 4$ for each concentration of bone. The contralateral side served as unoperated controls. Mice were imaged under computed tomography (CT) using a Gamma Medica X-SPECT small animal system (Gamma Medica, Salem, NH) at 6 and 12 weeks post-implantation. Imaging was performed at 80 kV peak voltage and 600 μA current. Reconstruction was done with voxel size 100 μm. At 12 weeks post-implantation, scaffolds were excised and fixed under 3.7% formalin overnight for histological analysis. Histological analysis consisted of a haematoxylin/eosin (H&E) stain for cellularity (Sigma Aldrich) and a von Kossa/van Gieson stain for bone formation (Sigma Aldrich).

## 3.5. Results: hybrid material studies

### *3.5.1. Print quality*

DCB:PCL scaffolds of 0%, 5%, 30%, 70%, and 85% bone by mass were printed and stained with Alizarin Red S. We observed staining in all scaffolds except in the 0% scaffold where no mineral was present, confirming the presence of bone particles within the hybrid scaffolds. The intensity of the red stain increased with increasing DCB concentration (**Figure 3.4**). When compared to a computer-generated ideal lattice, the print quality decreased as the concentration of bone increased from a score of roughly 89 for 0% and 5% DCB scaffolds to 77.6 for 70% DCB scaffolds; however, a dramatic drop in score (50) was observed at 85% DCB (**Table 3.1**). As such, for all subsequent studies 70% bone by mass was chosen as the maximum concentration of bone. 0% bone by mass was chosen as a pure PCL control, whereas 30% bone by mass was chosen as an intermediate group.

### *3.5.2. Raman spectroscopy*

To confirm whether mineral and collagen were presented on the surfaces of 3D printed DCB:PCL, we employed Raman spectroscopy (**Figure 3.5**). Raman spectroscopy of a printed sheet of 30% bone by mass showed a peak at 960 $cm^{-1}$ corresponding to the phosphate component of bone and a peak at 1650 $cm^{-1}$ corresponding to the amide I signal from collagen [96]. These peaks appear in the Raman spectrum of trabecular bone but not in the spectrum for pure PCL (**Figure 3.5**), matching observations reported previously [97]. The contributions from the PCL phase include the triple peak centered around 1450 $cm^{-1}$ for $\delta CH_2$ (fourth carbon from the carbonyl), the double peak at 1300

$cm^{-1}$ for $\omega CH_2$ (furthest carbon from the carbonyl), and the skeletal stretching peak at 1110 $cm^{-1}$ [97, 98], signals appearing in both the spectrum for pure PCL (**Figure 3.5**, top) and in the spectrum for the 30% bone by mass sample (**Figure 3.5**, **bottom**).

*3.5.3. Atomic force microscopy*

SEM had revealed that the surfaces of 30% and 70% scaffolds displayed more features than did the 0% scaffolds, whose surfaces were mostly smooth (**Figure 3.4**). To quantify the surface roughness of scaffolds, which is known to affect cell-biomaterial interactions [99-101], AFM was performed and the root mean square roughness of 0%, 30%, and 70% scaffolds were computed. At the length scale of AFM, we found no significant difference between 30% and 70% scaffolds: both had roughness values around 50 nm. Both 30% and 70% scaffolds were significantly rougher than were 0% scaffolds, which showed a surface roughness of 4.83 nm (**Figure 3.6**), confirming observations under SEM.

*3.5.4. Mechanical properties*

To determine how the bone particles affected the mechanical properties of the hybrid material, we first tested the compressive properties of bulk material. 0% and 30% blocks had similar compressive moduli of around 30 MPa, whereas 70% blocks showed a significant drop in modulus to around 10 MPa. The Poisson's ratio of approximately 0.3 did not differ significantly between the three groups (**Figure 3.7**, **top**). The same trend held for the compressive and shear moduli of 60% porous scaffolds. The compressive modulus in the *x*-direction was similar for both 0% and 30% scaffolds at around 15 MPa,

while the modulus for 70% scaffolds was around 7 MPa. In the *z*-direction, 0% and 30% scaffolds had moduli approaching 10 MPa, whereas 70% scaffolds had moduli approaching 5 MPa (**Figure 3.7**, **bottom**).

### *3.5.5. Cell-biomaterial adhesion*

We next characterized cell adhesion to the hybrid material as an indicator of cell-material interactions. The centrifuge-applied shear successfully detached cells in a force-dependent manner and the VSCR model fit the data well (**Figure 3.8**, **top**). The shear for half-detachment, $\sigma_{50}$, was significantly different between all three groups (**Figure 3.8**, **bottom**), increasing in a concentration-dependent manner from 87.2 mPa for pure PCL adhesion to 28.2 Pa for adhesion to 70% bone by mass. This observation is well-supported by the surface biomolecular data (**Figure 3.5**) and the surface roughness data (**Figure 3.4** and **Figure 3.6**).

### *3.5.6. In vitro osteoinductivity*

Since the goal of this study was to enhance bone regeneration, we next examined the ability of hybrid scaffolds to induce resident cells to form bone. By 3 weeks of culture, Runx2 expression increased by more than 3 orders of magnitude while OCN and ON expression increased by about 5 orders of magnitude compared to PCL alone despite the absence of soluble osteoinductive factors in the culture medium (**Figure 3.9**). Since no phosphate source was present, this increase in gene expression did not yield calcium production; however, when a phosphate source was added with ascorbic acid and constructs culture for 3 weeks, the hybrid scaffolds displayed higher calcium production

per cell relative to pure PCL controls, with 70% scaffolds yielding 88.0 ng/cell and 30% scaffolds yielding 48.1 ng/cell compared to 35.3 ng/cell from pure PCL scaffolds (**Figure 3.9**). Since little to no calcium was detected in samples under no phosphate, it can be surmised that the calcium content innately present in the hybrid scaffolds was not being detected by the assay.

*3.5.7. In vivo osteoinductivity*

As a final assessment of the osteoinductive properties of hybrid scaffolds in comparison to pure PCL scaffolds, scaffolds of 0%, 30%, and 70% bone by mass were fabricated and seeded with ASCs as was done in the in vitro experiment. Resulting constructs were implanted in 4-mm murine calvarial defects. CT scans at both 6 and 12 weeks post-implantation revealed that hybrid scaffolds invoked nearly twice the volume of regenerated bone compared to pure PCL scaffolds (**Figure 3.10**), with hybrid scaffolds approaching 4 $mm^3$ of regenerated bone compared to 2.07 $mm^3$ regenerated bone with pure PCL scaffolds. The pattern of signal detected by CT within the defect suggested that the system was not picking up the mineral innately present within the hybrid scaffolds, as the detected bone was punctate and isolated rather than ubiquitously present within the scaffolds struts (which were not visible under CT). CT scans also revealed that regenerated bone was appearing both in the scaffold centers as well as from the edges, suggesting that both implanted cells within the scaffold and invading cells from the host were contributing to repair. Histological analysis (**Figure 3.11**) revealed both non-mineralized osteoid and mineralized tissue, visualized by the van Gieson and von Kossa

stains, respectively, indicating that bone regeneration was actively occurring within the defect.

*3.5.8. 3D printing of anatomical geometry*

To demonstrate the ability of the approach described here to create anatomical shapes, the geometry of the human temporomandibular joint condyle was extracted and printed using pure PCL as well as 30% bone by mass. The scaffolds printed successfully and were subject to Alizarin Red S staining to confirm the presence of bone mineral (**Figure 3.12**). While the pure PCL condyle did not stain, as expected, robust staining was observed in the 30% bone by mass condyle, demonstrating that 3D printing of hybrid material can be used to fabricate complex craniofacial geometries.

## 3.6. Discussion: hybrid material studies

In this study, hybrid scaffolds consisting of bone particles embedded in a greater PCL phase were printed using a custom 3D printer. To our knowledge, this is the first time a bone engineering hybrid scaffold has been fabricated by 3D printing of naturally derived matrix. While being readily printable, hybrid scaffolds are more amenable to cell adhesion compared to pure PCL scaffolds and are osteoinductive both in vitro and in vivo. As such, the hybrid material developed here mitigates the lack of osteoinductivity and osteoconductivity in pure PCL while simultaneously overcoming the manufacturing challenges associated with producing a pure DCB scaffold.

We considered mechanics as a potential limiting factor in the use of this hybrid material, as mechanical properties for bone engineering scaffolds are crucial due to the

role of bone as a load-bearing tissue. The choice of PCL as a biomaterial partly arises from this consideration, as its mechanical properties (stiffness on the order of $10^7$ Pa) fall within the range reported for trabecular bone, 0.5 to 14.6 MPa [68, 102]. Even with the drop in properties at 70% DCB by mass, the stiffness values reported for DCB:PCL scaffolds still approach the values of trabecular bone and are within the range reported in the literature for pure PCL 3D printed scaffolds [103, 104]. Composite collagen/calcium phosphate printed scaffolds were reported to have a modulus of approximately 15 MPa, comparable to the values in the present study [62]; however, it should be noted that the porosity in the present study – an important property for highly osteoconductive scaffolds – is much greater in comparison while retaining appropriate moduli. Taken together, this data suggests that mechanics are not a limiting factor in the use of these hybrid scaffolds in bone engineering.

Next, we examined the interactions between human stem cells and the hybrid material. We investigated two important aspects of cell-biomaterial interactions: cell adhesion to biomaterials has extensively been studied and affects many aspects of cell behavior, while cell migration through a biomaterial scaffold is crucial for a uniformly-seeded graft as well as for recruitment of host cells to the implant. The SEM and AFM data on surface roughness indicated that this was a feature of the printed hybrid material that could enhance cell adhesion at different length scales – the micrometer scale as shown under SEM and the nanometer scale as shown under AFM. Meanwhile, the presence of collagen as confirmed by Raman spectroscopy suggested that an increased number of binding sites could be a second mode by which the hybrid material could enhance cell adhesion. The data demonstrates increasing cell adhesion strength with

higher concentrations of bone in the scaffolds. In comparison, the shear forces required for half-detachment of ASCs seeded on scaffolds containing 70% bone by mass (~30 Pa) agrees well with previous studies on cell adhesion to hydroxyapatite [105]. While it should be noted that the values reported here for initial cell numbers reflect a combination of initial adhesion and proliferation after 1 day, the trend that higher concentration of DCB leads to increased $\sigma_{50}$, an effect of surface roughness, the presence of collagen, or both, remains true.

The RT-PCR data are derived from ASCs grown in scaffolds in vitro and provide evidence that hybrid scaffolds are innately osteoinductive. The RQ values reported are normalized to expression in pure PCL scaffolds, where no osteoinductive cues were present and little expression of osteogenic genes is expected. Interestingly, the osteogenic gene expression in hybrid DCB-PCL scaffolds increased compared to pure PCL scaffolds despite the absence of soluble osteoinductive factors in the culture medium. The observation that calcium per cell increases in hybrid scaffolds relative to that in pure PCL scaffolds demonstrates the ability of the hybrid scaffold to enhance the osteogenic capability of resident ASCs. The changes in bone volume following transplantation of ASC-seeded scaffolds into orthotopic defects also supported the hypothesis that hybrid scaffolds are osteoinductive compared to pure PCL scaffolds. Note that in that particular experiment, the cells were not provided any soluble osteoinductive cues prior to implantation. Consequently, differentiation cues were provided solely by the DCB-PCL hybrid scaffolds. The percent of bone regenerated in the current study is also comparable to previous studies where PCL/tricalcium phosphate/collagen scaffolds were implanted into rat calvariae [106].

In examining the spatial profile of the bone formed, bone is visible both in the scaffold pore spaces and in the scaffold edges. As such it is possible to speculate that two factors are at play: bone being regenerated from the implanted human cells as well as bone regenerated from endogenous murine cells. While it is outside the scope of this study to distinguish between these two sources of regeneration, future studies may examine this further. It is worth noting that the hybrid scaffold potentially enhances both these avenues of regeneration due to both mineral and collagenous phases enhancing osteoinductivity and osteoconductivity.

While we have demonstrated here a printable, bioactive scaffold, future optimizations may be performed. First, the particle size of DCB was chosen at a maximum of 40 μm in the current study to reduce the chance of particle aggregation blocking flow from the print nozzle, which has a diameter an order of magnitude above this size. In the current study, this particle size resulted in successful prints of bioactive scaffolds; however, it is possible that smaller particle sizes may further increase the amount of bone that can be printed as nozzle clogging becomes less of an issue and smaller particles may have lower impact on the rheological properties of PCL. Another effect of particle size is the nanotopography of the scaffold, which we have shown here is affected at the nanoscale despite the microscale of the particles. Nanoscale changes in topography have been shown to affect the expression of osteocalcin in MSCs [99], while the use of nanotopography to control cell shape was shown to modulate BMP-dependent osteogenesis [107]. Another effect of particle-mediated nanotopography is the potential for the particles to serve as nucleation sites for the deposition of mineral, leading to

enhanced bone formation [108]. Taken together, this suggests that the DCB particle size alone may also play a role in enhancing the osteogenesis of seeded stem cells.

Second, the method of printing chosen here, melt extrusion, was selected due to its ease of use. Effectively, PCL was used as a "binder" to hold the DCB together. Other methods that have fabricated composite scaffolds, such as with synthetic ceramics, have used acidic binders that unfortunately result in decreased cell viability as well as smaller pore size due to the increased flow of acidic binders away from the target print location [62]. It has been shown that smaller pore size inhibits the migration and proliferation of seeded and infiltrating cells [109]. As such, another advantage of the method used here is that PCL as the "binder" is readily printable, with minimal flow away from the target print location doe to high viscosity, and is not cytotoxic. One potential short-coming of this approach is the DCB is subject to 80 °C printing temperatures that destroy osteoinductive growth factors, such as BMP, that are known to reside in bone matrix [22, 23, 36]; however, many other methods of printing feature temperatures above this value, such as 1300 °C for sintering techniques [110]. Despite the elevated temperatures used in this study, the hybrid scaffolds produced in this study were still shown to be osteoinductive, likely due to the presence of the mineral phase; furthermore, the collagenous phase of bone was retained as shown by Raman spectroscopy. As such, the hybrid scaffold still represents an increase in bioactivity from pure PCL scaffolds while retaining printability. For the first time, bone matrix can be 3D printed into any of the complex shapes in the human skeleton, representing a potentially storable, patient-specific component to tissue engineered bone grafts.

# Tables: Chapter 3

| Concentration of bone (% mass) | Print quality (-) |
|---|---|
| 0 | 88.2 |
| 5 | 89.6 |
| 30 | 85.8 |
| 70 | 77.6 |
| 85 | 50.0 |

**Table 3.1**: Print quality of pure and hybrid scaffolds.

# Figures: Chapter 3

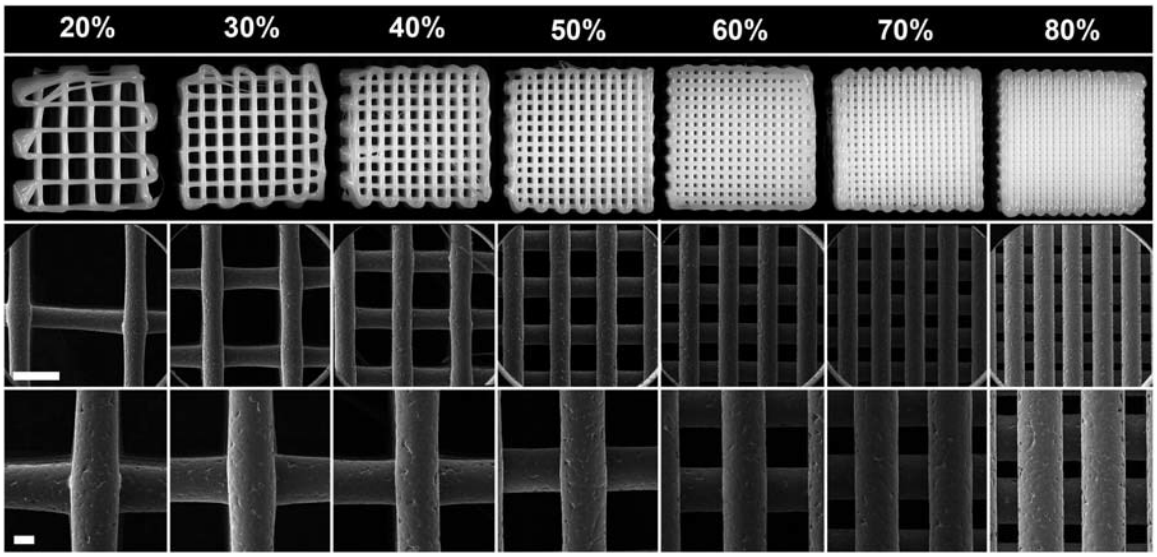


**Figure 3.1**: Scanning electron microscopy. **Upper row**: stereomicroscope images of 15 by 15 by 5 mm scaffolds with infill densities ranging from 20% to 80%. **Middle row**: SEM images taken at 25X magnification demonstrate the uniformity of the pores and fiber widths. Scale bar: 1 mm. **Bottom row**: SEM images at 55X magnification illustrate surfaces of fibers. Scale bar: 200 µm.

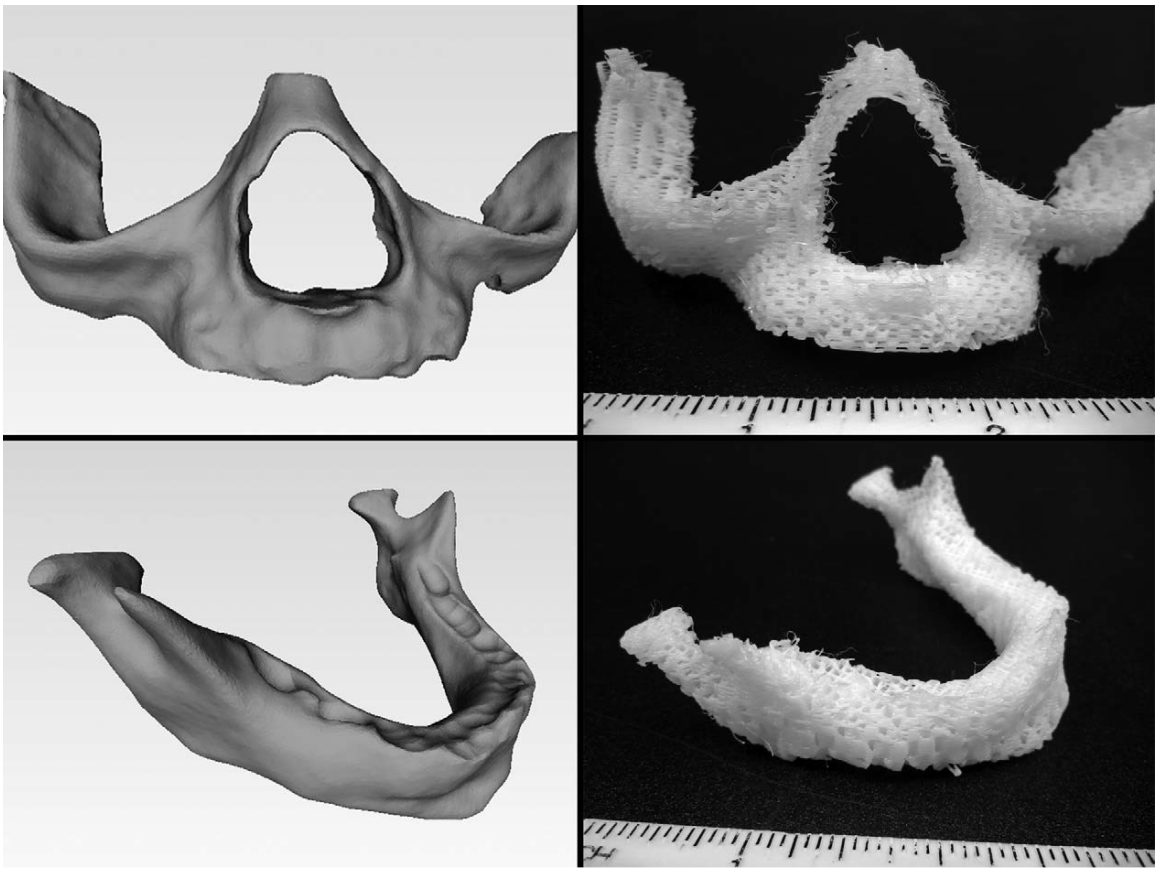

**Figure 3.2**: Anatomically shaped scaffolds. **Left**: Isolated 3D geometries of the maxilla (**top**) and mandible (**bottom**). **Right**: 3D printed, porous PCL scaffolds at 40% infill density.

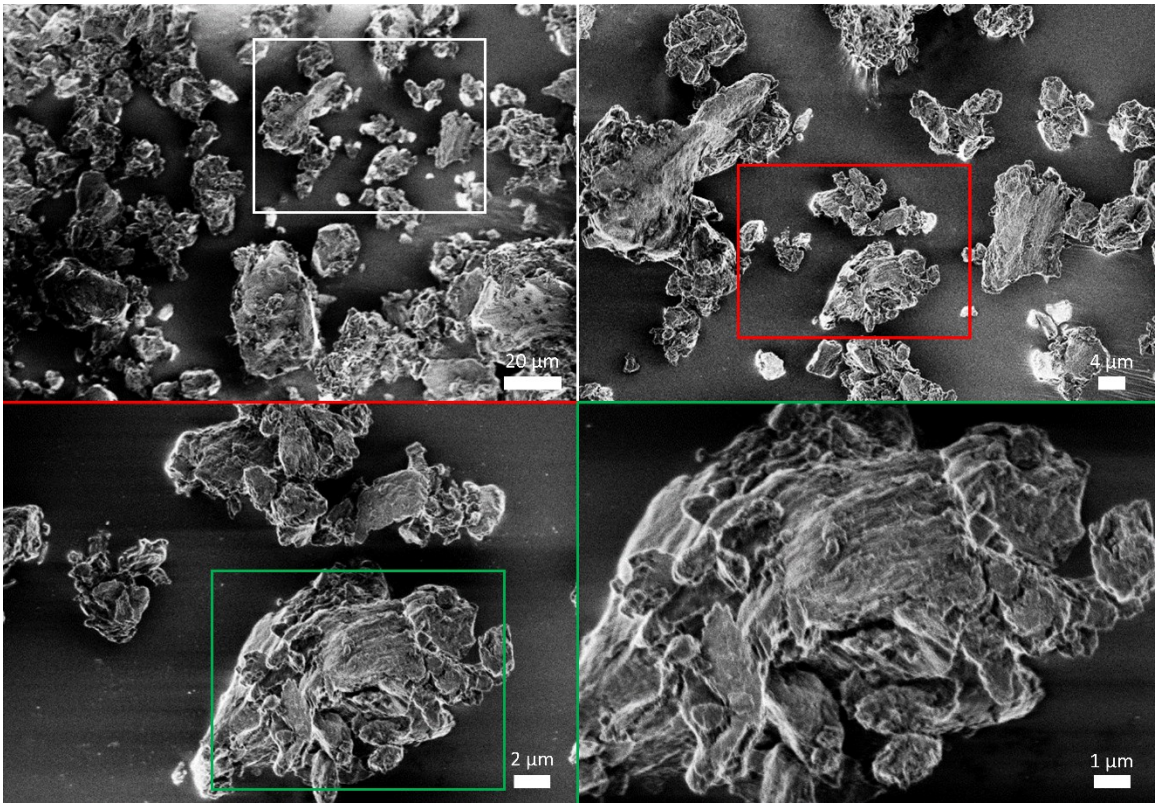


**Figure 3.3**: Scanning electron microscopy of cryo-milled bone particles that had been run through a 40 µm filter. Sizes of particles above 40 µm are absent. Colored boxes show images of increased magnification.

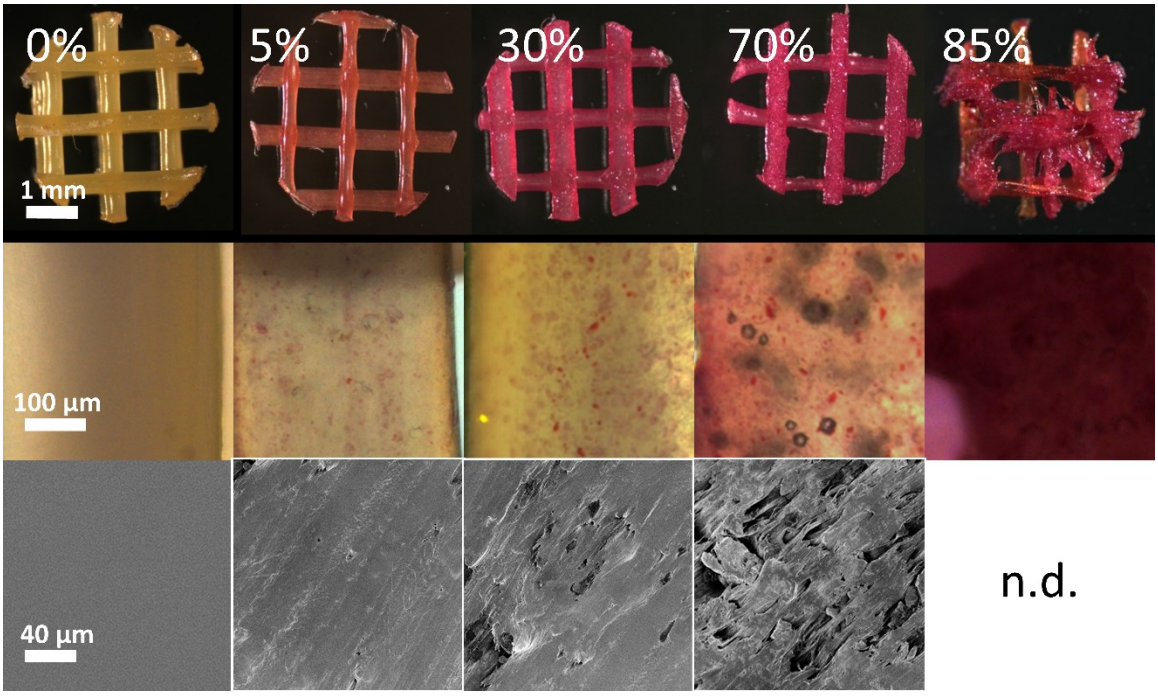


**Figure 3.4**: Imaging of 3D printed hybrid scaffolds. **Top**: Scaffolds stained positively for Alizarin Red S in all cases except for the pure polycaprolactone case. **Middle**: Magnified images of stained scaffold struts, delineating the punctate stain of the mineralized particles within the PCL. **Bottom**: Scanning electron microscopy of strut surfaces revealed rougher surface topographies in the more concentrated hybrid scaffolds.

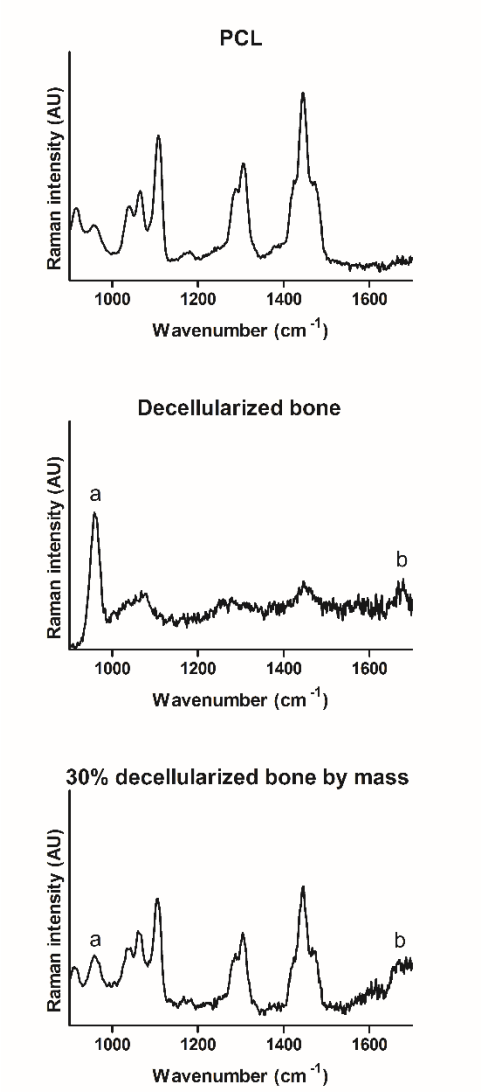


**Figure 3.5**: Raman spectroscopy of pure and hybrid material. **Top**: Raman spectra of pure polycaprolactone, revealing peaks at 1450 $cm^{-1}$ for $\delta CH_2$, 1300 $cm^{-1}$ for $\omega CH_2$, and 1110 $cm^{-1}$ for skeletal stretching. **Middle**: Raman spectra of decellularized trabecular bone, showing peaks at 960 $cm^{-1}$ for phosphate (a) and 1650 $cm^{-1}$ for collagen amide I (b). **Bottom**: Raman spectra of 30% DCB:PCL. The bone-only peaks as well as the peaks corresponding to contributions from both bone and polycaprolactone appear.

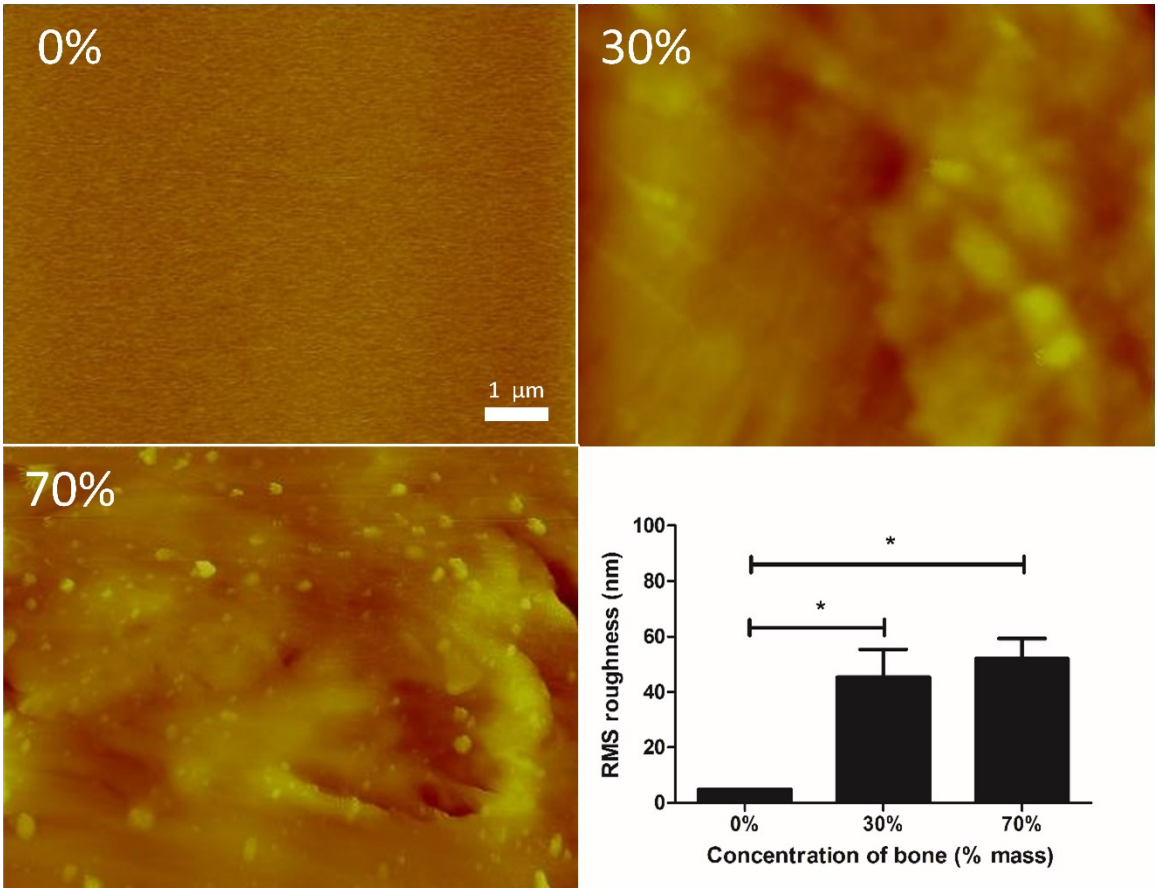


**Figure 3.6**: Atomic force microscopy of pure and hybrid material. **Top left**: The atomic force micrograph of pure polycaprolactone is mostly featureless, while surface features are rougher for 30% bone by mass (**top right**) and 70% bone by mass (**bottom left**). Quantification of root mean square roughness (**bottom right**) confirms these observations. *$p<0.05$ by one-way ANOVA with post-hoc Tukey test.

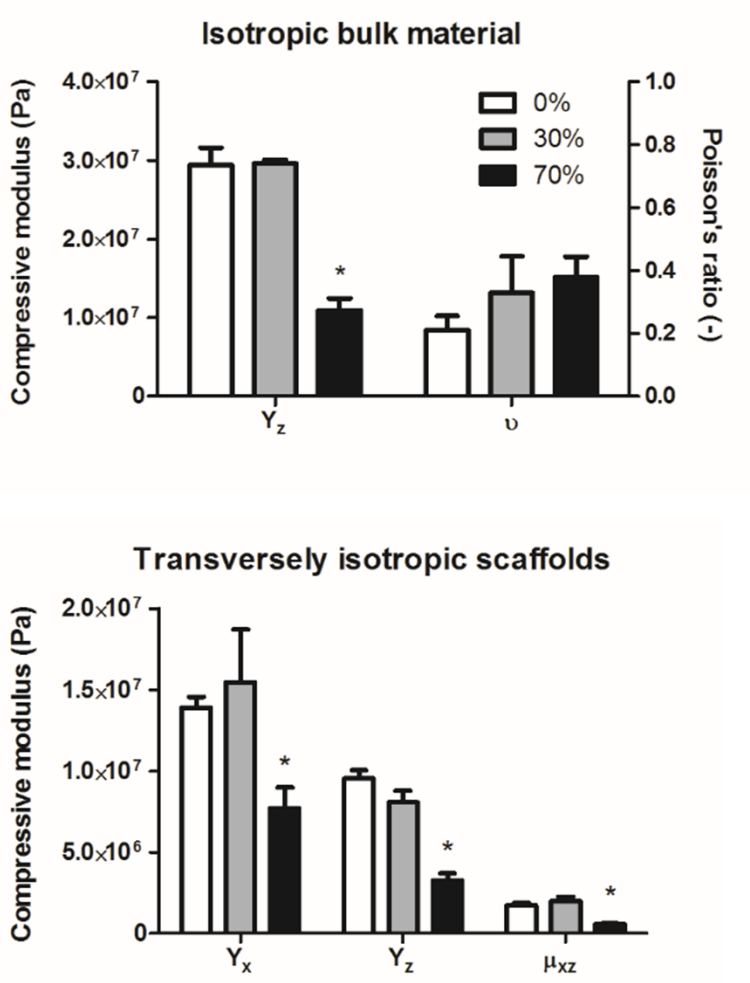


**Figure 3.7**: Mechanical testing of pure and hybrid material/scaffolds. **Top**: The Poisson's ratio of all groups were not significantly different from each other, while compressive modulus was significantly lower in the 70% group compared to both 30% and pure groups. **Bottom**: The same trend held for all directions in transversely isotropic porous scaffolds. *$p<0.05$ compared to pure polycaprolactone by one-way ANOVA with post-hoc Tukey test.

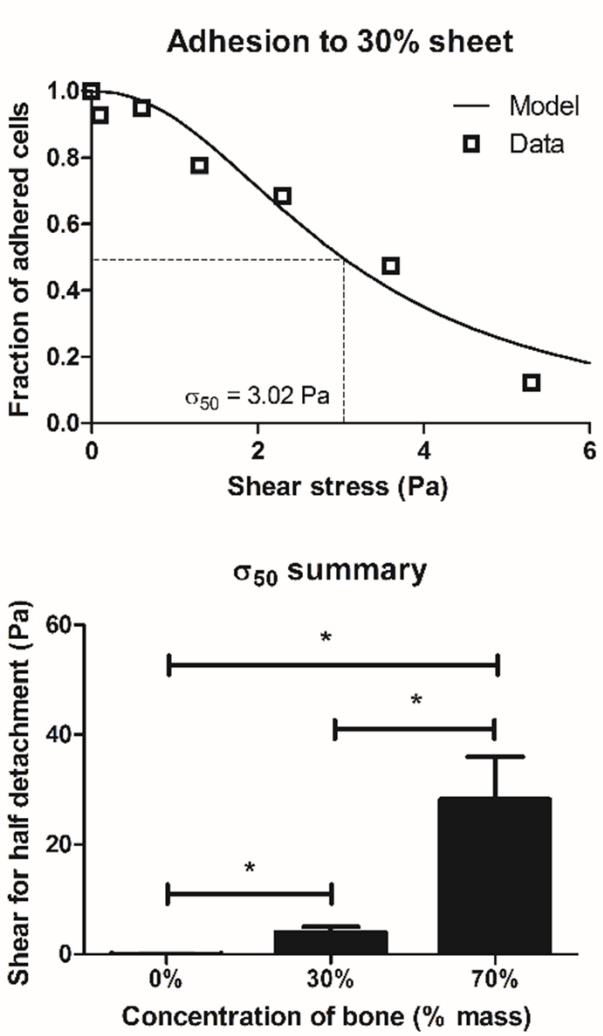


**Figure 3.8**: Cell adhesion to pure and hybrid material. **Top**: Representative graph of adhered cells plotted against shear with a variable-slope concentration response model fit to determine the shear for half-detachment, $\sigma_{50}$. **Bottom**: $\sigma_{50}$ increased in a dose-dependent manner with increasing bone concentration. *$p<0.05$ by one-way ANOVA with post-hoc Tukey test.

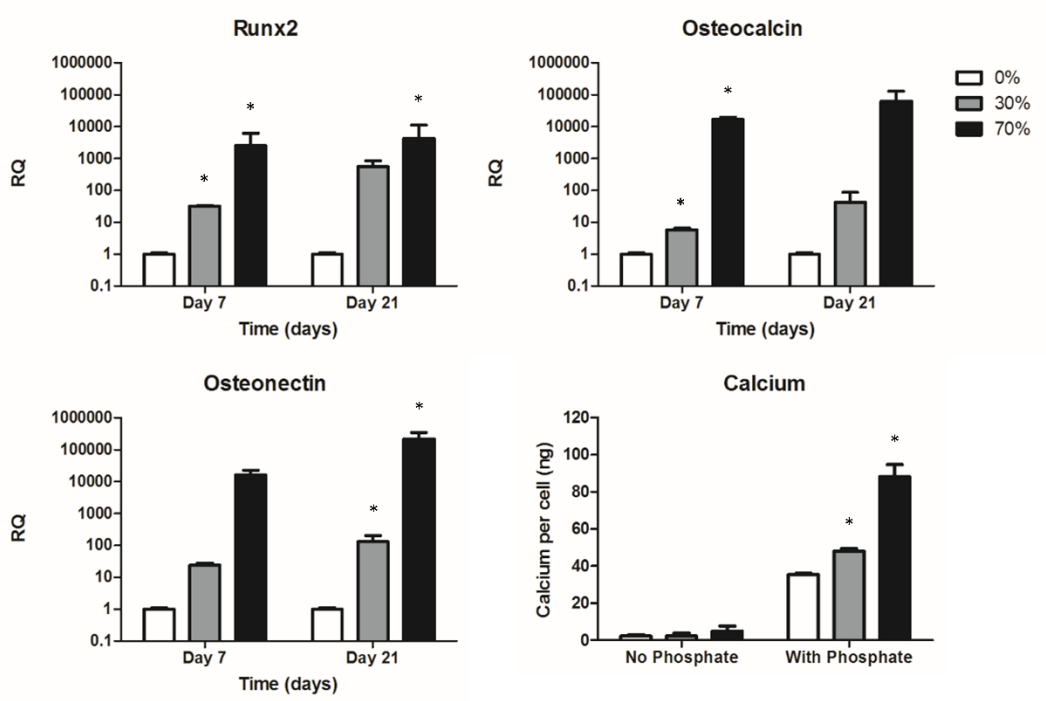


**Figure 3.9**: In vitro osteogenic gene expression. Gene expression of Runx2, osteocalcin, and osteonectin increased in cells cultured in hybrid scaffolds despite the absence of exogenous osteoinductive factors. **Bottom right**: With the addition of a phosphate source, calcium per cell production displayed the same trend. *$p<0.05$ compared to cells cultured in pure polycaprolactone scaffolds by one-way ANOVA with post-hoc Tukey test.

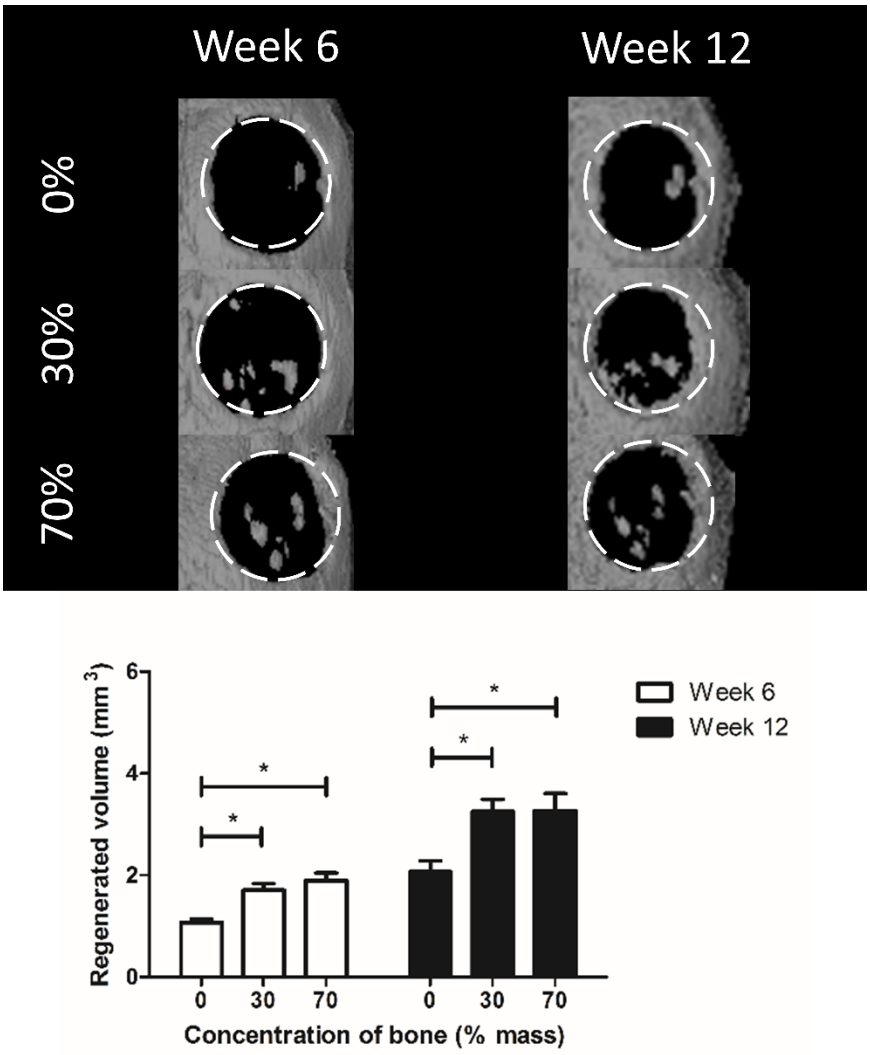


**Figure 3.10**: In vivo regeneration of murine calvarial defect. White dotted lines show boundaries of original defect. **Top**: Computed tomography scans at 6 and 12 weeks revealed increased bone regeneration in hybrid scaffolds compared to the pure polycaprolactone group. **Bottom**: Quantification of computed tomography scans showed a significant difference between hybrid groups and pure PCL groups, but no significant difference between the 30% and 70% groups. *$p<0.05$ by one-way ANOVA with post-hoc Tukey test.

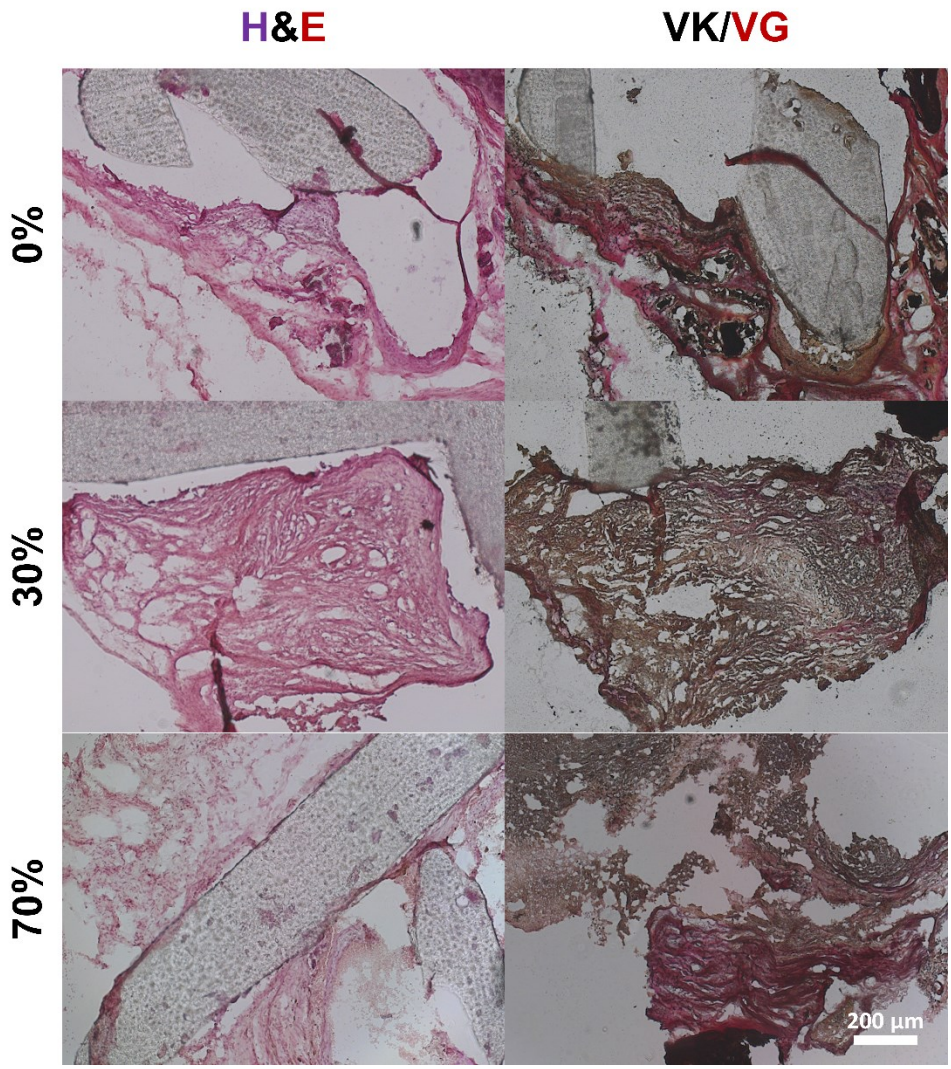


**Figure 3.11**: Histological analysis of excised constructs. Cellularity under haematoxylin/eosin staining (**left**) as well as bone and osteoid formation under the von Kossa/van Gieson stain (**right**) is evident.

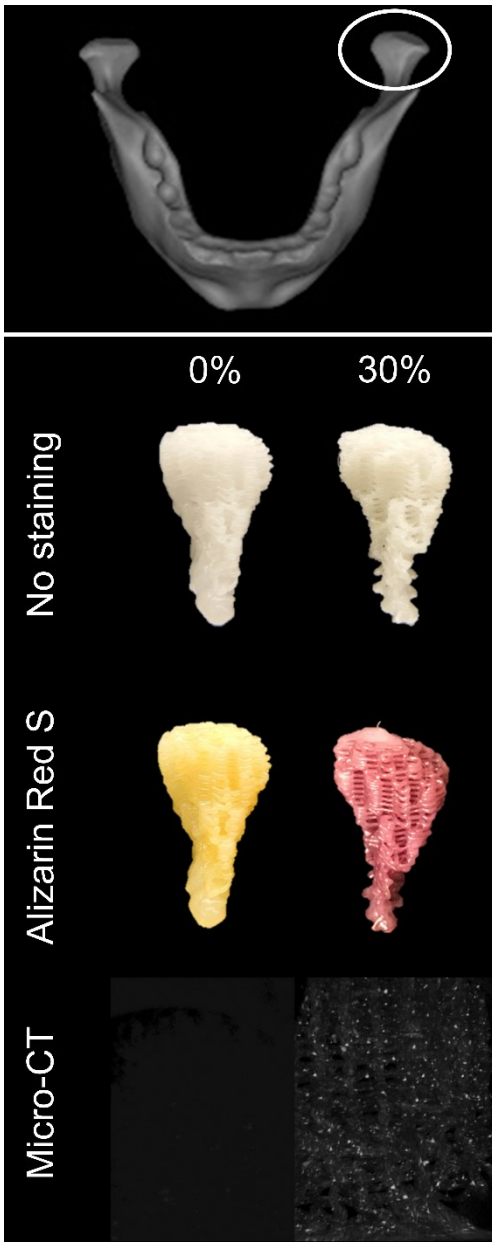


**Figure 3.12**: Anatomical shape printing of pure and hybrid scaffolds. A human temporomandibular joint condyle was isolated and printed into anatomically shaped, porous scaffolds. Scaffolds were subject to Alizarin Red S staining and micro-computed-tomography to confirm and visualize the presence of mineralized particles in the hybrid scaffold. As expected, mineralized particles were absent in the pure PCL scaffold.

# Chapter 4: adipose-derived stem cells and platelet-derived growth factor BB

This chapter draws from the following publications: (1) Tzeng SY, Hung BP, Grayson WL, and Green JJ. 2012. "Cystamine-terminated poly(beta-amino ester)s for siRNA delivery to human mesenchymal stem cells and enhancement of osteogenic differentiation." Biomaterials 33: 8142-8151; (2) Hung BP, Hutton DL, Kozielski KL, Bishop CJ, Naved BA, Green JJ, Caplan AI, Gimble JM, Dorafshar AH, and Grayson WL. 2015. "Platelet-derived growth factor BB enhances osteogenesis of adipose-derived but not bone marrow-derived mesenchymal stromal/stem cells." Stem Cells 33: 2773-2784.

## 4.1. Conflicting reports on PDGF-BB-mediated osteogenesis

As discussed in Chapter 2, section 2.5.2., the use of PDGF-BB to enhance ASC osteogenesis shows some promise. Previous studies into the osteoinductive potential of PDGF-BB were prompted by the observation of heightened PDGF-BB levels within bone fracture microenvironments [111, 112]; however, these studies have largely determined that PDGF-BB is not osteoinductive when signaling MSCs. In fact, PDGF-BB was shown to inhibit mineralization [113-116] and when the beta receptor for PDGF, PDGFRβ, was deleted using Cre-LoxP recombination, mineralization of MSCs was restored even in the presence of PDGF-BB [117]. In contrast, more recent studies showed a dose-dependent increase in calcification per cell in ASCs with signaled with PDGF-BB [73]. Consequently, ASCs have recently been used in fibrin matrices incorporating

PDGF-BB to exploit this finding [118]; however, to date, no direct comparison of MSCs and ASCs in their osteogenic response to PDGF-BB has been performed to resolve the apparent contradiction.

A potential difference between MSCs and ASCs is of high importance in the use of tissue engineering approaches to treat bone defects. PDGF-BB is a known mitogen [119] and chemoattractant [75] and it has been observed that injection of PDGF-BB into fracture sites accelerates bone healing [74]. Given the in vitro observations that PDGF-BB does not directly promote osteogenesis in MSCs, it is thought that PDGF-BB in this case is largely acting through recruitment of endogenous repair cells. The notion that PDGF-BB can directly enhance ASC mineralization, however, presents toe possibility that the use of ASCs in conjunction with PDGF-BB for bone repair can more efficiently make use of both the cellular and biomolecular components.

In this chapter, we hypothesize that the osteogenic response of MSCs and ASCs to PDGF-BB is different at a fundamental genetic level. To test this hypothesis, the objectives of this study are (a) to investigate the differences in osteogenic response of MSCs and ASCs at a cellular and genetic level, (b) to use siRNA-mediated knockdown of PDGFRβ for loss-of-function evidence that specifically PDGF-BB leads to enhanced mineralization of ASCs but not of MSCs, and (c) to demonstrate the application of this finding using ASCs overexpressing PDGFB in an in vivo murine calvarial defect model.

## 4.2. Development of an siRNA delivery vehicle

To accomplish objective (b), an siRNA delivery vehicle must be first developed. In finding a suitable approach, lipid-based materials are an option. Such materials

generally form liposome-like vehicles within which siRNA can be encapsulated and then carried [120]. Several groups have capitalized on this property of cationic lipid formulations for siRNA delivery [121, 122], using both natural and synthetic lipids to facilitate cellular entry via endocytosis or membrane fusion [123]. Because of the prevalence of their use in the field of siRNA delivery, although lipids are not a focus of this report, a lipidic product is used as a control in these studies. In particular, we compare our results here against results from Lipofectamine™ 2000, which has been widely used in the gene delivery literature as a leading commercial transfection agent. Many lipid-based materials, however, can be prohibitively cytotoxic [124] and unstable, especially in the presence of salts or serum [125]. The commonly used cationic polymer polyethyleneimine (PEI) must be chemically modified to avoid cytotoxicity [126] and, along with other methods like gold nanoparticle immobilization, also requires high siRNA doses of up to 200 nM [127, 128], even when using easier-to-transfect cell types such as CHO-K1 or HeLa cells.

Poly(β-amino ester)s (PBAEs) are an attractive non-viral method of gene delivery, as they are simple to synthesize, easily chemically modified, and hydrolytically degradable under physiological conditions [129-131]. Success in DNA delivery to MSCs has previously been shown [132], but the ability to deliver other biomolecules such as siRNA would expand the flexibility of the cationic polymer delivery system by allowing gene knockdown as well as upregulation. Other researchers have previously been unsuccessful in transfecting cells with PBAE-siRNA nanoparticles without the use of gold nanoparticles as a substrate [133]. Researchers using similar systems have used high siRNA doses of up to 125 nM, usually in the absence of serum in the transfection media,

to achieve moderate knockdown [134, 135]. Earlier studies of siRNA delivery to another hard-to-transfect primary human cell type have shown that polymers ideal for DNA delivery may not be the same as those necessary for siRNA delivery [131], likely due to differences in chemical and physical properties of the two types of nucleic acids as well as differences in their mechanisms of action [136]. As such, PBAEs optimized specifically for siRNA delivery must be identified. In the first part of the chapter, we synthesize, characterize, and evaluate an array of PBAEs for effective siRNA delivery to primary human MSCs. The ability to screen many PBAE formulations in a high-throughput manner provides a powerful tool not only to identify top formulations quickly but also to see trends in the relationship between polymer structure and function, thereby helping to refine results further and to direct studies in similar systems. This nanobiotechnology for siRNA delivery can be an enabling tool for control-based approaches to engineer biological systems [137].

As a model for knockdown, we transduced MSCs with lentivirus to overexpress enhanced green fluorescence protein (eGFP). We then transfected these cells with siRNA against eGFP (siGFP) using PBAEs, and monitored eGFP expression over time as a measure of knockdown efficiency. We ensured the transduced MSCs had not lost their potency by evaluating multilineage differentiation to ensure their suitability for future biological applications. Finally, to demonstrate the potential applications of our approach, we identified the leading nanoparticle formulation among those we developed and tested, utilized this formulation to deliver siRNA against an inhibitor of osteogenesis, B-cell lymphoma (Bcl)-like protein 2 (BCL2L2), and examined the effect on MSC osteogenic differentiation.

## 4.3. Materials and methods: development of an siRNA delivery vehicle

### *4.3.1. Materials*

Monomers used for polymer synthesis (**Figure 4.1**) include 1,3-propanediol diacrylate (B3; Monomer-Polymer and Dajac Labs, Trevose, PA); 1,4-butanediol diacrylate (B4; Alfa Aesar, Ward Hill, MA); 1,5-pentanediol diacrylate (B5; Monomer-Polymer and Dajac Labs); 1,6-hexanediol diacrylate (B6; Alfa Aesar); 3-amino-1-propanol (S3; Alfa Aesar); 4-amino-1-butanol (S4; Alfa Aesar); 5-amino-1-pentanol (S5; Alfa Aesar); 6-amino-1-hexanol (S6; Sigma Aldrich, St. Louis, MO); 1,3-diaminopropane (E1; Sigma Aldrich); 1,3-diaminopentane (E3; TCI America, Portland, OR); 2-methyl-1,5-diaminopentane (E4; TCI America); 2-(3-aminopropylamino)ethanol (E6; Sigma Aldrich); 1-(3-aminopropyl)-4-methylpiperazine (E7; Alfa Aesar); 1-(3-aminopropyl)pyrrolidine (E8; TCI America); and cystamine dihydrochloride (E10; Alfa Aesar). siGFP with 5'-CAAGCUGACCCUGAAGUUCTT (sense) and 3'-GAACUUCAGGGUCAGCUUGCC (antisense) (Silencer ® positive control) and a scrambled siRNA sequence (scrRNA) with 5'-AGUACUGCUUACGAUACGGTT (sense) and 3'-CCGUAUCGUAAGCAGUACUTT (antisense) (Silencer ® negative control #1) were designed by and purchased from Ambion, Inc., (Carlsbad, CA). For viral transduction, lentivirus containing pPPT-eGFP plasmid was received from Dr. David Yue (Johns Hopkins University). Lipofectamine™ 2000 and Opti-MEM I were from Invitrogen (Carlsbad, CA) and used according to manufacturer instructions. For gel electrophoresis, UltraPure™ agarose was purchased from Invitrogen. All other materials used were reagent grade.

*4.3.2. eGFP-lentiviral transduction of MSCs*

Lentivirus containing pPPT-eGFP plasmids (cytomegalovirus promoter) were diluted in serum-free medium (Dulbecco's Modified Eagle Medium (DMEM; Invitrogen) with high glucose supplemented with 100 U/mL penicillin and 100 µg/mL streptomycin (Cellgro, Manassas, VA)) and added to passage 1 MSCs (Lonza (formerly Cambrex), Walkersville, MD) at 10% confluency. Complete expansion medium (the above mixture supplemented with 10% v/v fetal bovine serum (FBS; Atlanta Biologicals, Flowery Branch, GA)) was added 4 h after transduction to dilute viral titer, and medium was replaced with fresh medium complete medium after 48 h. Fluorescence microscopy and flow cytometry were used to confirm the overexpression of eGFP; we obtained an efficiency of >99% (**Figure 4.2**).

*4.3.3. MSC pre-differentiation and pre-transfection expansion*

MSCs were grown at 37 °C, 5% $CO_2$, and 21% $O_2$. All differentiation studies were done at passage 5. MSCs were expanded in monolayer at passage 4 with high glucose DMEM, 10% v/v FBS, 100 U/mL penicillin and 100 µg/mL streptomycin, and 1 ng/mL basic fibroblast growth factor 2 (bFGF-2; PeproTech, Rocky Hill, NJ). At 80% confluency, cells were released from monolayer via trypsin and placed under differentiation conditions.

*4.3.4. MSC adipogenic differentiation*

Previously expanded MSCs were plated at a density of 10000 /cm$^2$ and cultured for 4 weeks with high glucose DMEM, 10% v/v FBS, 100 U/mL penicillin and 100 µg/mL streptomycin, 5 µg/mL recombinant human insulin (Invitrogen), 1 µM dexamethasone (Sigma Aldrich), 200 µM indomethacin (Sigma Aldrich), and 500 µM 3-isobutyl-1-methylxanthine (IBMX; Sigma Aldrich) [31]. Cultures were assayed for adipogenesis by staining lipid droplets with Oil Red O (Sigma Aldrich).

*4.3.5. MSC osteogenic differentiation*

Previously expanded MSCs were plated at a density of 5000 /cm$^2$ and cultured for 4 weeks with low glucose DMEM, 10% v/v FBS, 100 U/mL penicillin and 100 µg/mL streptomycin, 10 mM β-glycerophosphate (Sigma Aldrich), 100 nM dexamethasone (Sigma Aldrich), and 50 µM ascorbic acid (Sigma Aldrich) [30]. Cultures were assayed for osteogenesis by staining protein-associated calcification with Alizarin Red S (Sigma Aldrich).

*4.3.6. Polymer synthesis*

Polymers were synthesized using previously reported protocols and are referred to following the reported nomenclature, with a polymer's name referring directly to its constituent monomers [130, 138, 139]. The number following the "B" title refers to the number of carbons between acrylate groups in the backbone monomer and the number following the "S" title refers to the number of carbons between the amine group and the alcohol group in the sidechain. One backbone diacrylate monomer (B3, B4, B5, or B6)

was mixed with one sidechain monomer (S3, S4, S5, or S6) at a 1.2:1 molar ratio of B:S. The reaction was carried out with stirring for 24 h at 90 °C to allow formation of the base polymer (B-S). The resulting base polymer was dissolved in dimethyl sulfoxide (DMSO) at 167 mg/mL. 480 µL of B-S in DMSO was mixed with 320 µL of a 0.5 M solution of one end-capping monomer (E1, E3, E4, E6, E7, E8, or E10) and vortexed for 1 h at room temperature. For E10-capped polymers, the resulting B-S-E polymer was incubated at room temperature for 1 day to ensure completion of the reaction before storage at –20 °C. All other polymers were immediately stored at –20 °C after end-capping. For the remainder of this report, polymers will be referred to by their composition (e.g. B4-S3-E10 or 4310).

All synthesized polymers used in this study were dissolved in BHT-stabilized tetrahydrofuran with 5% DMSO and 1% piperidine, filtered through a 0.2-µm filter, and measured with gel permeation chromatography (GPC; Waters, Milford, MA) to determine molecular weight. Representative polymers were diluted with deuterated DMSO and also analyzed by nuclear magnetic resonance (400 MHz, Bruker, Billerica, MA) using TopSpin 2 software (Bruker) for spectrum acquisition and ACD/NMR Processor (Advanced Chemistry Development, Inc., Toronto, Ontario, Canada) to verify the completion of both steps of the reaction.

*4.3.7. Nanoparticle characterization: nanoparticle tracking analysis (NTA)*

siRNA was diluted to 10 µg/mL in 25 mM sodium acetate buffer (pH 5). Polymer was diluted in the same sodium acetate buffer and added to the siRNA solution in a 1:1 volume ratio, for a final polymer-to-siRNA weight ratio (w/w) of 100-200 (500-200

μg/mL final polymer concentration). This solution was mixed by pipetting and then incubated at room temperature for 1 min to allow self-assembly to occur. The resulting nanoparticle suspension was diluted 1:100 in phosphate-buffered saline (PBS), then measured using a NanoSight NS500 (NanoSight Ltd., United Kingdom( and analyzed with NanoSight NTA 2.2 software as previously described [140]. Reported values for size are number-weighted hydrodynamic diameters of the particles.

*4.3.8. Polymer-siRNA binding assay: gel electrophoresis*

Gel retardation assays were carried out by adding polymer of varying concentrations in sodium acetate buffer to a constant concentration of siRNA in sodium acetate, as with normal particle preparation protocols (above). After 10 min of incubation, a solution of 30% v/v glycerol in water was added at a 1:5 v/v ratio as a loading buffer. Dyes were not added to the loading buffer, as they were found to interfere with binding. Samples were loaded into a 1% agarose gel with 1 μg/mL ethidium bromide at 125 ng siRNA per well. Samples were run for 15 min under 100 V, then visualized using UV exposure. Lack of a visible band at the location corresponding to siRNA alone (0 w/w polymer) was considered complete complexation of the nucleic acid by polymer.

To test the effect of a reducing agent, after 10 min of complexation, PBS buffer alone or PBS with L-glutathione (GSH) was added to each tube of particles, with a final GSH concentration of 5 mM to match approximate intracellular concentration of 1-10 mM [141]. Samples were immediately loaded into a 1% agarose gel and run for 15 min under 100 V before visualization under UV.

*4.3.9. Transfection of MSCs with siRNA against eGFP*

$GFP^+$ MSCs were seeded in clear-bottom, opaque-sided 96-well-plates at a density of 10000 /$cm^2$ and allowed to adhere overnight. All experiments were carried out on passage 3-6 MSCs. Before transfection, the GFP signal from each well was measured using a fluorescence multiplate reader (Synergy 2, Biotek, VT). Background signal was subtracted using $GFP^-$ MSCs seeded alongside the $GFP^+$ cells in complete expansion medium as described above. siGFP was diluted in 25 mM sodium acetate buffer (pH 5).

Polymer was diluted in sodium acetate and added to the siRNA solution at 1:1 volume ratio, for a final polymer-to-siRNA weight ratio of 100-200 w/w. This solution was mixed by pipetting and then incubated at room temperature for 10 min to allow self-assembly to occur. The resulting nanoparticles were added to cells in complete expansion medium for a final siRNA dose of 60 nM (0.9 μg/mL) and final polymer dose of 90-180 μg/mL. Studies were done in triplicate. Cells were incubated with the particles for 2 h before the media was changed and replaced with fresh, complete medium. For each polymer tested, one group was treated with siGFP and another with scrRNA complexed with the same polymer as a paired control. A replicate set of wells was prepared for each group for viability measurements.

After 24 h, viability was measured using an MTS assay (CellTiter Aqueous One, Promega, Madison, WI) according to the manufacturer's instructions. On the remaining plates, medium was changed every 3-4 days and fluorescence measurements were taken daily. At each timepoint, knockdown was calculated by subtracting background signal, then calculating the ratio of signal in the siGFP group to that in the scrRNA group and

subtracting this ratio from 1. For particles with the highest activity, cells were trypsinized after 12 days, resuspended in PBS with 2% FBS, and analyzed by flow cytometry (Accuri C6, Accuri Cytometers, MI) to confirm readings taken using the plate reader. The media of the FL1 signal (emission 530/30 nm) was calculated for each group of cells using FlowJo 7 (Treestar Inc., Ashland, OR). Background fluorescence, or the median of $GFP^-$ cells, was subtracted from all values, and the ratio of signal from scrRNA- and siGFP-treated cells was calculated as above to determine knockdown.

*4.3.10. Transfection of MSCs with siRNA against BCL2L2*

Passage 3 untransduced MSCs were seeded in 12-well-plates at a density of 10000 /$cm^2$ in complete expansion medium and allowed to adhere overnight. Transfection was carried out as described above, with the top polymer from the siGFP screenings used at a 150 w/w ratio to complex with siRNA against BCL2L2 (siBCL2L2). A control with polymer at 150 w/w and scrRNA was also prepared. After 10 min of incubation for nanoparticle self-assembly, the resulting nanoparticles were added to cells incomplete expansion medium for a final siRNA dose of 60 nM in each well and allowed to incubate at 37 °C for 4 h. The media and nanoparticles were then removed and replaced with osteogenic medium. We also included one group of cells that were not transfected but were cultured under osteogenic conditions and another group of cells cultured under growth conditions as negative controls. The medium was replaced every 3-4 days and the cells were analyzed after 4 weeks by Alizarin Red S staining, calcium assay (Calcium LiquiColor Kit, Stanbio, Boerne, TX), and DNA assay (Quant-iT PicoGreen dsDNA Assay Kit, Invitrogen) to ensure the results of the calcium assay were

not due to differences in cell number between groups. Wells were transfected at $n = 9$, with $n = 3$ for each of the analyses.

*4.3.11. Statistics*

Unless otherwise stated, all results are presented as mean ± standard error of the mean. Statistical significance compared to the controls was assessed with a one-way ANOVA with post-hoc Dunnett test, with $p<0.05$ considered significant.

## 4.4. Results and discussion: development of an siRNA delivery vehicle

*4.4.1. MSC multilineage differentiation*

Both GFP-transduced and untransduced MSCs were subjected to osteogenic and adipogenic conditions for 4 weeks. Osteogenic and adipogenic groups were then stained with Alizarin Red S and Oil Red O, respectively. Transduced MSCs retained the ability to differentiate down both osteogenic and adipogenic lineages at levels comparable to that of untransduced MSCs (**Figure 4.3**). Hence, $GFP^+$ MSCs were deemed a valid model to assess the characteristics of non-viral transfection of MSCs over the course of this experiment.

*4.4.2. Polymer synthesis*

The number-averaged (Mn) and weight-averaged (Mw) molecular weights of all synthesized polymers are summarized in **Table 4.1**. The numbers of subunits per polymer chain was calculated using the Mn, with an average of 14-15 subunits. NMR analysis clearly showed the presence of acrylate peaks in the base polymer, which are no longer

detectable after 1 h end-capping reaction at room temperature (**Figure 4.4**). The reaction of E10 with the base polymer did not go to completion after only 1 h, so further incubation at room temperature was required. This additional incubation time could lead to a side reaction (amide formation due to nucleophilic attack by the free end-capping amine on the base polymer's ester linkages), indicated by any additional peaks in the product around 3-3.5 ppm [139]. Since this amide peak was not apparent in the spectrum, our product was not contaminated by this side product.

*4.4.3. Nanoparticle tracking analysis*

Using NTA, individual nanoparticles suspended in a buffer of physiological salinity and pH were measured to calculate number-weighted average size and concentration (**Figure 4.5**). As has been reported in previous studies [130, 131, 140], most nucleic acid particles formed with PBAEs are between 80 and 150 nm in diameter, a size range found to be amenable for cellular uptake [140]. By using NTA rather than dynamic light scattering (DLS), we were able to measure individual particles, including number-weighted size distributions and absolute particle concentration [142]. Increased polymer content tended to increase the number of particles formed with the same amount of siRNA, indicating that complexation of siRNA into nanoparticles was more efficient with more polymer. Interestingly, 4310-based particles tend to be larger in size compared to 437- and 433-based particles; these also showed significant differences in transfection efficiency (see below). We therefore concluded that the representative end-modified PBAEs measured by NTA (453, 447, 4410, 433, 437, and 4310) are good candidate materials for packaging siRNA.

*4.4.4. siGFP transfection*

We evaluated degradable polymers to choose an optimal polymer for siRNA delivery to MSCs, assaying delivery efficacy by looking at GFP knockdown over time (**Figure 4.6**). Based on previous results in another cell type [131], we included many cystamine (E10) terminated polymers in our study, along with polymers that have previously been seen to be effective in DNA delivery [129, 132, 143, 144]. Although RNAi has been found to be an important potential tool in directing stem cell differentiation and MSCs are one of the most commonly studied cell types in differentiation studies [145], MSCs have generally been found to be much harder to transfect than are other cells, such as human umbilical vein endothelial cells (HUVECs). This trend has been seen in DNA delivery studies [132], especially when the transfection is performed in the presence of serum proteins, as we have done here (10% v/v serum).

Through our polymer library approach, we were able to discover several polymers that caused effective knockdown. This research reveals several trends; many types of PBAEs induced knockdown, but only a few were significantly better than the leading commercially available controls (**Figure 4.6**). Interestingly, the subset of E10-terminated polymers examined here tended to cause relatively high knockdown compared to non-E10- or cystamine-terminated polymers. A major exception to this trend is 447 at high w/w ratios, which has been previously identified as one of the top-performing PBAEs and which can be used for nucleic acid delivery to HUVECs [131]. The other exception is 546, which, while very effective at high w/w, was also very toxic. The top E10 polymers, on the other hand, tended to be less toxic and were also effective at lower w/w. Certain

base polymers, like B4-S3, showed little or no delivery efficacy with most end-capping amines, but were particularly effective when end-capped with E10, suggesting that the cystamine moiety itself may play an important role in siRNA delivery.

In particular, polymer 4310 formed successful nanoparticles, able to knock GFP levels down by 74% ± 6% at 200 w/w and 72% ± 5% at 150 w/w according to flow cytometry 12 days after transfection (**Figure 4.7**). Both of these were significantly superior to Lipofectamine™ 2000 ($p<0.01$). It should be noted that the flow cytometry data shown here are expected to be a slight underestimate. As seen in **Figure 4.2**, the $GFP^+$ MSCs used were so brightly fluorescent that they were at the upper limit of sensitivity for the flow cytometer, even when using a 90% attenuation filter; therefore, small levels of GFP fluorescence knockdown in the brightest population of $GFP^+$ cells could be underreported.

We examined the influence of cystamine further by directly comparing 4310 with 433 and 437 to test our hypothesis that the cystamine end-cap was the reason for 4310's efficacy. We also compared transfection with Lipofectamine™ 2000 and with naked siRNA as a baseline control (**Figure 4.8**). 4310 outperformed Lipofectamine™ 2000, 433, and 437 in both magnitude and duration of knockdown, achieving knockdown of ~91% at 20 days pot-transfection compared to ~50% using Lipofectamine™ 2000. This is in contrast to other work in siRNA-mediated knockdown using other delivery methods, including naked siRNA and lipid-based vehicles, in which knockdown duration was reported as 15 days or less [146-149]. Even after 20 days, 4310-mediated siRNA knockdown was only beginning to decline. Based on knockdown data from flow

cytometry and the plate reader, 4310 at 150 w/w, which was not significantly different from 200 w/w, was used for later differentiation studies.

*4.4.5. E10 (cystamine)-mediated siRNA release*

The base polymer B4-S3 shows great difference in siRNA binding ability depending on its end-capping amine group (**Figure 4.9**). 4310 is able to bind more tightly than is 433 at lower weight ratios upon initial complexation, which may explain why it is effective at lower w/w compared to other PBAEs in our study. The addition of reducing agent GSH, however, has no apparent effect on 433-siRNA complexes, while 4310-siRNA complexes show complete release immediately after addition of GSH. Because intracellular GSH concentration is approximately three orders of magnitude higher than extracellular GSH concentration is [150], this polymer's sensitivity to GSH could prove very useful for quick and efficient environmentally-triggered intracellular siRNA delivery once the polymeric nanoparticles enter the cytoplasm.

It is known that PBAEs are able to facilitate high cellular uptake (due to their net positive charge) as well as endosomal escape via the proton sponge mechanism because of titratable tertiary amines in the polymer backbone [151]. Just as insufficient release of DNA plasmids can have an inhibitory effect on their transcription and function [152, 153], we also expect that efficient release is important for optimal delivery of siRNA. As such, polymers like 4310 and other E10-terminated polymers may serve the dual purpose of strengthening the initial binding interaction between polymer and siRNA due to the presence of additional terminal primary amines as well as facilitating triggered release in

the cytoplasm after cellular uptake due to the presence of disulfide linkages adjacent to these terminal primary amines.

*4.4.6. siBCL2L2 transfection and its effect on osteogenesis*

To ensure that the knockdown of GFP as a reporter would translate to successful knockdown when using functional genes, we tested our delivery system on MSC osteogenic differentiation. siBCL2L2 was delivered to MSCs and, after 4 weeks of cultivation under osteogenic conditions, osteogenesis was evaluated. Alizarin Red S staining (**Figure 4.10**, **A-D**) revealed that cells transfected with siBCL2L2 stained more intensely than did both cells transfected with scrRNA and untreated cells, demonstrating increased osteogenic differentiation. As expected, cells cultured under standard growth conditions, rather than differentiation conditions, did not stain under Alizarin Red S. We also assayed the calcium content in each group to evaluate osteogenesis further to discover that the Alizarin Red S findings correlated with quantitative analysis of calcium content. Cells transfected with siBCL2L2 showed statistically higher calcium relative to all other groups (**Figure 4.10**, **E**). These results were not due to differences in cell number, as indicated by the results of the DNA assay, which revealed no significant differences in cell number between groups (**Figure 4.10**, **F**).

Our results indicate that 4310-mediated knockdown of BCL2L2 is capable of inducing a functional outcome in MSCs, enhancing osteogenesis over the course of 4 weeks. This study demonstrates a proof-of-principle using our environmentally-triggered bioreducible nanoparticle siRNA-delivery system. Critically, we have shown that cystamine-terminated poly(β-amino ester)s are effective for siRNA delivery to MSCs,

especially when used at a high weight ratio of polymer to siRNA. This result is supported by studies in the literature that report the use of reducible polymers for siRNA delivery, albeit in the absence of serum [154] or at a higher dosage and with lower efficacy [155, 156]. Here, we were not only able to deliver siRNA-loaded nanoparticles in medium with 10% serum and induce high knockdown (>70%), but also isolate the effects of the cystamine end-group from other effects due to the rest of the polymer. That the polymer's terminal group has such a dominant effect on the properties of PBAEs, which are linear polymers with 10-20 subunits along the base polymer chain, is unexpected but emphasizes the importance of small changes to the molecular structure of PBAEs, a feature that our library-based approach is well-suited to address.

In conclusion for the first part of the chapter, a polymer screen of PBAEs resulted in the finding that bioreducible polymer vehicles, such as 4310, efficiently deliver siRNA to MSCs, resulting in knockdown that can have an effect on stem cell differentiation. With this finding, the investigation into PDGF-BB follows.

## 4.5. Materials and methods: effect of PDGF-BB on osteogenesis

### *4.5.1. Isolation and source of cells*

A tissues obtained for this study were obtained under Institutional Review Board approved protocols with patient consent. To ensure the observed phenomena are cell-type specific rather than donor-dependent, the initial characterization study was performed using three donors for MSCs, denoted M1, M2, and M3; and three donors for ASCs, denoted A1, A2, and A3. Donor M1 (late 20s, male) was commercially obtained from Lonza (Basel, Switzerland), while donors M2 (32-year-old male) and M3 (27-year-old

male) were isolated at Case Western Reserve University following established marrow isolation procedures [88, 157, 158]. Briefly, aspirated iliac crest bone marrow was mixed with culture medium and centrifuged to remove adipocytes. MSCs were isolated from the resulting cell pellet via centrifugation in a Percoll gradient and the MSC-enriched fraction was plated. Donors A1 (54-year-old female) and A2 (50-year-old female) were isolated from lipoaspirate using established protocols [92, 93] at Johns Hopkins Medical Institutions, while donor A3 (47-year-old female) was isolated at Tulane University School of Medicine. Briefly, harvested lipoaspirate tissue was digested in 1 mg/mL collagenase type I (Worthington Biochemical Corporation, Lakewood, NJ) for 1 hour at 37 °C. The released cells were then centrifuged to obtain the stromal vascular fraction pellet; the pellet was then resuspended and plated to obtain passage 0 ASCs. Cells from all six donors were characterized via flow cytometry for surface expression of CD31, CD34, CD73, CD90, and PDGFRβ as previously described [93]. In this study, PDGFRβ was studied specifically as it preferentially binds PDGF-BB.

*4.5.2. Culture conditions*

For all experiments, cells were expanded for use at passage 2. Expansion medium consisted of Dulbecco's Modified Eagle Medium (DMEM) with 4.5 g/L glucose (Life Technologies, Frederick, MD) supplemented with 10% v/v fetal bovine serum (FBS; Atlanta Biologicals, Flowery Branch, GA), 100 U/mL penicillin and 100 µg/mL streptomycin (Cellgro, Manassas, VA), and 1 ng/mL basic fibroblast growth factor (PeproTech, Rocky Hill, NJ). Subsequent to expansion, cells were cultured in one of four conditions: namely, the control (-), control (+), osteogenic (-), and osteogenic (+)

conditions. The control (-) medium consisted of DMEM with 1 g/L glucose, 100 U/mL penicillin and 100 µg/mL streptomycin, and 6% v/v FBS. Control (+) medium consisted of control (-) medium with the addition of 20 ng/mL recombinant human PDGF-BB (PeproTech), a concentration determined based on the work outlined in Chapter 2, section 2.5.2 [73]. The osteogenic (-) medium consisted of control (-) medium with 10 mM β-glycerophosphate (Sigma Aldrich, St. Louis, MO) and 50 µM ascorbic acid (Sigma Aldrich). Finally, osteogenic (+) medium consisted of osteogenic (-) medium with 20 ng/mL PDGF-BB. For all conditions, PDGF-BB was replenished twice a week. Unless otherwise noted, all osteogenic cultured were carried out for 3 weeks.

*4.5.3. Characterization of mineralization response to PDGF-BB*

MSCs and ASCs were cultured under control (-), control (+), osteogenic (-), and osteogenic (+) conditions for 3 weeks and then subjected to Alizarin Red S (Sigma Aldrich) or von Kossa (silver nitrate and sodium thiosulfate both from Sigma Aldrich) staining for qualitative assessments. Quantitatively, samples were subject to the Quant-iT PicoGreen dsDNA assay (Invitrogen, Carlsbad, CA) and the Stanbio LiquiColor calcium assay (Stanbio, Boerne, TX) to determine calcium content normalized to cell number. DNA content was converted to cell number using 6.24 pg/MSC and 7.23 pg/ASC, determined by performing the DNA assay on known numbers of the cells specifically used in this study (data not shown).

*4.5.4. Real-time polymerase chain reaction*

To investigate the genetic expression of MSCs and ASCs under the four conditions, RT-PCR was performed at 1, 2, and 3 weeks of culture for β-actin (BA), Runx2, osteocalcin (OCN), osteonectin (OSN), and collagen I (Col-I). Cells were digested using TRIzol reagent (Life Technologies) and the mRNA isolated with chloroform washes. The mRNA was further purified and concentrated using isopropanol and ethanol washes and used to produce cDNA using the iScript cDNA Synthesis Kit (Bio-Rad Laboratories, Hercules, CA). cDNA was then subject to RT-PCR using custom-designed primers (**Table 4.2**). For all analysis, the delta-delta Ct method was used in which the housekeeping gene (BA) and the appropriate (-) group were subtracted from all other Ct readings.

*4.5.5. Monomer and polymer synthesis*

Using the principle that bioreducible structures can effectively deliver siRNA as outlined in the first part of this chapter, bioreducible monomers and polymers were developed and synthesized for the current study. Bioreducible monomer 2,2'-disulfanediylbis(ethane-2,1-diyl) (BR6) was synthesized as previously described [159, 160]. Briefly, bis(2-hydroxyethyl) disulfide (10 mmol) was acrylated with acryloyl chloride (300 mmol) in the presence of trimethylamine (TEA; 300 mmol) in anhydrous tetrahydrofuran (THF) for 24 hours. TEA HCl precipitate was removed via filtration, and THF was removed via rotary evaporation. The product was further purified by dissolving it in dichloromethane (DCM) and washing five times with a 0.2 M solution of $Na_2CO_3$ and three times with water. The organic phase was dried with $Na_2SO_4$ and DCM was

removed via rotary evaporation. BR6 structure and purity were verified by $^{1}$H NMR [159].

Bioreducible PBAEs were synthesized in a method similar to Kozielski et al. [159]. Base monomer BR6 was polymerized with side chain monomer 4-amino-1-butanol (S4) at a ratio of 1.05:1 at 500 mg/mL in anhydrous THF at 60 °C for 24 hours while stirring. Polymers were end-capped at a concentration of 100 mg/mL in THF with 2-(3-(aminopropyl)amino)methanol (E6) at 0.2 M for 1 hour at room temperature while stirring. Polymers were precipitated in diethyl ether to remove uncreated monomer and THF. The precipitate was recovered by centrifugation and solvent decanting. The polymer was washed and isolated a second time, and residual ether was removed under vacuum for 48 hours. The resulting polymer BR6-S4-E6 was stored in dimethyl sulfoxide at 100 mg/mL at –20 °C.

*4.5.6. Knockdown of PDGFRβ*

siRNA against PDGFRβ (siPDGFRβ) was delivered to both MSCs and ASCs as follows. Nanoparticles were formed by dissolving siRNA and polymer separately in 25 mM sodium acetate, mixing the siRNA and polymer solutions, and allowing nanoparticles to self-assemble for 1 minutes. The cell culture medium was removed and replaced with serum-free medium, then nanoparticle solutions were added directly to the cell culture media. Polymer was used at a final concentration of 180 μg/mL and siRNA concentration at 40 nM. Following a 2-hour incubation with cells, the nanoparticle-containing media were removed and replaced with fresh, complete cell culture medium.

At 1, 2, and 3 weeks, knockdown of PDGFRβ was quantified using both RT-PCR and flow cytometry via an antibody against the receptor (Santa Cruz, Santa Cruz, CA). Separately, siPDGFRβ was delivered to MSCs and ASCs and cells were cultured under control (-), osteogenic (-), and osteogenic (+) conditions for 3 weeks. After the culture period, calcium and DNA content were quantified as outlined above.

*4.5.7. Murine critically sized calvarial defect model*

For the final portion of the study, two different cell groups were created by lentiviral transduction: (a) ASCs transduced with PDGFB (DNASU plasmid HsCD00437330 [161]) and (b) ASCs transduced with the fluorescent protein mCherry (plasmid kindly provided by Don Zack's laboratory). Lentiviral production was produced using 293T cells and the ViraSafe Lentiviral Packaging System (Cell Biolabs, San Diego, CA). ASCs were seeded at 6000 /cm$^2$, allowed to adhere overnight, and given virus at $8 \times 10^7$ viral particles per milliliter for 4 hours (an approximate multiplicity of infection of 80) under serum-free conditions. Expansion medium was added after the viral incubation step and transduction was allowed to continue for 72 more hours, after which medium was changed to clean expansion medium and the cells were allowed to proliferate to confluence. PDGFB-transduced ASCs were verified by RT-PCR and enzyme-linked immunosorbent assay (ELISA, PeproTech). In addition, cells were cultured under control (-) and osteogenic (-) conditions for 3 weeks and the subject to DNA and calcium assays as outlined above to determine whether the overexpressed PDGF-BB was having a mitogenic and mineralization effect.

For the in vivo study, ASCs were encapsulated at $2 \times 10^7$ /mL in fibrin gels containing final concentrations of 8 mg/mL fibrinogen and 2 U/mL thrombin. Cells in fibrin were seeded into porous PCL scaffolds (diameter: 4 mm, height: 644 μm, porosity 60%) mixed with DCB particles printed with our custom 3D printer as outlined in Chapter 3. The scaffold geometry was chosen to match the geometry of the murine calvarial defect described below. In addition, a third group was produced with the same scaffolds and fibrin, but containing no cells. For seeding, cells were suspended in fibrinogen and thrombin was added at the proper ratio. Prior to gelation, the mixture was pipetted into the pore spaces of the scaffold and subsequent gelation held the cells in place within the pore spaces.

Eight 8-week-old male FOXN1-knockout mice (Jackson Laboratories, Bar Harbor, ME) were operated on, resulting in 16 sites with $n = 4$ for ASCs overexpressing PDGFB, $n = 4$ for ASCs transduced with mCherry, $n = 4$ for acellular controls, and $n = 4$ unoperated controls. In all cases, IACUC-approved procedures were followed. For creation of the defect, previously established methods were adapted [94, 95]. Briefly, a 4-mm circular knife (Medicon, Tuttlingen, Germany) was used to excise 4-mm pieces of calvaria, with special care made to avoid damaging the underlying dura mater. The location of the defect was kept consistent from animal to animal by placement between the coronal and lambdoid sutures and approximately 1 mm lateral to the sagittal suture.

Mice were imaged using computed tomography (CT) at 8 weeks post-implantation, sacrificed, and calvariae were excised for histological analysis. Imaging was performed on a Gamma Medica X-SPECT small animal system (Gamma Medica, Salem, NH) with 80 kV peak voltage and 600 μA current. Reconstruction was performed

with voxel size 100 μm and threshold 15300/65535. For sectioning, samples were fixed in 3.7% formalin overnight and fixed samples were infiltrated with 30% sucrose, frozen in Tissue Tek OCT medium, and cut into 10 μm thick sections. Cryosections were mounted and dried on Superfrost Plus slides, followed by rehydration in water before staining with von Kossa/van Gieson, haematoxylin/eosin (H&E; Sigma Aldrich), or immunohistochemistry. Immunohistochemistry was performed by blocking for 30 minutes (10% normal serum/0.2% Triton X), followed by overnight incubation with primary antibody (0.5 μg/mL mouse anti-human Lamin A/C; Abcam, Cambridge, Britain) at 4 °C, 1 hours incubation with Cy3-conjugated donkey anti-mouse (Jackson ImmunoResearch, West Grove, PA) at room temperature, and nuclear counterstain with 4'-6-diamidino-2-phenylindole (DAPI; Sigma Aldrich). Cryosections were imaged using an inverted Zeiss Axio Observer microscope.

#### *4.5.8. Statistics*

Unless otherwise noted, statistical comparisons used the two-tailed Student's t-test at α level 0.05.

### 4.6. Results: effect of PDGF-BB on osteogenesis

#### *4.6.1. Cell characterization*

Surface marker characterization marched well-documented profiles for MSCs/ASCs: all cells were negative for CD31, the MSCs negative for CD34, the ASCs weakly positive for CD34, and all cells were positive for both CD73 and CD90 (**Figure 4.11**).

*4.6.2. Osteogenic response of MSCs and ASCs to PDGF-BB*

After 3 weeks of culture, MSCs and ASCs were stained with Alizarin Red S and von Kossa for a qualitative assessment of mineralization. MSCs and ASCs stained negatively under both control (-) and control (+) conditions (**Figure 4.12**, **A**-**H**), as no calcium phosphate source was present in these conditions. Under osteogenic (-) conditions, both cell types stained positively for mineralization (**Figure 4.12**, **I**-**L**); the ASC group stained more intensely positive under osteogenic (+) conditions (**Figure 4.12**, **O**-**P**). MSCs under osteogenic (+) conditions stained with similar intensity to MSCs under osteogenic (-) conditions (**Figure 4.12**, **M**-**N**). Because PDGF-BB is a mitogen, we considered the possibility that the more intense staining with ASCs was simply due to the presence of more cells. To address this, calcium content was quantified and normalized to cell counts. ASCs under osteogenic (+) conditions displayed significantly higher calcium per cell than did ASCs under osteogenic (-) conditions, an observation that did not hold for MSCs; there was no difference in calcium per cell between MSCs under osteogenic (-) conditions versus MSCs under osteogenic (+) conditions (**Figure 4.12**, **bottom**). In particular, this held for cells across all donors examined. Also of note, in all cases PDGF-BB acted as a mitogen, with osteogenic (+) groups displaying higher cell counts at the end of 3 weeks compared to cells under osteogenic (-) conditions; this held regardless of cell type and donor (**Figure 4.11**, **top**), confirming that the MSCs were able to respond to the PDGF-BB, just not in an osteogenic manner.

To determine whether there was a genetic mechanism underlying this data, RT-PCR was performed at 1, 2, and 3 weeks of culture. Cells cultured under control (+)

conditions, despite being unable to form mineral, displayed a genetic response: MSCs generally downregulated osteogenic genes compared to MSCs under control (-) conditions, whereas ASCs generally upregulated those genes (**Figure 4.13**, **left**). With the addition of osteogenic factors, the same trend held, with ASC expression of the same genes upregulated under osteogenic (+) conditions compared to expression levels under osteogenic (-) conditions and the opposite true for MSCs (**Figure 4.13**, **right**).

*4.6.3. Loss-of-function*

R646 knocked down PDGFRβ well, achieving a peak knockdown approaching 100% at 1 week post-transfection and declining afterward to ~30% at 3 weeks post-transfection (**Figure 4.14**, **top**). After 3 weeks of culture under control (-), osteogenic (-), and osteogenic (+) conditions (the control (+) group was omitted in this experiment since no mineralization occurred in the absence of osteogenic medium ), cells were subjected to calcium per cell quantification to determine the effect of knocking down the receptor. MSCs produced similar levels of calcium per cell irrespective of the presence of PDGF-BB or whether cells were treated with siRNA, reinforcing the notion that PDGF-BB did not directly affect MSC mineralization (**Figure 4.14**, **bottom**). In contrast, while the silenced ASCs show no statistically significant difference between osteogenic (-) and osteogenic (+) groups, untreated ASCs and ASCs given scrRNA retained a statistically higher calcium per cell reading in the osteogenic (+) groups as compared to the osteogenic (-) groups via a two=way ANOVA with $p<0.05$ (**Figure 4.14**, **bottom**) despite the knockdown being less pronounced in ASCs at the mRNA level at later time points.

This loss-of-function data further supports the observations that ASCs upregulate calcium production on a per-cell basis when signaled with PDGF-BB, whereas MSCs do not.

### *4.6.4. Transduction of PDGFB into ASCs*

Both RT-PCR and PDGF-BB ELISA confirmed the efficacy of transduction, with the PDGFB mRNA and protein greatly upregulated compared to cells transduced with mCherry by 2 weeks post-transduction (**Figure 4.15**, **top**). PDGFB-transduced cells also proliferated more under osteogenic conditions (**Figure 4.15**, **bottom left**) and produced more calcium per cell (**Figure 4.15**, **bottom right**) compared to mCherry-transduced cells, indicating the overexpressed PDGFB gene was having a functional effect on ASCs. PDGFB-transduced MSCs displayed similar increases in proliferation (**Figure 4.16**, **bottom left**), but the transduction did not have an effect on MSC calcium per cell (**Figure 4.16**, **bottom right**).

Transduced cells were encapsulated into fibrin gels and seeded into custom-printed scaffolds and implanted for 8 weeks within the murine calvarial defect. CT imaging of murine calvariae at 8 weeks post-implantation (**Figure 4.17**, **A**-**B**) showed a significantly higher volume of regenerated bone within the PDGFB-transduced groups compared to both other groups via one-way ANOVA both when considering absolute bone volume (**Figure 4.17**, **C**) or when normalizing bone volume to unoperated contralateral controls (**Figure 4.17**, **D**). In particular, the higher mineral content was observed throughout the scaffolds (both outer and inner regions), strongly suggesting that transplanted ASCs themselves were being signaled by the elevated PDGF-BB concentrations to undergo osteogenesis.

To investigate this further, we tested whether human ASCs remained at the defect site. Excised scaffolds were sectioned and stained with human-specific Lamin A/C with DAPI counterstain for retention of human cells (**Figure 4.18**, **left**), H&E for general scaffold cellularity and tissue formation (**Figure 4.18**, **middle**), and von Kossa/van Gieson for bone formation (**Figure 4.18**, **right**). All scaffolds were populated with cells and matrix as evidenced by DAPI and H&E stains. While a small amount of von Kossa staining occurred in the mCherry-transduced group with some surrounding osteoid, there was much more mineralized tissue in the PDGFB-transduced group. Of particular note, positive human-specific staining was apparent in both mCherry-transduced and PDGFB-transduced groups, indicating the human cells were still present 8 weeks post-implantation and were potentially contributing to the tissue formation within the scaffold. As a control, the acellular scaffolds, while showing DAPI staining, had no human-specific staining, indicating the resident cells were of murine origin.

## 4.7. Discussion: effect of PDGF-BB on osteogenesis

In this study, MSCs and ASCs were compared directly in their osteogenic response to PDGF-BB. The findings reported in this study simultaneously confirm previous research showing that PDGF-BB is not directly osteoinductive on MSCs [113-117] while also confirming more recent findings that PDGF-BB can directly enhance ASC osteogenesis [73, 93]. Both correlative (**Figure 4.12**) and loss-of-function (**Figure 4.14**) evidence support the observations that the divergent mineralization responses to PDGF-BB are marked. Since it has been previously shown [73] that dexamethasone is not essential for mineralization of ASCs, we omitted it from this study; however, due to

the prevalence of dexamethasone in MSC osteogenic culture, we also compared the mineralization response of MSCs and ASCs to PDGF-BB in the presence of 100 nM dexamethasone. While the addition of dexamethasone resulted in a two-fold increase of calcium per cell for MSCs and three-fold increase of calcium per cell for ASCs (**Figure 4.19**), the mineralization of MSCs was still unaffected by the addition of PDGF-BB, while it was enhanced in ASCs. In particular, a key finding in this study is the differential response between MSCs and ASCs when examining the gene expression of osteogenic genes Runx2, OCN, and OSN (**Figure 4.13**), indicating that the observed difference in mineralization arise from fundamental genetic differences in these two cell populations. Indeed, ASC expression of Runx2 and OCN was enhanced in the presence of PDGF-BB even in the absence of osteogenic factors, indicating that PDGF-BB itself is osteoinductive to ASCs but not to MSCs.

The impetus for hypothesizing a fundamental difference between MSCs and ASCs is not new and arises from subtleties observed in the literature. For example, the generally accepted surface marker profile for ASCs includes a weakly positive CD34 population [162, 163], while MSCs are traditionally reported to be negative for CD34 [31, 162], an observation supported by this study (**Figure 4.11**, **bottom**). In addition, ASCs possess more proliferative potential than do MSCs [164]. Most importantly, there have been several studies demonstrating a difference in potency between MSCs and ASCs, with some groups suggesting an increased capacity for osteogenic differentiation of MSCs [165, 166] and a penchant for adipogenic differentiation in ASCs [166, 167]. Despite these observations, other studies have shown that by changing culture conditions (e.g. by the addition or subtraction of growth factors), differentiation potential can be

modulated between the cell types [168], thus suggesting the innate biochemistries of MSCs and ASCs are different.

While differences in potency are not generally a subject of controversy, the mechanisms underlying these differences are still poorly understood. It has been shown that MSCs express a higher preponderance of genes associated with osteogenesis [165], while ASCs display higher expression of adipogenic genes [169]. The possibility of epigenetic mechanisms underlying differences in lineage-specific gene expression has been investigated, albeit not as extensively. For instance, osteo-specific genes such as osteoglycin and osteopontin have been shown to feature different levels of methylation in MSCs and ASCs [170, 171]. While delineating genetic and epigenetic mechanisms is outside the scope of this study, the finding that gene expression of Runx2, OCN, and OSN differed between MSCs and ASCs with respect to the presence of PDGF-BB may be well-supported in this context. Taken together, previous studies into MSC and ASC stem cell biology and lineage potency provide ample motivation for rigorously delineating differences in response to growth factors.

The original impetus for investigating the role of PDGF-BB specifically in bone repair arises from its native presence in the fracture site [111, 112] and the clinical observation that injection of PDGF-BB accelerates bone regeneration [74]. Given previous results with MSCs, confirmed by the results of this study, the idea that PDGF-BB in a fracture site enhances repair in an indirect fashion is well-supported. For instance, the role of PDGF-BB in recruiting vascular-stabilizing cells is well-studied: endothelial cells invading a region secrete PDGF-BB to attract pericytes that then wrap around the nascent vasculature, stabilizing the network [75, 76]. Given the observation

that bone forms around a vascular template [112, 172-174], the vascular stabilization of PDGF-BB in a fracture site may be a possible mechanism for indirect enhancement of bone repair. Such indirect mechanisms would be the sole mechanisms in a tissue engineering approach using MSCs in conjunction with PDGF-BB; however, a tissue engineering approach using ASCs instead may take advantage of a second mechanism – that the PDGF-BB may directly enhance the osteogenesis of implanted ASCs while retaining the establishes vascular-stabilizing properties. The potential for this additional mechanism underscores the importance of critically defining differences between cell populations such that a tissue engineered graft can take full advantage of both cellular and biomolecular components.

The clinical advantages of PDGF-BB itself are underscored when comparing to the current gold standard for growth factor-based bone regenerative therapies, BMP2. The drawback of BMP2 use, the requirement for supraphysiological doses, was discussed in Chapter 2, section 2.5.2. As shown before [73] and in the current study, a robust enhancement of ASC mineralization in response to PDGF-BB occurred at a concentration of 20 ng/mL, a concentration comparable to physiological levels within a fracture site [111, 175]. In particular, while ASCs cultured under osteogenic (-) conditions tended to produce less calcium per cell than did identically cultured MSCs, ASCs cultured under osteogenic (+) conditions not only produced more calcium per cell than did ASCs cultured under osteogenic (-) conditions, but also produced calcium levels at or above levels from MSCs cultured under osteogenic (-) conditions (**Figures 4.12** and **4.14**, **bottom**). This observation held across the six donors investigated in this study, indicating a donor-independent phenomenon. Taken together, these considerations suggest that the

use of PDGF-BB in clinical bone regenerative therapy in conjunction with ASCs may be an attractive option alongside more traditional approaches.

To illustrate the in vivo regenerative potential of tissue engineered constructs using both ASCs and PDGF-BB, the murine calvarial defect model showed a marked difference in implanted ASCs overexpressing PDGFB compared to implanted ASCs without PDGF-BB. CT quantification of newly mineralized tissue was evidently higher from ASCs with PDGF-BB (**Figure 4.17**) and positive von Kossa staining in the PDGFB-transduced groups confirmed this observation (**Figure 4.18**). We considered the possibility that the regenerated bone was solely due to invading murine cells; however, the presence of human-specific staining within both PDGFB-transduced and mCherry-transduced groups (**Figure 4.18**, **left**), the stark contrast of mineralized volume between the two, and the presence of mineralized tissue in the PDGFB-transduced scaffold center (**Figure 4.17**, **B** and **Figure 4.18**, **right**) suggests the implanted human cells directly contributed to increased bone regeneration. While there is previous data suggesting this [176], we have shown here that the contribution of implanted ASCs is greatly enhanced by the presence of PDGF-BB signaling. A more rigorous investigation on the exact contribution of implanted ASCs within an in vivo bone defect will be the subject of a future study.

# Tables: Chapter 4

| Polymer | Mn (Da) | Mw (Da) | PDI | # subunits per chain |
|---|---|---|---|---|
| B4-S3-E3 | 4295 | 6805 | 1.584 | 17 |
| B4-S3-E7 | 4288 | 6891 | 1.607 | 17 |
| B4-S4-E7 | 4940 | 10,176 | 2.060 | 18 |
| B4-S5-E3 | 4426 | 7459 | 1.685 | 15 |
| B4-S5-E4 | 4991 | 11,919 | 2.388 | 17 |
| B4-S5-E6 | 4840 | 8080 | 1.669 | 17 |
| B4-S5-E7 | 4262 | 7181 | 1.685 | 15 |
| B4-S5-E8 | 5464 | 12,365 | 2.263 | 19 |
| B5-S4-E4 | 4183 | 7637 | 1.826 | 14 |
| B5-S4-E6 | 4381 | 7912 | 1.806 | 15 |
| B6-S3-E3 | 4243 | 7090 | 1.671 | 15 |
| B6-S3-E6 | 4206 | 7806 | 1.856 | 15 |
| B3-S4-E10 | 3527 | 6599 | 1.871 | 14 |
| B3-S5-E10 | 3096 | 5173 | 1.671 | 11 |
| B3-S6-E10 | 3257 | 5258 | 1.614 | 11 |
| B4-S3-E10 | 4035 | 7896 | 1.957 | 16 |
| B4-S4-E10 | 3937 | 7551 | 1.918 | 14 |
| B4-S5-E10 | 4774 | 7252 | 1.519 | 16 |
| B5-S3-E10 | 3099 | 4637 | 1.496 | 11 |
| B5-S4-E10 | 3677 | 5793 | 1.575 | 13 |
| B5-S5-E10 | 4108 | 6140 | 1.495 | 13 |
| B6-S3-E10 | 4198 | 7125 | 1.697 | 14 |

**Table 4.1**: Polymer molecular weight and polydispersity index measured by gel permeation chromatography.

| Gene name | | Primer sequence (5′–3′) |
|---|---|---|
| $\beta$-Actin | Fwd. | AGTTGCGTTACACCCTTTCTTG |
| | Rev. | TCACCTTCACCGTTCCAGTTT |
| RUNX-2 | Fwd. | GTCTCACTGCCTCTCACTTG |
| | Rev. | CACACATCTCCTCCCTTCTG |
| OCN | Fwd. | GTGACGAGTTGGCTGACC |
| | Rev. | TGGAGAGGAGCAGAACTGG |
| OSN | Fwd. | TCGGCATCAAGCAGAAGGATA |
| | Rev. | CCAGGCAGAACAACAAACCAT |
| Col-1 | Fwd. | GAGAGGAAGGAAAGCGAGGAG |
| | Rev. | GGGACCAGCAACACCATCT |
| PDGF-B | Fwd. | GTTGAGGTGGCTGTAGATGGT |
| | Rev. | AGGGTGGAGGTAGAGAGATGAA |
| PDGFR-$\beta$ | Fwd. | TGAGGCTTTGGAGGAATC |
| | Rev. | CCTTGCTTCATCTGGACA |

**Table 4.2**: Primer sequences used for real-time polymerase chain reaction to study the osteogenic effect of PDGF-BB.

# Figures: Chapter 4

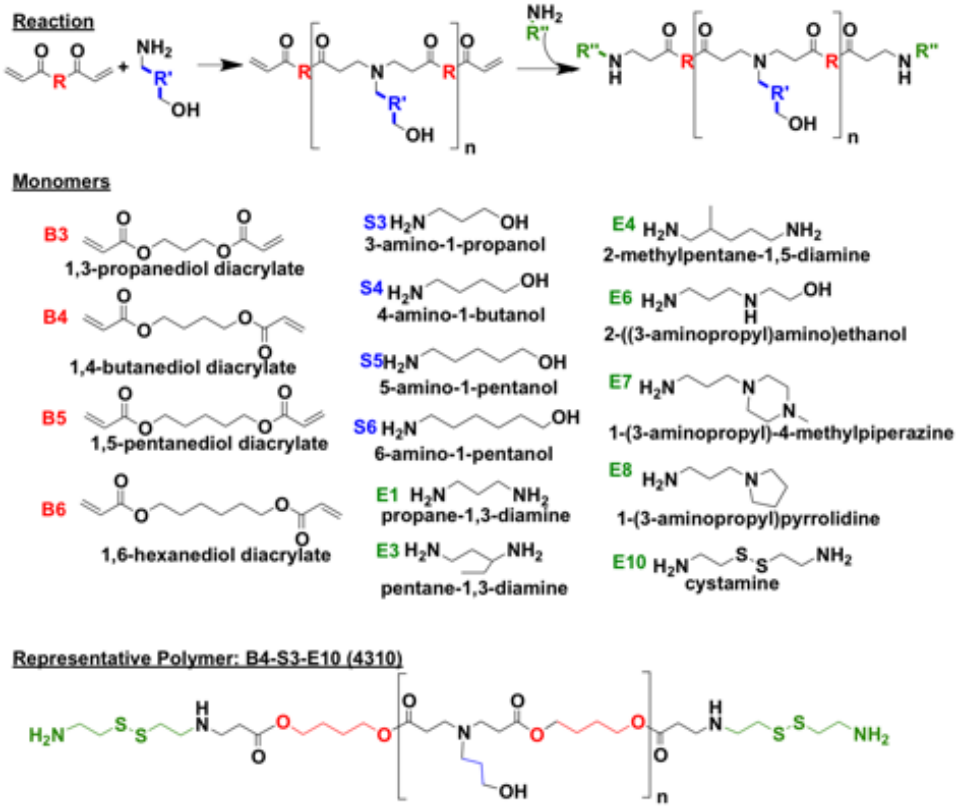


**Figure 4.1**: Polymer synthesis reaction and monomer structures. One backbone (B) and one sidechain (S) monomer are mixed to form an alternating copolymer via Michael addition. The resulting acrylate-terminated base polymer is functionalized with one end-cap (E) monomer.

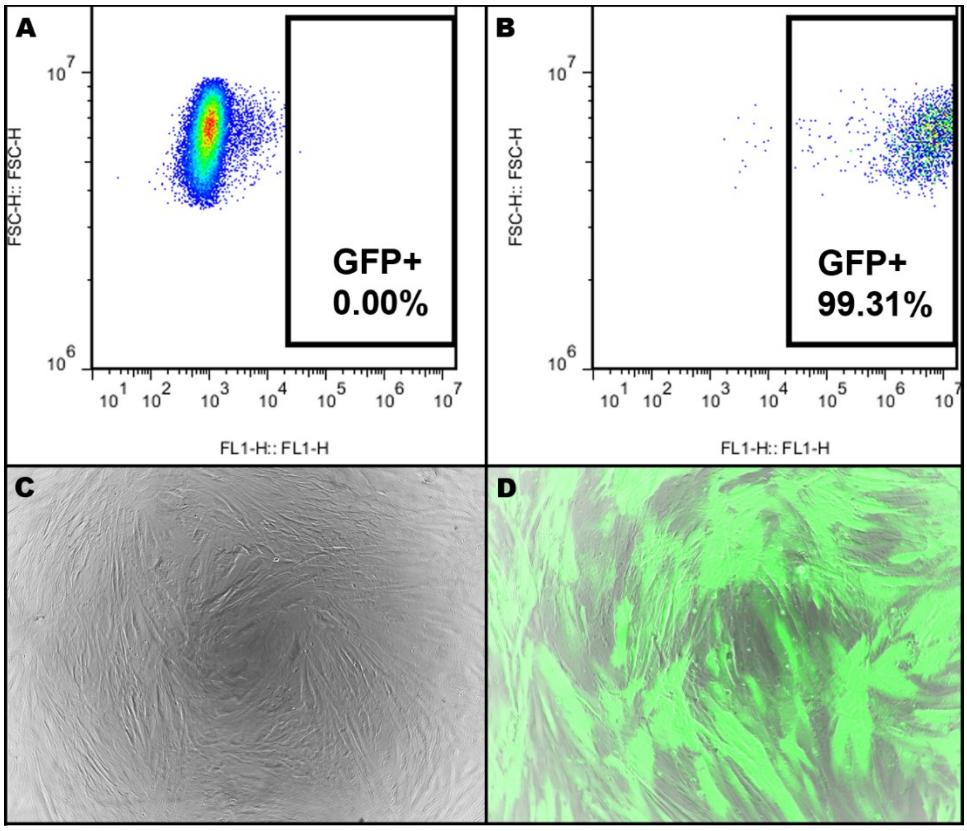


**Figure 4.2**: Flow cytometry (**A** and **B**) and fluorescence/brightfield imaging (**C** and **D**) confirmed the success of eGFP transduction of MSCs.

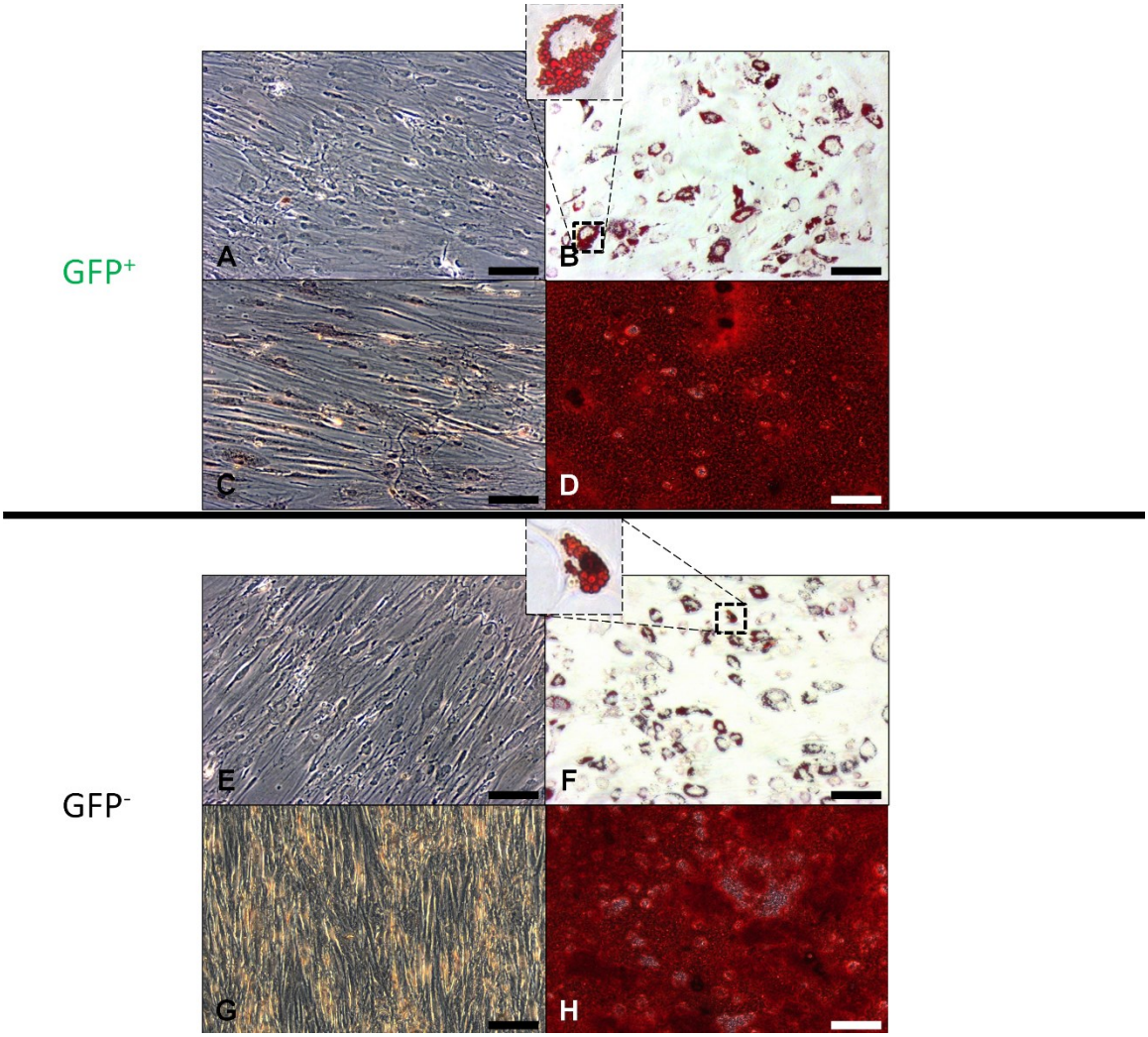


**Figure 4.3**: Transduced (**top**) and untransduced (**bottom**) MSCs were exposed to adipogenic (**B** and **F**) and osteogenic (**D** and **H**) cues. A corresponding set of cells was given expansion medium as a control (**A**, **C**, **E**, and **G**). Transduced cells underwent adipogenesis and osteogenesis comparable to untransduced controls as shown by Oil Red O staining of fat vacuoles and Alizarin Red S staining of calcification. Scale bar: 200 μm.

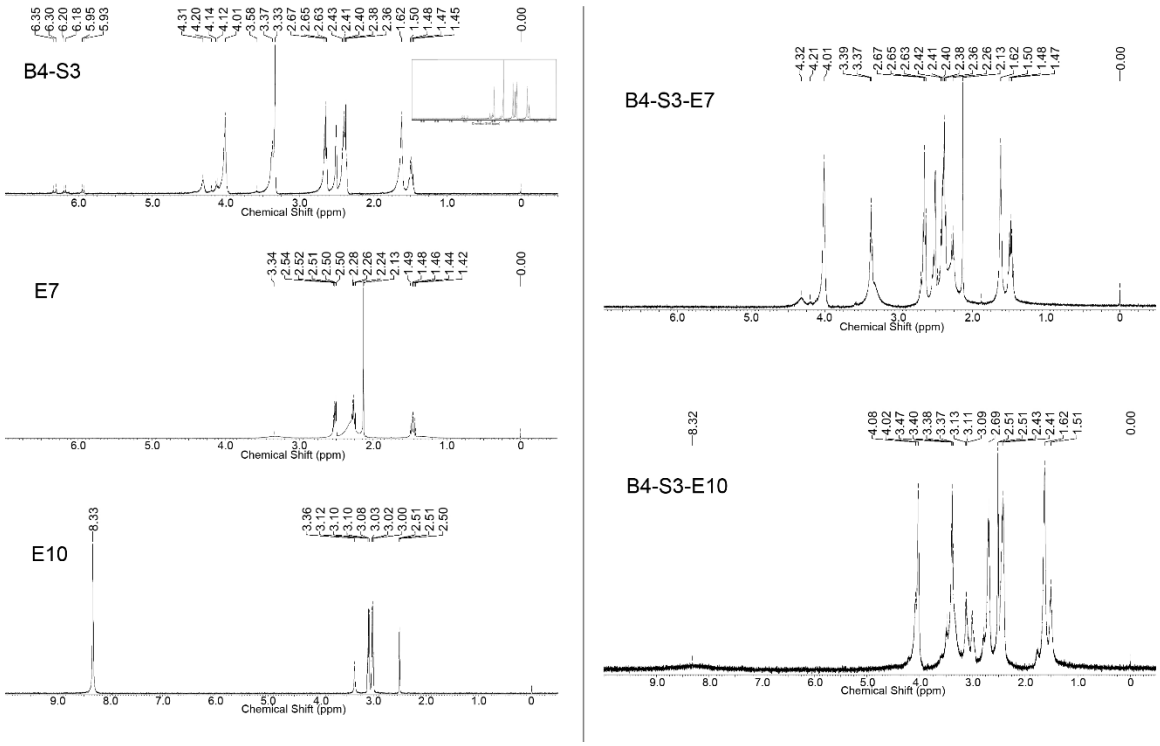


**Figure 4.4**: NMR spectra show the presence of expected peaks, including those corresponding to acrylate protons in the base polymer B4-S3 (**top left**), which are no longer present after end-capping is complete (**right**).

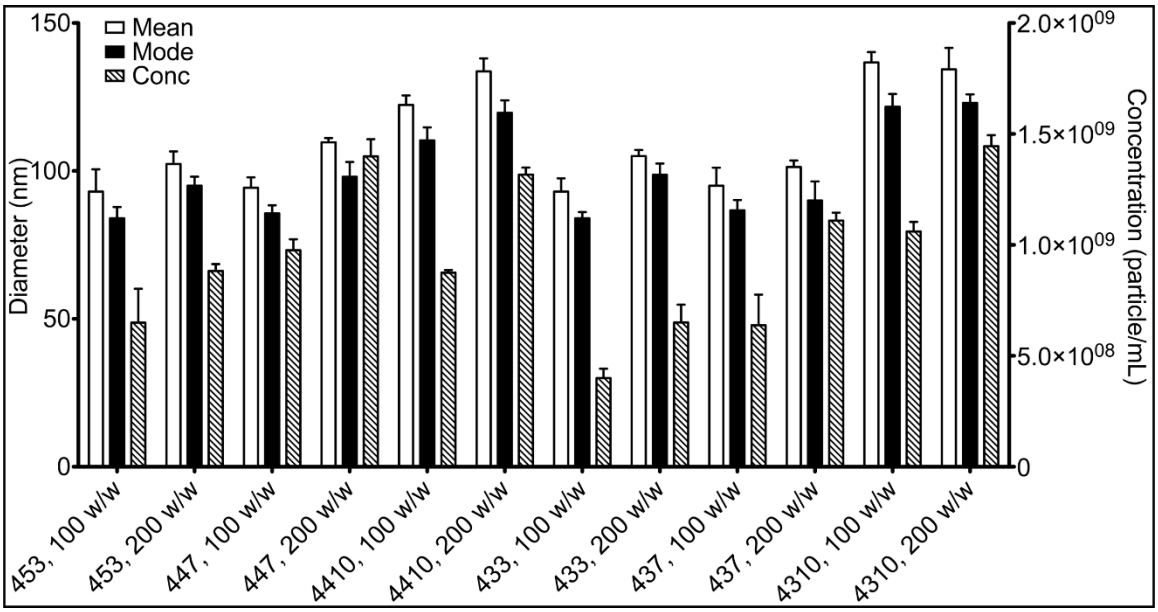


**Figure 4.5**: Nanoparticle tracking analysis. Number-averaged mean and mode particle size for all tested polymers was between 80 and 150 nm. Nanoparticle concentration was $0.5\text{-}2 \times 10^9$ /mL.

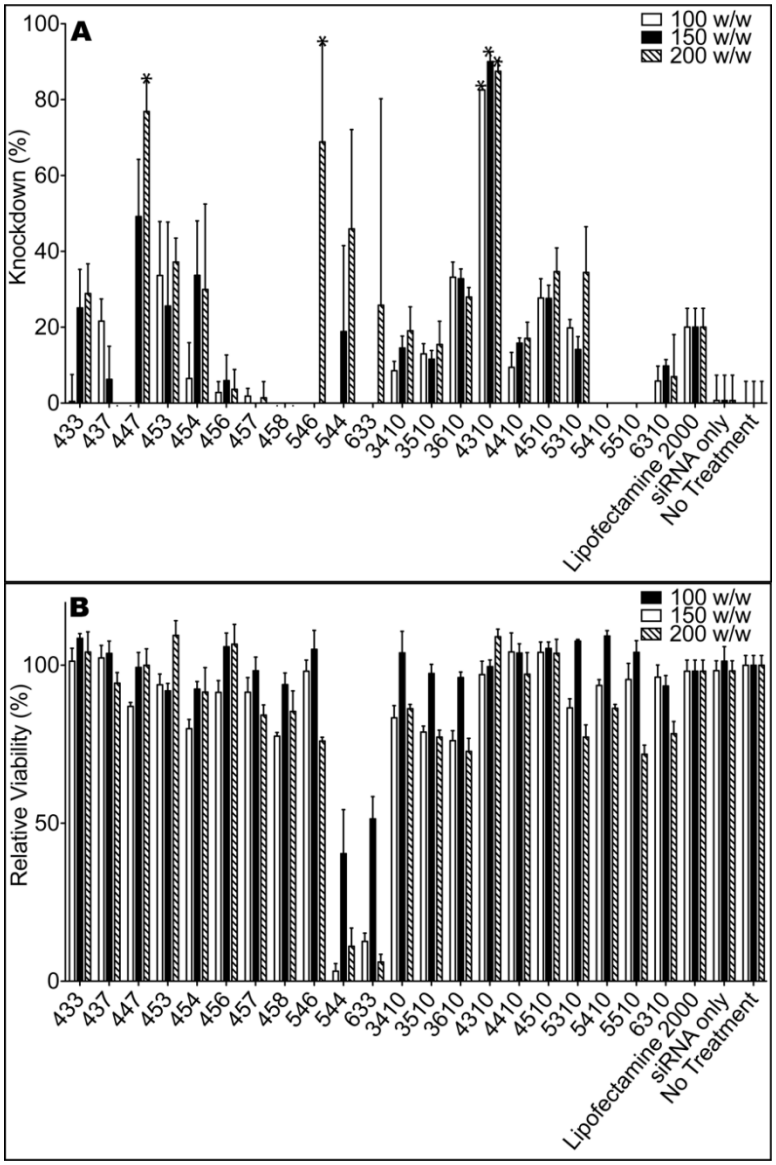


**Figure 4.6**: Nanoparticle induced knockdown and relative metabolic activity. (**A**) eGFP signal from cells transfected with siRNA was normalized to the signal from cells transfected with scrRNA and subtracted from 100% to calculate knockdown. Knockdown data are from 12 days post-transfection and *$p<0.01$. (**B**) Relative metabolic activity of nanoparticle-treated samples compared to untreated control. Metabolic activity measurements are from 24 h post-transfection.

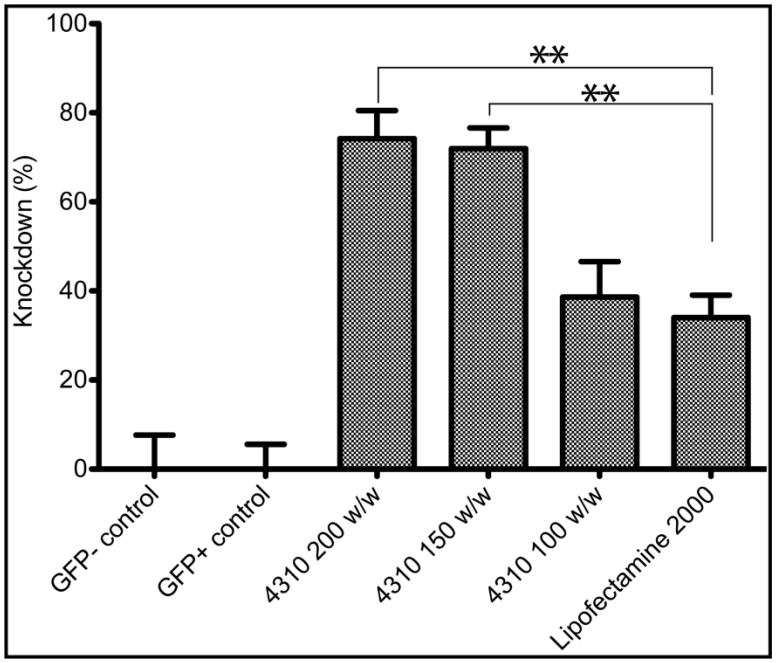


**Figure 4.7**: Median GFP intensity per cell, measured by flow cytometry 12 days after transfection with 4310, showed knockdown significantly superior to Lipofectamine™ 2000 transfection (**$p<0.01$).

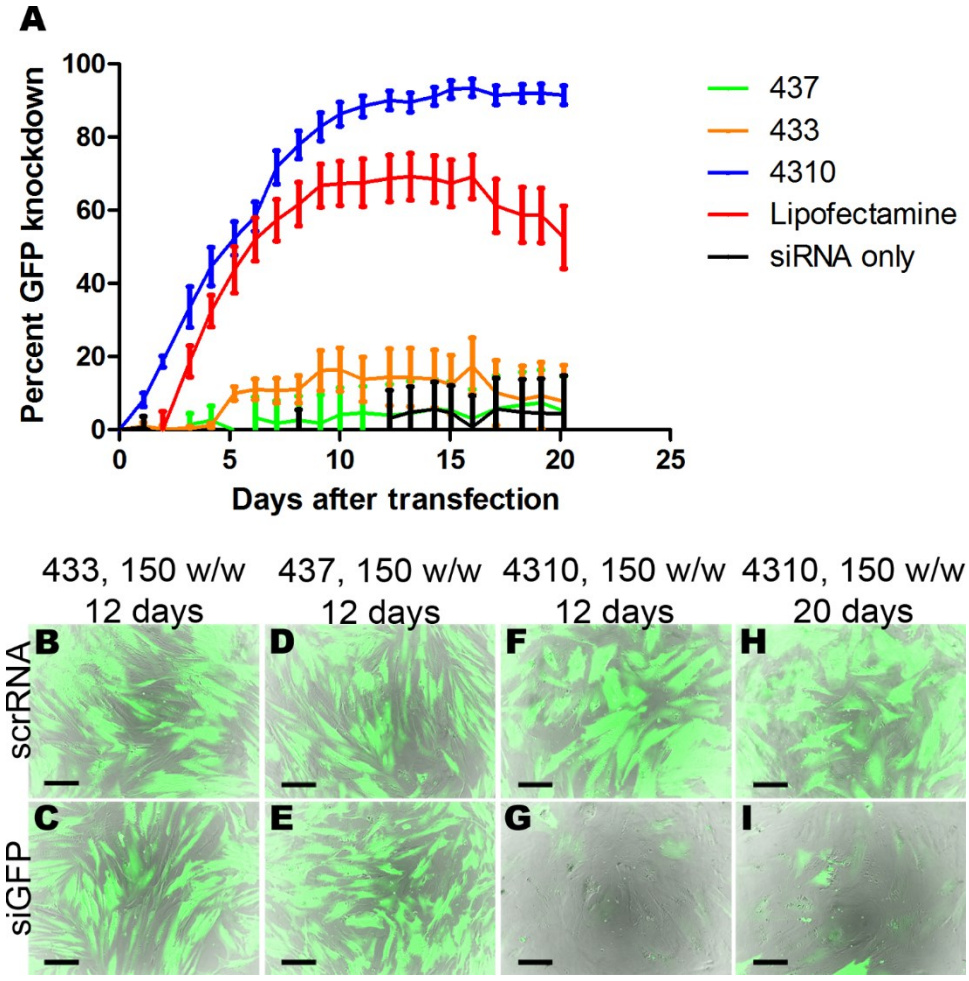


**Figure 4.8**: Comparison between 4310 and other vehicles of siRNA delivery. (**A**) At a weight ratio of 150 w/w, 433, 437, and naked siRNA induced little to no knockdown in contrast to Lipofectamine™ 2000 and 4310. 4310, in turn, outperformed Lipofectamine™ 2000, with robust knockdown still evident 20 days post-transfection. Fluorescence microscopy (**B-I**) supported observations from the plate reader. Scale bar: 200 µm.

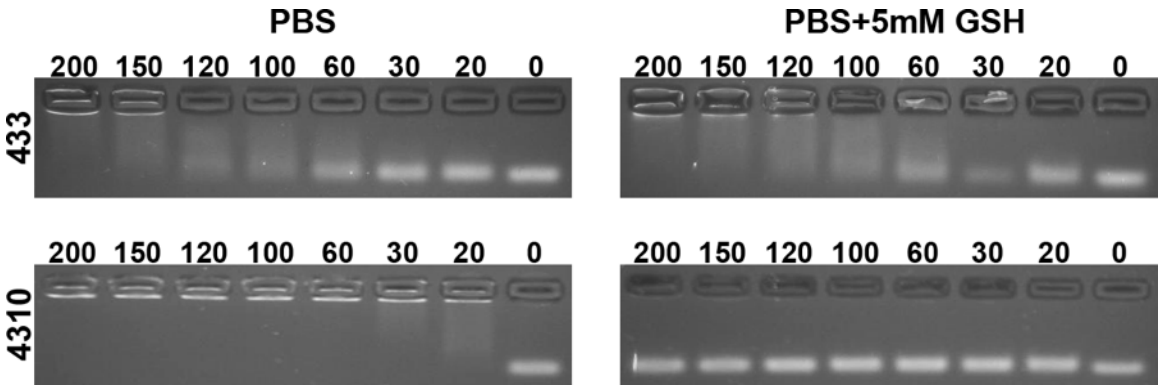


**Figure 4.9**: PBAE/siRNA binding evaluation. PBAE was added to siRNA at varying weight ratios, mixed with wither PBS alone or PBS with GSH (final 5 mM GSH concentration) and then added to the lanes of agarose gels. There is a progressively tighter binding and greater retardation of siRNA in the gel with greater weight ratios. 4310-based nanoparticles release siRNA in the presence of GSH, whereas 433-based nanoparticles do not release siRNA in the presence of GSH.

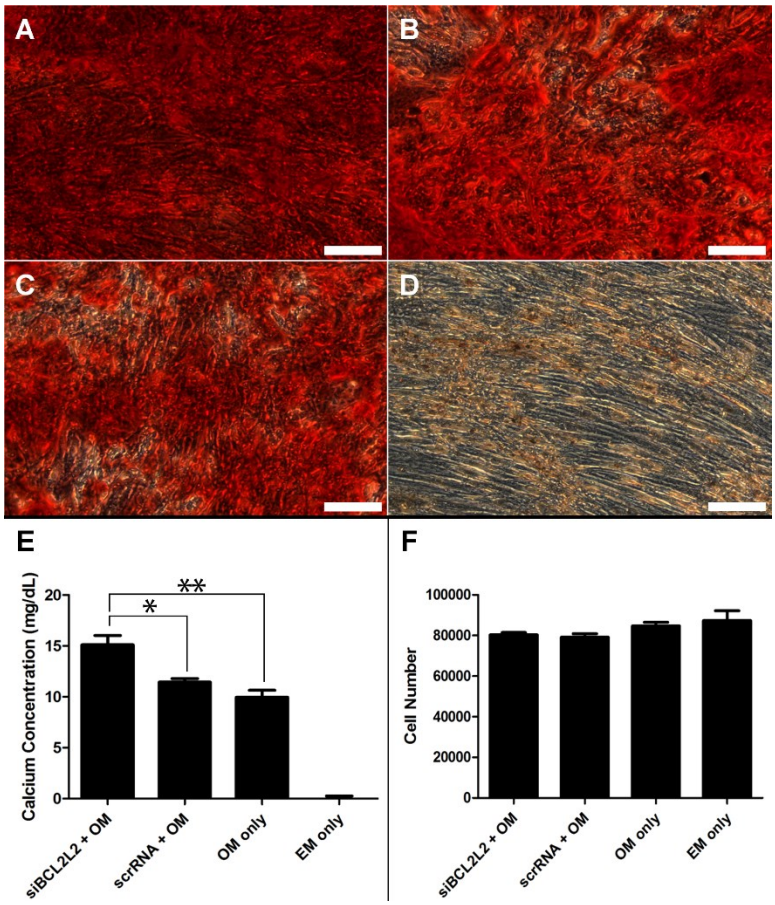


**Figure 4.10**: Quantification of osteogenesis and cell number. Alizarin Red S staining showed noticeably denser staining from cells given (**A**) siBCL2L2 + OM compared to cells given (**B**) scrRNA + OM and (**C**) cells given only OM. (**D**) Cells given EM only did not stain under Alizarin Red S. (**E**) Quantitatively, the siBCL2L2 + OM group produced more calcium than did the scrRNA + OM group and the OM-only group. No significant difference was found in calcium content between the scrRNA + OM and OM-only groups. (**F**) A DNA assay on replicate samples showed no difference in cell number between groups (one-way ANOVA ($p>0.05$), ruling out increased cell density as a cause for the increased calcium content. OM = osteogenic medium, EM = expansion medium. Scale bar: 200 µm.

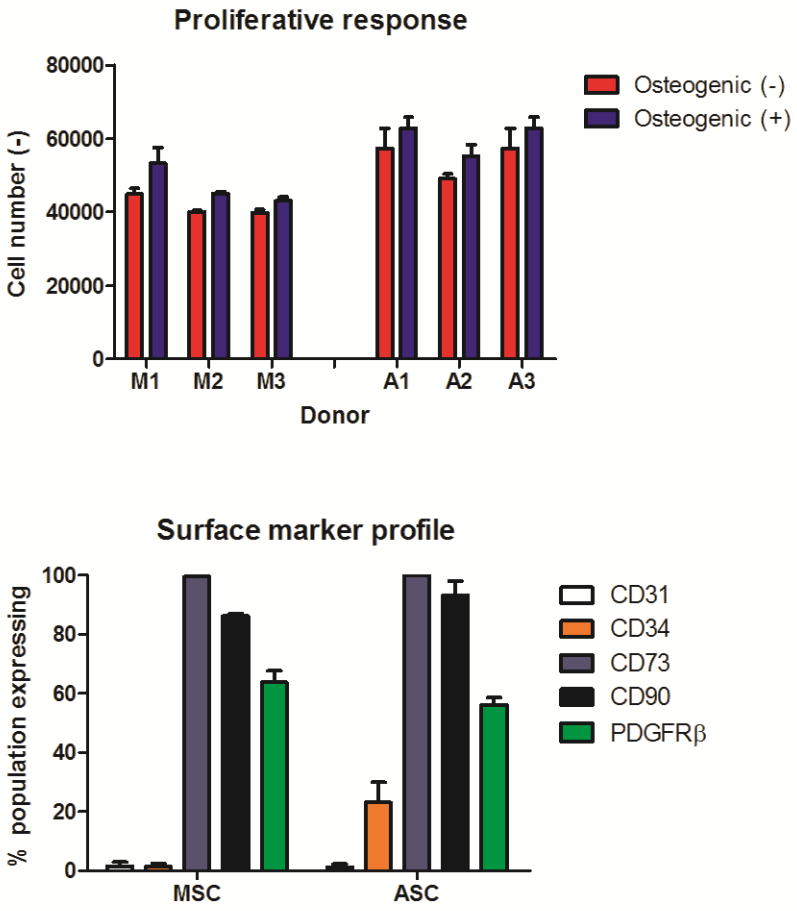


**Figure 4.11**: Characterization of cells used in this study. To ascertain that all cells could respond to exogenous PDGF-BB, cell proliferation was quantified by DNA assay at three weeks of culture under osteogenic (+) conditions (**top**). Indeed, all six cell populations irrespective of type and donor showed increased cell numbers relative to osteogenic (-) controls. Surface marker characterization of all six donors revealed profiles in good agreement with established features of mesenchymal stem cells (**bottom**; data reported as mean and standard error of mean computed from all three donors for a given cell type).

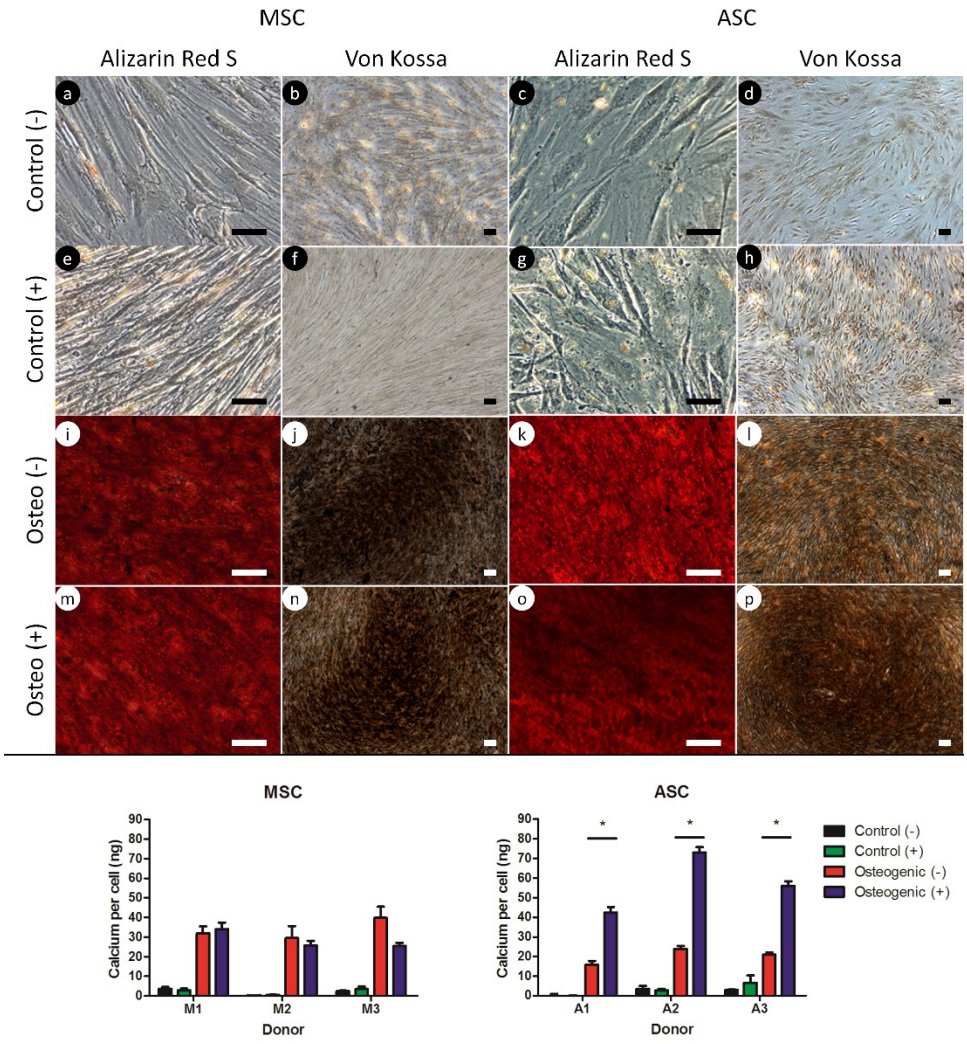


**Figure 4.12**: MSC and ASC mineralization under the effects of exogenous platelet-derived growth factor BB (PDGF-BB). MSCs and ASCs were cultured under control (-), control (+), osteogenic (-), and osteogenic (+) conditions for 3 weeks. Staining after 3 weeks of culture revealed no mineralization under either control condition (**A**-**H**) and an enhancement of mineralization under the presence of PDGF-BB in ASCs (**O**, **P** v. **K**, **L**) but not in MSCs (**M**, **N** v. **I**, **J**). Quantitative calcium per cell analysis revealed the increased mineralization was on a per-cell basis and the ASC-specific phenomenon was a donor-independent effect over six donors (**bottom**). Scale bar: 100 μm. *p<0.05.

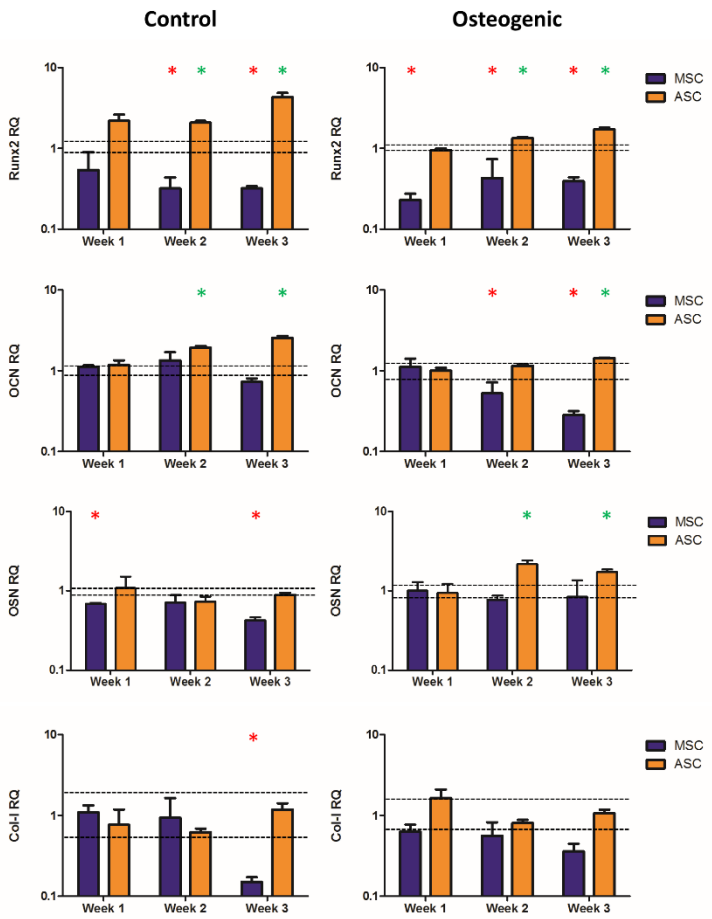


**Figure 4.13**: Gene expression of MSCs and ASCs under the effect of exogenous PDGF-BB. Gene expression analysis of osteogenic genes via RT-PCR showed that exogenous PDGF-BB under control (+) conditions tended to downregulate genes in MSCs while upregulating them in ASCs (**left**; normalized to expression under control (-) conditions, variation shown by dotted lines). The same observations held when considering osteogenic conditions (**right**; normalized to expression under osteogenic (-) conditions, variation shown by dotted lines). All expression quantities are relative to β-actin as housekeeping gene. Red asterisk denotes downregulation while green asterisk denotes upregulation compared to (-) conditions, $p<0.05$.

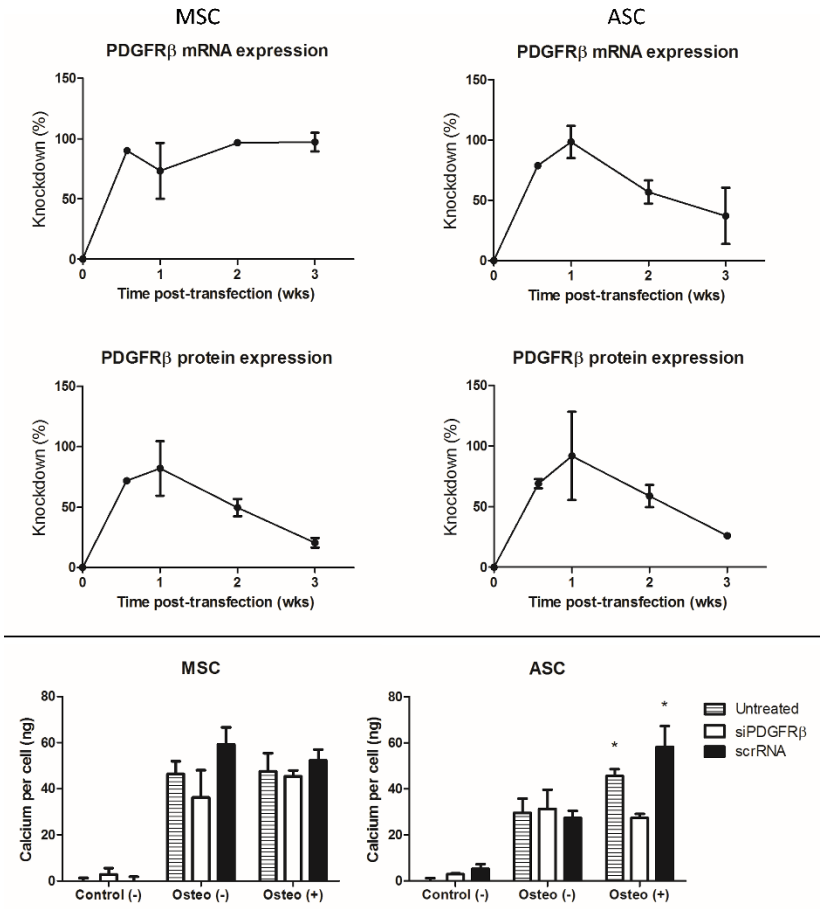


**Figure 4.14**: Loss-of-function experiment for the effect of exogenous PDGF-BB. siPDGFRβ was delivered to MSCs and ASCs using a reducible poly(β-amino ester) vehicle. Knockdown of receptor relative to a scrambled control was evident for more than 3 weeks via both RT-PCR and antibody-based flow cytometry (**top**). While MSC mineralization at 3 weeks post-transfection was unaffected irrespective of treatment or the presence of PDGF-BB, silenced ASCs lost the enhancement of mineralization under osteogenic (+) conditions in contrast to untreated ASCs or ASCs given the scrambled control. *$p<0.05$ compared to corresponding osteogenic (-) quantities via two-way ANOVA.

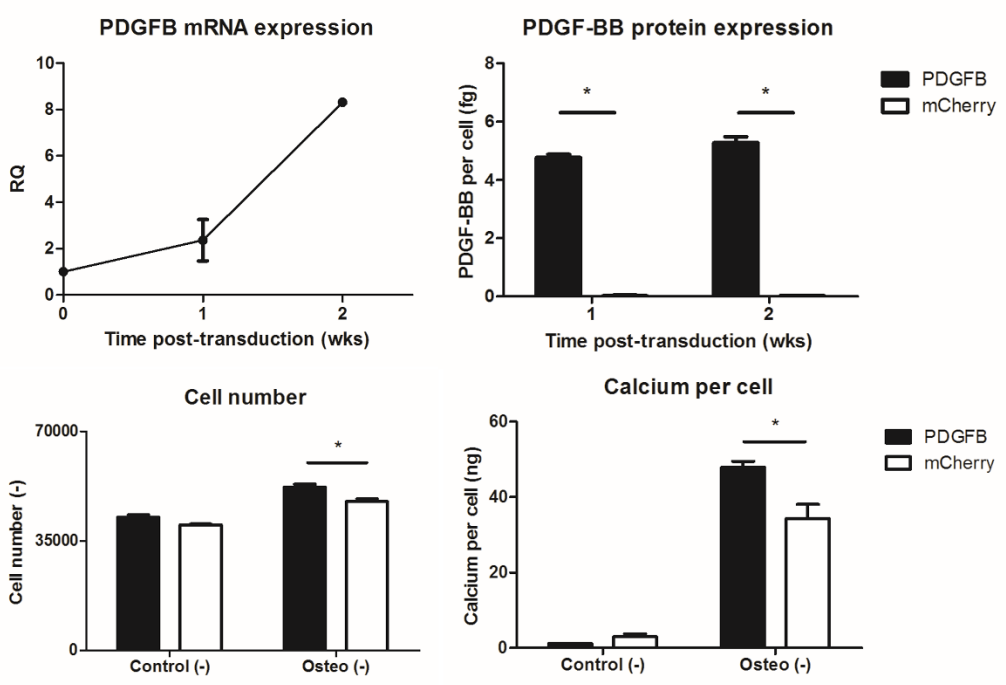


**Figure 4.15**: Verification of lentiviral transduction. Lentivirus containing the gene PDGFB or mCherry was used to transduce ASCs. PDGFB-transduced ASCs overexpressed the gene and produced more protein compared to mCherry-transduced controls as determined by RT-PCR and ELISA (**top**). The produced protein had a functional effect, increasing cell proliferation and calcium-per-cell content as evidenced by DNA and calcium assays (**bottom**). *$p<0.05$.

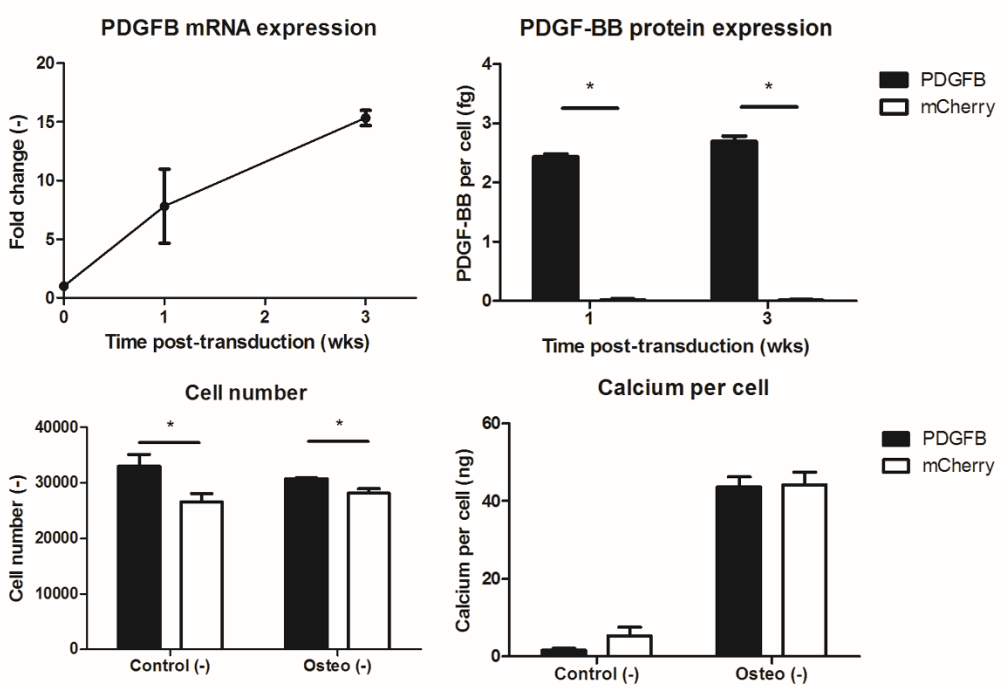


**Figure 4.16**: Lentiviral transduction on MSCs. Similar to studies with ASCs (shown in **Figure 4.15**), MSCs were transduced with PDGFB or mCherry. Transduction was verified by increased mRNA and protein expression (**top**) as well as by a mitogenic response (**bottom left**); however, the transduction had no effect on MSC calcium production per cell (**bottom right**). *$p<0.05$.

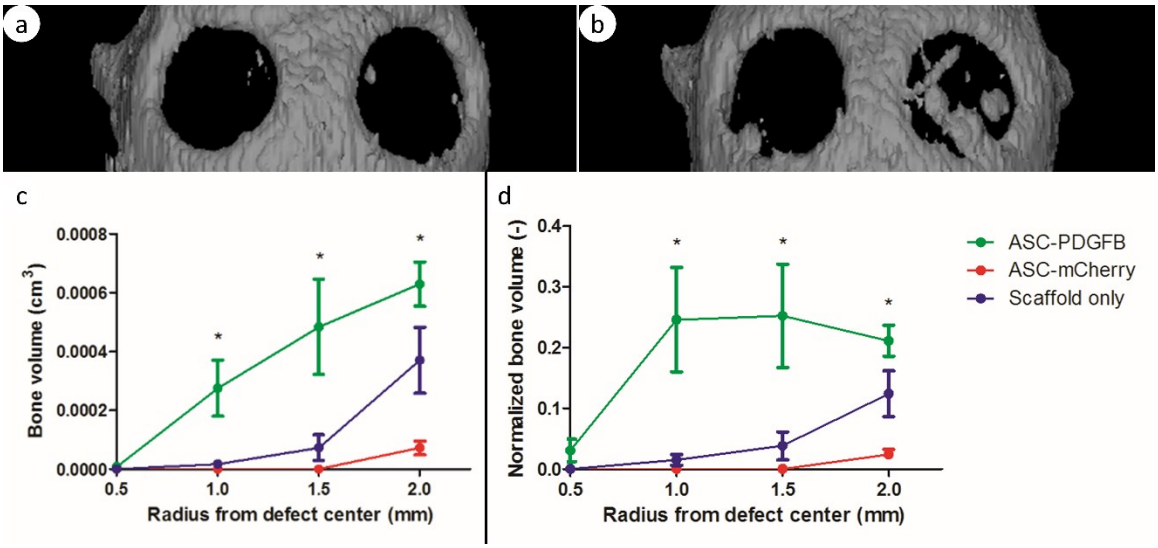


**Figure 4.17**: Computed tomography analysis of in vivo regeneration. Scaffolds seeded with mCherry-transduced ASCs (**A**, right defect), PDGFB-transduced ASCs (**B**, right defect), or empty fibrin (**A**-**B**, left defects) were implanted in critically sized 4-mm-diameter murine calvarial defects for 8 weeks. Computed tomography reconstructions (**A**-**B**) were used for quantification of bone volume within the defect. In terms of both absolute bone volume (**C**) and bone volume normalized to unoperated values (**D**), the PDGFB-transduced ASCs produced significantly more bone volume beginning at a 2-mm radius within the defect compared to both other groups. *$p<0.05$ via one-way ANOVA.

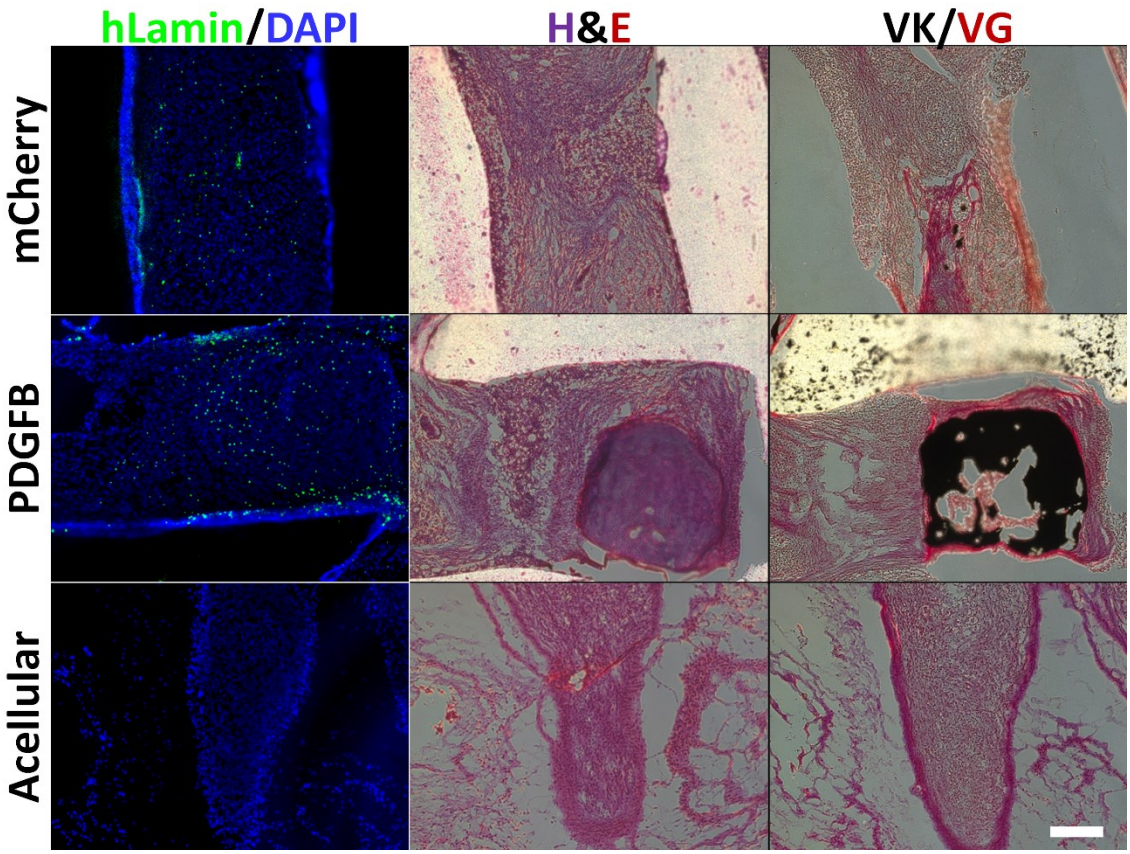


**Figure 4.18**: Histological analysis of in vivo regeneration. Eight weeks post-implantation, mice were sacrificed and scaffolds excised. Immunohistochemistry for human-specific Lamin A/C (**left**), H&E (**middle**), and von Kossa/van Gieson (**right**) was performed to assess retention of human cells, scaffold cellularity, and bone formation, respectively. The majority of mineralization (von Kossa staining, black) occurred in the PDGFB-transduced group. The implanted human cells (human Lamin A/C, green) were retained within all scaffolds, with positive staining evident in all groups except for the acellular group, where no human cells were implanted. Scale bar: 200 μm.

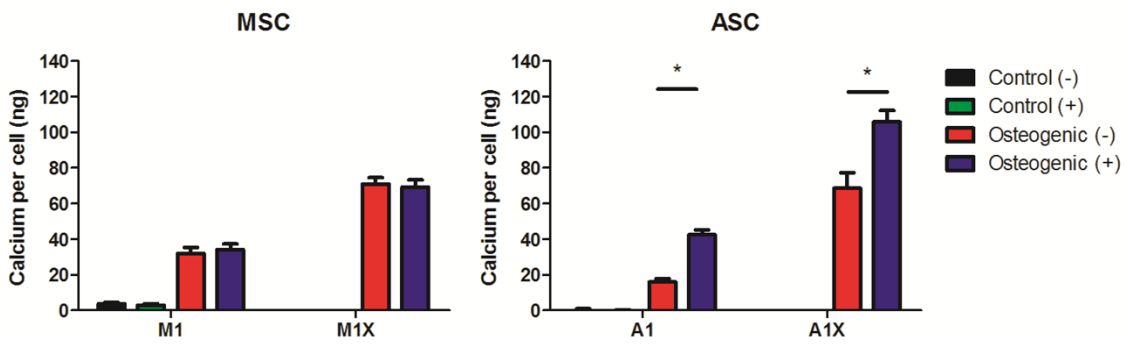


**Figure 4.19**: Effect of dexamethasone on MSC and ASC osteogenesis. To confirm that PDGF-BB enhances ASC, but not MSC, osteogenesis regardless of the presence of dexamethasone, 100 nM dexamethasone was added to all osteogenic medium conditions for both cell types and the calcium/cell experiment repeated for three weeks. Dexamethasone greatly increased calcium per cell for both MSCs and ASCs, but the PDGF-BB-dependent enhancement of mineralization remained specific to ASCs.

# Chapter 5: in vivo imaging of implanted stem cells

This chapter may be adapted into a future publication.

## 5.1. Introduction

The use of stem cells in tissue engineered constructs is prevalent and is motivated by evidence that stem cells have beneficial effects on healing of defects. For instance, cellular constructs implanted into critically sized rat femoral defects resulted in significantly higher regenerated bone volume, maximum torque, and torsional stiffness compared to acellular controls [177]. In another study, histological analysis of an implanted construct in a human mandibular defect revealed dramatically higher amounts of new bone in bioprinted cellular constructs compared to scaffold-only implants [178]. As such, while it is evident that stem cells can greatly augment tissue engineered methods, the action of implanted stem cells within tissue engineering constructs remains a poorly understood subject as discussed in Chapter 1, section 1.4. The classical paradigm, that implanted stem cells directly differentiate into replacement tissue, was called into question from studies that found widely varying levels of implanted stem cell retention. A study performing histology on constructs excised 3 weeks post-implantation in a murine calvarial defect found that only ~5% of the area fraction consisted of retained implanted cells [179]. A different study, also using the murine calvarial defect model, visualized implanted stem cells by bioluminescence imaging (BLI) and reported little loss of signal 3 weeks post-implantation [118], suggesting high cell retention. Still other studies have been wholly unable to find implanted stem cells post-implantation [177]. Given that stem cells take around 3 weeks to differentiate into bone in vitro, the

inconsistency of their long-term presence in implant sites provides ample motivation for further investigation on whether direct differentiation is actually occurring in vivo.

To perform such an investigation requires an in vivo stem cell imaging modality with specific capabilities. First, the modality should allow for longitudinal tracking – a given stem cell population implanted in a given animal should be monitored over a period of time rather than taking timepoints from different populations in different animals [180]. This consideration is due to the heterogeneity between cells and animals: a process occurring in one animal may not necessarily be reflective of the process occurring in another. Second, the resolution of the modality should be high enough such that the spatiotemporal profile of implanted cells can be well-defined. Another consideration for resolution is the ability to correlate the spatiotemporal profile of implanted cells with high-resolution tissue imaging modalities, such as computed tomography as has been used previously in this dissertation. As a benchmark for resolution, previous studies have shown that high-resolution computed tomography methods can visualize trabecular architecture with a voxel size of ~80 $\mu m^3$ [181]. Third, the imaging modality should be non-invasive to both the animal and to the cells [180]. Imaging should observe rather than interfere, and a modality that alters the course of stem cell behavior in vivo would give altered information about in vivo regenerative processes. Finally, the modality should feature depth-independence for scalability to large-animal models. Small-animal models do not always recapitulate in vivo processes in larger organisms, such as humans. For instance, mass transport considerations that are absent in a murine critically sized defect (~mm) are major challenges in human critically sized defects (~cm) [182]. As such, imaging modalities must be able to visualize implants in large animals without

attenuation of signal due to depth within the body for a clear understanding of how implanted stem cells behave in models that can recapitulate the situation in patients.

Several imaging modalities have emerged to monitor implanted stem cells; however, each has key drawbacks related to one or more of the above requirements. For instance, the simplest and perhaps the most widely used method of detecting implanted cells is to sacrifice the animal, excise the implant, and perform histology, as was shown in **Figure 4.18**. This method is invasive and not longitudinal, meaning it is impossible to visualize whether the implanted ASCs formed bone over the course of the study. It is only possible to extract a correlation between the presence of human cells and the presence of mineral at the final timepoint of the study.

Another class of methods that has been used can be referred to as particle-based methods, in which particles detectable under an imaging modality, such as MRI, are inserted into implanted cells. For MRI, the particles are generally magnetic iron-based, such as superparamagnetic iron oxide (SPIO) or bionized nanoferrite (BNF) nanoparticles [183-186]. MRI fits the requirements that have been outlined; however, the particle-based methods of labeling cells have two distinct drawbacks. First, it has been shown that labeling MSCs with SPIO nanoparticles negatively affects their differentiation capability down the three classical mesenchymal lineages [187]. In addition, our own studies into the effect of BNF labeling of ASCs has shown that it negatively inhibits cell viability as determined by MTS. At the concentrations used in literature (600 μg/mL [185]), ASCs experienced a decrease in viability of around 40% (**Figure 5.1**). A second drawback is the ability of macrophages to uptake the nanoparticles after implanted cell death. Since the particles are intact and detectable, MRI will still visualize them, despite the loss of

implanted cells [188]. Data also suggests this occurs with other particle-based imaging modalities, such as with quantum dots [177].

To overcome this drawback, live-cell imaging reporters have been used. The main modality in this category is luciferase-based bioluminescence, which has been widely used for visualizing processes in vivo [180]. Implanted stem cells expressing the luciferase gene would be exposed to luciferin, which would be converted to bioluminescence-emitting oxyluciferin only if living cells are actively expressing luciferase. As such, dead cells cannot be inadvertently detected under BLI. BLI is easy to use and is amenable for non-invasive, longitudinal, in vivo imaging of implanted stem cells. Despite this, BLI is a low-resolution method, generally used for whole-body imaging, and the attenuation of bioluminescence through tissue limits the method to small animals. It is estimated that for each centimeter of tissue bioluminescence must pass through, there is a 10-fold attenuation in signal [189].

A new imaging modality was developed that takes advantage of chemical exchange saturation transfer (CEST), a process in which a proton on a biomolecule is saturated by a magnetic pulse and transfers to surrounding water protons, thus enhancing the contrast of the original biomolecule [190, 191]. To exploit this property, biomolecules containing CEST-compatible protons are aggregated in cells, thereby rendering the cells visible under CEST-MRI. For example, it has been shown that a chain of lysine residues contains a CEST-compatible amine proton that has a resonant saturation frequency of 3.76 ppm, compared to water at 0 ppm [192]. As such, if cells are transfected/transduced with a gene encoding long lysine chains, the cells will be visible under CEST-MRI at 3.76 ppm. A newer but similar method instead overexpresses a thymidine kinase –

specifically, herpes simplex virus type 1 thymidine kinase (HSV1-tk) – that then traps a modified thymidine (containing a CEST-compatible proton) inside the cell, thereby allowing for visibility under CEST-MRI at approximately 5 ppm [193, 194]. This method relies on MRI and is therefore high-resolution and depth-independent. It requires the labeled cells to be alive and expressing the CEST agent (or thymidine kinase to entrap and concentrate the CEST agent), so it is similar to the live-cell tracking properties of BLI. MRI also allows for longitudinal and non-invasive imaging. These considerations suggest CEST-MRI may be an attractive imaging modality to monitor implanted stem cells, satisfying the required capabilities outlined above.

In this study, CEST-MRI is investigated in its potential to monitor implanted ASCs in the murine calvarial defect. ASCs were labeled and assessed for their proliferation as well as for tri-lineage differentiation potential. Following that, they were implanted in the murine calvarial defect and imaged under CEST-MRI.

## 5.2. Materials and methods

### *5.2.1. Labeling of ASCs*

P2 ASCs were transduced to express HSV1-tk, the intended use of which is to entrap 5-methyl-5,6-dihydrothymidine (5-MDHT), a modified thymidine kinase that was synthesized for compatibility with CEST-MRI [193]. HSV1-tk traps 5-MDHT within ASCs by phosphorylation of the 5’ hydroxyl. The –NH hydrogen is then able to exchange with nearby water hydrogens for CEST. Because 5-MDHT is trapped and concentrated within ASCs, the ASCs are visible under CEST-MRI.

To transduce ASCs with HSV1-tk, lentiviral transduction was performed as described previously [195, 196]. Briefly, a lentiviral vector containing the gene for HSV1-tk under the cytomegalovirus (CMV) promoter was packaged into lentivirus using the ViraSafe Lentiviral Packaging System (Cell Biolabs, San Diego, CA) with 293T cells as a sacrificial cell type. Virus was applied to ASCs the day after plating at 6000 /cm$^2$ and transduction was allowed to continue for 72 hours, at which point virus was removed and ASCs were allowed to grow to confluence. Transduction success was verified by Western blot and blasticidin selection. As a control for the experiments outlined below, ASCs were also transduced with green fluorescence protein (GFP) using the same procedure outlined above.

*5.2.2. Tri-lineage differentiation and proliferation of labeled ASCs*

Osteogenic differentiation proceeded as previously described [85, 195, 196]. ASCs were plated at 5000 /cm$^2$ and cultured for 3 weeks under Dulbecco's Modified Eagle Medium (DMEM) with 1 g/L glucose, 6% v/v fetal bovine serum (FBS), 100 U/mL penicillin and 100 μg/mL streptomycin (Cellgro, Manassas, VA), 10 mM β-glycerophosphate (Sigma Aldrich, St. Louis, MO), and 50 μM ascorbic acid (Sigma Aldrich). Monolayers were assessed for osteogenic differentiation by Alizarin Red S (Sigma Aldrich) staining and calcium per cell assay. Calcium assay was performed with the Stanbio LiquiColor calcium assay (Stanbio, Boerne, TX) and cell number was determined with the Quant-iT PicoGreen dsDNA assay (Invitrogen, Carlsbad, CA).

Adipogenic differentiation proceeded as previously described [85, 195]. ASCs were plated at 10000 /cm$^2$ and cultured for 3 weeks under DMEM with 4.5 g/L glucose,

10% v/v FBS, 100 U/mL penicillin and 100 µg/mL streptomycin, 5 µg/mL recombinant human insulin (Invitrogen), 1 µM dexamethasone (Sigma Aldrich), 200 µM indomethacin (Sigma Aldrich), and 500 µM 3-isobutyl-1-methylxanthine (Sigma Aldrich). Monolayers were assessed for adipogenic differentiation by Oil Red O (Sigma Aldrich) staining and triglyceride per cell assay. The triglyceride assay was performed with the Serum Triglyceride Determination Kit (Sigma Aldrich) and cell number was determined with the Quant-iT PicoGreen dsDNA assay.

Chondrogenic differentiation proceeded as previously described [85]. ASCs were pelleted at 250000 cells per pellet and cultured for 3 weeks under DMEM with 4.5 g/L glucose, 100 U/mL penicillin and 100 µg/mL streptomycin, 1 µM dexamethasone, 10 ng/mL transforming growth factor β3 (PeproTech, Rocky Hill, NJ), 50 µM ascorbic acid, 110 µg/mL sodium pyruvate (Sigma Aldrich), 40 µg/mL L-proline (Sigma Aldrich), and ITS (10 µg/mL bovine insulin, 5.5 µg/mL human transferrin, 6.7 ng/mL selenium; Sigma Aldrich). Pellets were cryo-sectioned and stained with Safranin O (ScholAR Chemistry, West Henrietta, NY) for qualitative assessment of chondrogenesis. For sectioning, samples were fixed in 3.7% formalin overnight and fixed samples were infiltrated with 30% sucrose, frozen in Tissue Tek OCT medium, and cut into 10 µm thick sections. Cryosections were mounted and dried on Superfrost Plus slides, followed by rehydration in water before staining. Quantitatively, pellets were subject to glycosaminoglycan (GAG) per cell assessments using the 1,9-dimethylmethylene blue (DMMB) assay as follows. Pellets were first digested in papainase III buffer overnight at 60 °C. Buffer was prepared by creating PBE buffer consisting of 14.2 mg/mL $Na_2HPO_4$ (Sigma Aldrich) and 3.72 mg/mL ethylenediaminetetraacetic acid (EDTA; Sigma Aldrich), then

dissolving L-cysteine (Sigma Aldrich) at 1.75 mg/mL PBE buffer and adding papain (Worthington Biochemicals, Lakewood, NJ) at 6.64 U/mL. Supernatant from the digest was combined with a DMMB solution consisting of 3.36 mg/mL glycine (Sigma Aldrich), 2.62 mg/mL NaCl (Sigma Aldrich), and 17.68 mg/mL DMMB for quantification of GAG content. A separate set of pellets were subject to the Quant-iT PicoGreen dsDNA assay to determine cell number.

For proliferation, ASCs were plated at 5000 /cm$^2$ and cultured for 3 weeks under DMEM with 4.5 g/L glucose, 10% v/v FBS, 100 U/mL penicillin and 100 µg/mL streptomycin, and 1 ng/mL basic fibroblast growth factor (bFGF; PeproTech). Monolayers were assessed with the Quant-iT PicoGreen dsDNA assay.

*5.2.3. In vivo imaging*

ASCs were seeded into 3D-printed polycaprolactone (PCL) scaffolds [86] as described previously [196]. Briefly, ASCs were suspended in fibrinogen and combined with thrombin to create fibrin gels consisting of final concentrations 8 mg/mL fibrinogen, 2 U/mL thrombin, and $2 \times 10^7$ ASCs/mL. Before gelation, fibrin solutions were pipetted into the pore spaces of 3D-printed scaffolds of dimensions 0.644 mm height, 4 mm diameter, and 60% porosity.

Resulting constructs were implanted into 4-mm critically sized murine calvarial defects as previously described [196]. All procedures were reviewed and approved by the Johns Hopkins Animal Care and Use Committee. 8-week-old male FOXN1-knockout mice (Jackson Laboratories, Bar Harbor, ME) were anesthetized and a 4-mm circular knife (Medicon, Tuttiligen, Germany) was used to excise a 4-mm disk of calvaria

between the coronal and lambdoid sutures and 1 mm lateral to the sagittal suture with care taken to preserve the underlying dura mater. Constructs were implanted in the resulting defects and 10 μL of fibrin was pipetted over them to hold them in place. For each mouse, two defects were created. On the right side, constructs containing ASCs transduced with HSV1-tk were implanted while constructs containing GFP-transduced ASCs were implanted in the contralateral side as a control.

Immediately post-implantation, mice were injected through the tail vein with 150 mg/kg 5-MDHT. Mice were allowed to remain awake and mobile for three hours before imaging, a timepoint that was determined in previous studies [194].

## 5.3. Results

### *5.3.1. Effect of transduction on ASCs*

The lentiviral transduction was successful, with transduced cultures surviving under blasticidin treatment 2 weeks post-transduction. In addition, Western blot assessments on transduced ASCs revealed a positive band, in contrast to no band from untransduced ASCs (**Figure 5.2**).

Both qualitative (**Figure 5.3**) and quantitative (**Figure 5.4**) assessments showed no effect of transduction, both with HSV1-tk and GFP, on ASC osteogenic and adipogenic differentiation; however, chondrogenic differentiation was significantly inhibited by both HSV1-tk and GFP transduction. ASC proliferation as determined by cell numbers after 3 weeks of culture was unaffected by transduction. Because ASC osteogenic capability was unaffected by HSV1-tk labeling, the method was deemed suitable for further investigation into bone engineering models.

*5.3.2. In vivo imaging of murine calvarial defect*

CEST-MRI of the murine calvarial defects (**Figure 5.5**) three hours post-injection of 5-MDHT revealed higher CEST contrast in the animal's right defect, where ASCs transduced with HSV1-tk had been implanted. GFP-transduced ASCs on the left side showed minimal signal.

## 5.4. Discussion

In this study, the suitability of CEST-MRI for in vivo tracking of implanted ASCs was investigated. Specifically, the effect of labeling on ASCs was determined and a pilot imaging experiment was performed to determine whether labeled ASCs would be visible under CEST-MRI.

A key observation in this early-stage study is the negative effect of transduction on ASC chondrogenic capability. GAG content in transduced ASCs was notably reduced as evidenced by both Safranin O staining and DMMB assay. This occurred regardless of gene transduced – GFP or HSV1-tk – suggesting the effect is due to transduction and not due specifically to HSV1-tk. Given the ability of other studies to achieve chondrogenesis of stem cells post-transduction (e.g. [197]), this observation is likely due to the specific transduction protocol used here rather than a biological phenomenon. As such, potential future applications involving cartilage repair models would require more careful investigation of the effects of lentiviral labeling. Despite this, the data shows no effect on other aspects of ASC potency, most notably osteogenic capacity, so the method was further investigated.

Labeled ASCs were distinguishable from GFP-transduced ASCs under CEST-MRI, with a maximum contrast level approximately three times higher. This is comparable to previous studies using 5-MDHT as a contrast agent to visualize brain tumors in the rat, which reported a contrast approximately two-fold higher in labeled versus wild-type cells [194]. Notably, the injection of 5-MDHT in this experiment occurred immediately after implantation of the constructs, meaning host vasculature had not yet invaded into the construct during the incubation period. As such, the contrast observed in this experiment is solely due to ASC uptake of 5-MDHT that diffused into the region rather than directly delivered by vasculature. It is possible that, as vasculature develops into the construct, that CEST contrast would be enhanced. Ongoing long-term imaging studies will elucidate such effects further.

In conclusion, this study presents a proof-of-concept that CEST-MRI can be used to visualize ASCs in bone engineering constructs. Future studies will utilize CEST-MRI to investigate the long-term retention and viability of implanted ASCs as well as their in vivo osteogenesis.

# Figures: Chapter 5

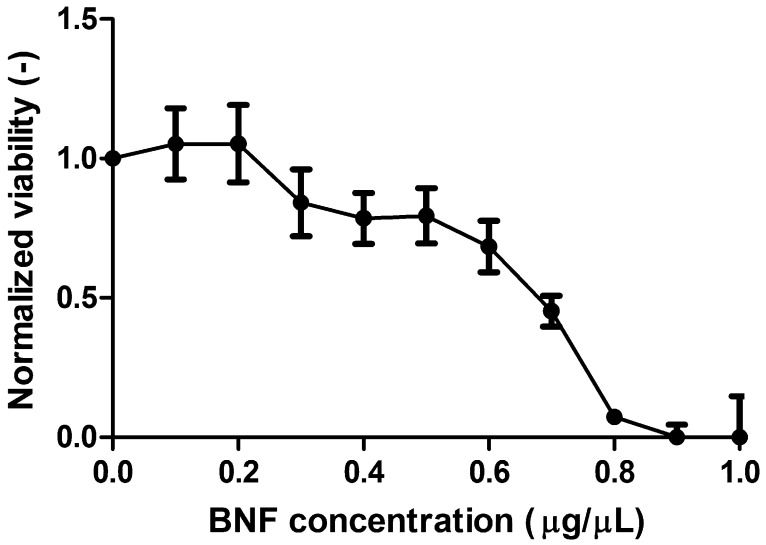


**Figure 5.1**: Effect of BNF labeling on ASC viability. Using MTS, readings from ASCs labeled with varying concentrations of BNF nanoparticles were normalized to untreated ASCs. Viability of labeled ASCs drops with increasing concentration of BNF.

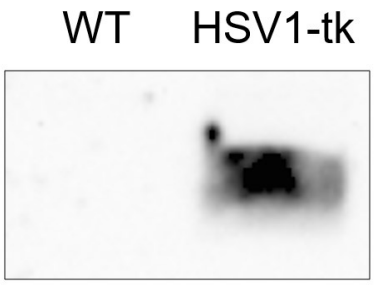


**Figure 5.2**: Western blot of transduced ASCs 2 weeks post-transduction. A protein band is visible in transduced (right) but not in untransduced (left) cells.

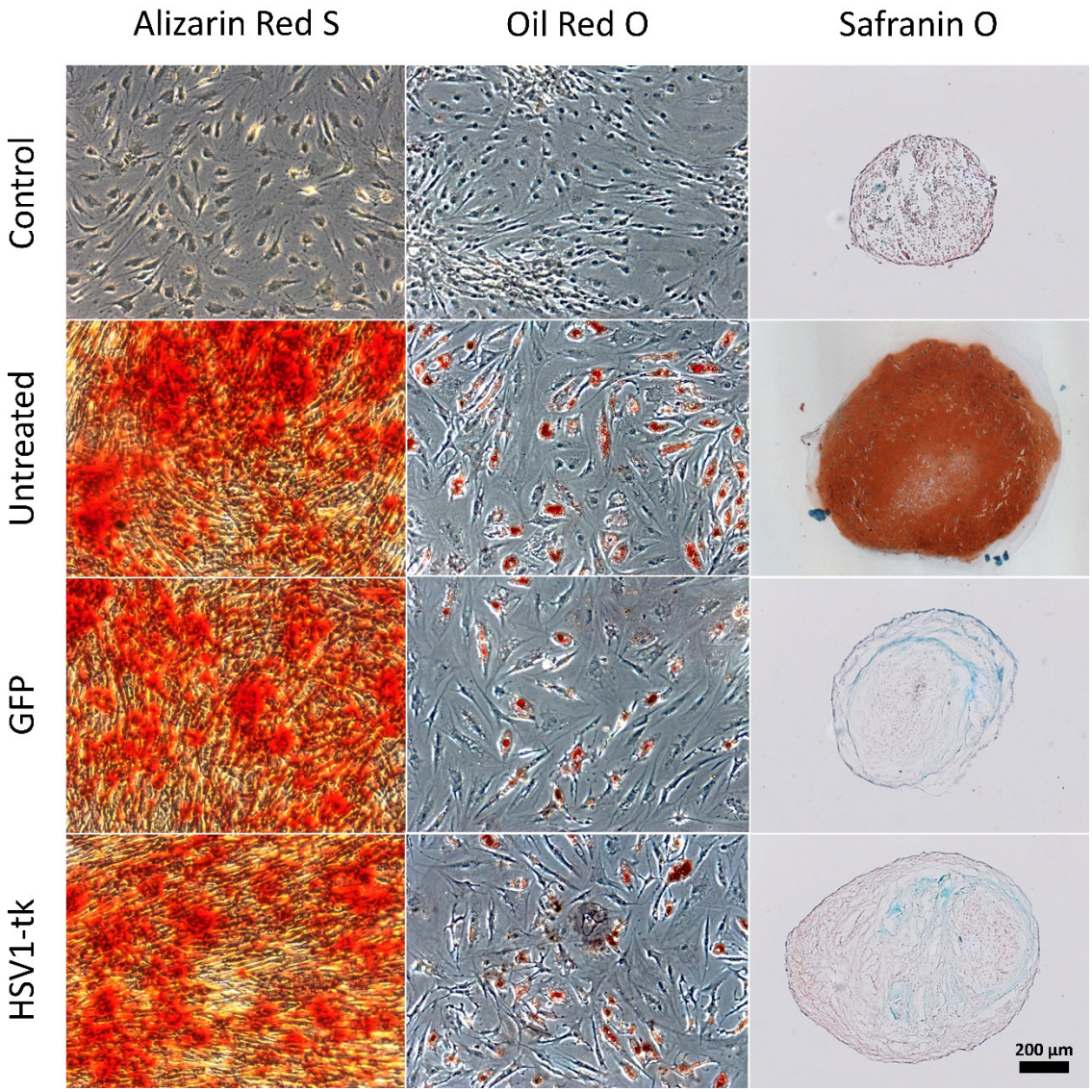


**Figure 5.3**: Qualitative assessments of ASC differentiation post-transduction. Regardless of transduction, ASCs were able to undergo osteogenic and adipogenic differentiation at levels comparable to that of untreated ASCs. Transduction of both GFP and HSV1-tk resulted in decreased ability of ASCs to undergo chondrogenic differentiation.

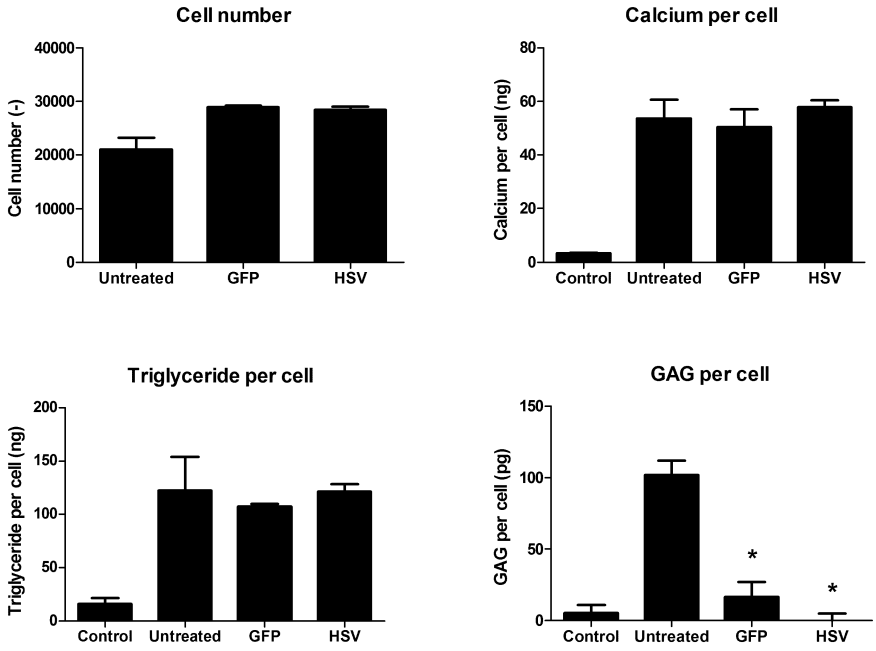


**Figure 5.4**: Quantitative assessments of ASC proliferation and differentiation post-transduction. Transduced ASCs displayed similar cell numbers, calcium per cell, and triglyceride per cell as untreated ASCs, but displayed significantly reduced glycosaminoglycan content per cell compared to untreated ASCs. *$p<0.05$ compared to untreated ASCs.

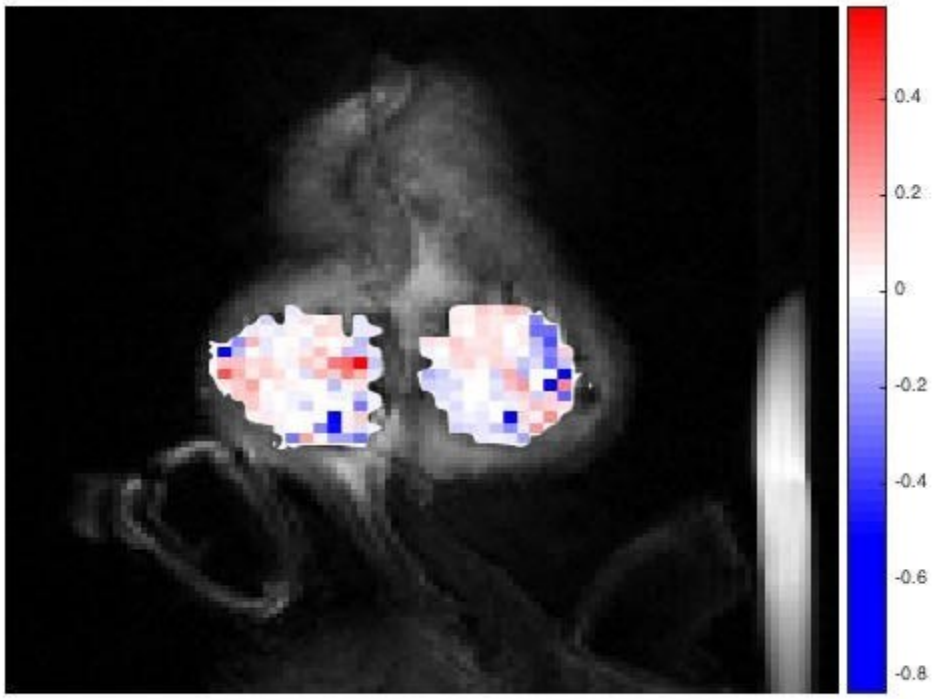


**Figure 5.5**: In vivo CEST-MRI of ASC constructs in murine calvarial defects. The capillary in the image was placed on the mouse's left side. The mouse's right side had ASCs transduced with HSV1-tk, while the mouse's left side had ASCs transduced with GFP. The CEST contrast is quantifiably higher with ASCs transduced with HSV1-tk.

# Chapter 6: future directions

## 6.1. Summary of thesis accomplishments

The goal of this dissertation was to develop a bone engineering approach translatable to the clinic. The first iteration of this approach utilized "gold standards" of the field, marrow-derived bone progenitors and scaffolds derived from native bone. The drawbacks of DCB scaffolds led to the use of 3D printing to create anatomically shaped bioactive hybrid scaffolds composed of DCB within PCL. The drawbacks of eBM and MSCs led to the investigation of ASCs as a cell source and it was shown that PDGF-BB could enhance ASC osteogenesis while not enhancing MSC osteogenesis. This next iteration of the approach – 3D printed scaffolds populated with ASCs – served as a promising new platform for bone regeneration. The CEST-MRI modality was then found suitable for exploring the performance and behavior of this platform post-implantation.

## 6.2. Future directions

The 3D printed hybrid scaffold outlined in Chapter 3 was used in this dissertation to repair a craniofacial defect, but the approach is amenable to other bone defects as well due to the ability of 3D printing to create any anatomical shape and the osteoinductive properties of the hybrid scaffold. For instance, spinal fusion cages and long bone non-unions are other bone defects for which ideal repair solutions do not exist and have clinical trials investigating cell-based approaches [198, 199]. Expanding further, other tissues could be cryo-milled and printed with modified but similar approaches to that outlined in this dissertation.

In Chapter 4, the in vivo effects of PDGF-BB on ASCs were investigated using a transduction model. This model is instructive, but not clinically relevant with current safety concerns. As such, one direction for exploiting the benefits of PDGF-BB on ASCs is developing an in vivo growth factor delivery system. It may be possible to tether PDGF-BB onto the DCB in the scaffold. Alternatively, fibrin-binding fibronectin fragments could be incorporated into the fibrin phase of the construct to bind growth factors, as has been shown previously [200].

Finally, Chapter 5 developed a framework for harnessing the capabilities of CEST-MRI to monitor implanted ASCs. Several directions can come out of the pilot information shown. First, ASCs transduced with HSV1-tk under the CMV promoter, as was done here, can simply be observed under CEST-MRI over a period of time to determine their retention and viability post-implantation. Next, if retention is long enough to allow for direct osteogenic differentiation of ASCs (on the order of a month), a construct where HSV1-tk is under control of an osteogenic promoter, such as osteocalcin, can be transduced into ASCs such that they are only visible under CEST-MRI if they are directly differentiating in vivo. Finally, the spatiotemporal profile of ASCs visualized under CEST-MRI can be correlated with CT, a correlation that can be performed since these two imaging modalities are of similar resolution. If retention is insufficient, it is possible with this imaging modality to determine what strategies may be effective in vivo in bolstering retention to maximize the chance for ASC-mediated osteogenesis.

# References


1. Breeze J, Gibbons AJ, Shieff C, et al. 2011. "Combat-related craniofacial and cervical injuries: a 5-year review from the British military." J Trauma 71: 108-113.
2. Tong D, Beirne R. 2013. "Combat body armor and injuries to the head, face, and neck region: a systematic review." Mil Med 178: 421-426.
3. Parker SE, Mai CT, Canfield MA, et al. 2010. "Updated National Birth Prevalence estimates for selected birth defects in the United States, 2004-2006." Birth Defects Res 88: 1008-1016.
4. Foster RD, Anthony JP, Sharma A, et al. 1999. "Vascularized bone flaps versus nonvascularized bone grafts for mandibular reconstruction: an outcome analysis of primary bony union and endosseous implant success." Head Neck 21: 66-71.
5. Chen YBT, Chen HC, Hahn LH. 1994. "Major mandibular reconstruction with vascularized bone-grafts - indications and selection of donor tissue." Microsurgery 15: 227-237.
6. Schmitz JP, Hollinger JO. 1986. "The critical size defect as an experimental-model for craniomandibulofacial nonunions." Clin Orthop: 299-308.
7. Desai BM. 2007. "Osteobiologics." Am J Orthop 36: 8-11.
8. Champaneria MC, Workman AD, Gupta SC. 2014. "Sushruta: father of plastic surgery." Ann Plast Surg 73: 2-7.
9. Broyles JM, Abt NB, Shridharani SM, et al. 2014. "The fusion of craniofacial reconstruction and microsurgery: a functional and aesthetic approach." Plast Reconstr Surg 134: 760-769.

10. Fisher M, Dorafshar A, Bojovic B, et al. 2012. "The evolution of critical concepts in aesthetic craniofacial microsurgical reconstruction." Plast Reconstr Surg 130: 389-398.

11. Brydone AS, Meek D, Maclaine S. 2011. "Bone grafting, orthopaedic biomaterials, and the clinical need for bone engineering." Proc Inst Mech Eng H 224: 1329-1343.

12. Peled M, El-Naaj IA, Lipin Y, et al. 2005. "The use of free fibular flap for functional mandibular reconstruction." J Oral Maxillofac Surg 63: 220-224.

13. Shan XF, Chen HM, Liang J, et al. 2015. "Surgical reconstruction of maxillary and mandibular defects using a printed titanium mesh." J Oral Maxillofac Surg 73.

14. Aitasalo KMJ, Piitulainen JM, Rekola J, et al. 2014. "Craniofacial bone reconstruction with bioactive fiber-reinforced composite implant." Head Neck 36: 722-728.

15. van Gestel NAP, Geurts J, Hulsen DJW, et al. 2015. "Clinical applications of S53P4 bioactive glass in bone healing and osteomyelitic treatment: a literature review." Biomed Res Int.

16. Fu Q, Saiz E, Tomsia AP. 2011. "Direct ink writing of highly porous and strong glass scaffolds for load-bearing bone defects repair and regeneration." Acta Biomater 7: 3547-3554.

17. Kolan KCR, Leu MC, Hilmas GE, et al. 2011. "Fabrication of 13-93 bioactive glass scaffolds for bone tissue engineering using indirect selective laser sintering." Biofabrication 3: 025004.

18. Jalbert F, Boetto S, Nadon F, et al. 2014. "One-step primary reconstruction for complex craniofacial resection with PEEK custom-made implants." J Craniomaxillofac Surg 42: 141-148.

19. Benzel EC, Thammavaram K, Kesterson L. 1990. "The diagnosis of infections associated with acrylic cranioplasties." Neuroradiology 32: 151-153.

20. Park HK, Dujovny M, Agner C, et al. 2001. "Biomechanical properties of calvarium prosthesis." Neurol Res 23: 267-276.

21. Langer R, Vacanti JP. 1993. "Tissue engineering." Science 260: 920-926.

22. Urist MR. 1965. "Bone: formation by autoinduction." Science 150: 893-899.

23. Urist MR, Mikulski A, Lietze A. 1979. "Solubilized and insolubilized bone morphogenetic protein." Proc Natl Acad Sci U S A 76: 1828-1832.

24. Harakas NK. 1984. "Demineralized bone-matrix-induced osteogenesis." Clin Orthop: 239-251.

25. Mauney JR, Blumberg J, Pirun M, et al. 2004. "Osteogenic differentiation of human bone marrow stromal cells on partially demineralized bone scaffolds in vitro." Tissue Eng 10: 81-92.

26. Mauney JR, Jaquiery C, Volloch V, et al. 2005. "In vitro and in vivo evaluation of differentially demineralized cancellous bone scaffolds combined with human bone marrow stromal cells for tissue engineering." Biomaterials 26: 3173-3185.

27. Lima EG, Mauck RL, Han SH, et al. 2004. "Functional tissue engineering of chondral and osteochondral constructs." Biorheology 41: 577-590.

28. Lima EG, Chao PHG, Ateshian GA, et al. 2008. "The effect of devitalized trabecular bone on the formation of osteochondral tissue-engineered constructs." Biomaterials 29: 4292-4299.

29. Grayson WL, Bhumiratana S, Grace Chao PH, et al. 2010. "Spatial regulation of human mesenchymal stem cell differentiation in engineered osteochondral constructs: effects of pre-differentiation, soluble factors and medium perfusion." Osteoarthritis Cartilage 18: 714-723.

30. Grayson WL, Frohlich M, Yeager K, et al. 2010. "Engineering anatomically shaped human bone grafts." Proc Natl Acad Sci U S A 107: 3299-3304.

31. Pittenger MF, Mackay AM, Beck SC, et al. 1999. "Multilineage potential of adult human mesenchymal stem cells." Science 284: 143-147.

32. Dominici M, Le Blanc K, Mueller I, et al. 2006. "Minimal criteria for defining multipotent mesenchymal stromal cells. The International Society for Cellular Therapy position statement." Cytotherapy 8: 315-317.

33. Sackstein R, Merzaban JS, Cain DW, et al. 2008. "Ex vivo glycan engineering of CD44 programs human multipotent mesenchymal stromal cell trafficking to bone." Nat Med 14: 181-187.

34. Hoogduijn MJ, Gorjup E, Genever PG. 2006. "Comparative characterization of hair follicle dermal stem cells and bone marrow mesenchymal stem cells." Stem Cells Dev 15: 49-60.

35. Barry FP, Boynton RE, Haynesworth S, et al. 1999. "The monoclonal antibody SH-2, raised against human mesenchymal stem cells, recognizes an epitope on endoglin (CD105)." Biochem Biophys Res Commun 265: 134-139.

36. Sampath TK, Reddi AH. 1981. "Dissociative extraction and reconstitution of extracellular matrix components involved in local bone differentiation." Proc Natl Acad Sci U S A 78: 7599-7603.

37. He X, Dziak R, Yuan X, et al. 2013. "BMP2 genetically engineered MSCs and EPCs promote vascularized bone regeneration in rat critical-sized calvarial bone defects." PLoS One 8: e60473.

38. Schofer MD, Roessler PP, Schaefer J, et al. 2011. "Electrospun PLLA nanofiber scaffolds and their use in combination with BMP-2 for reconstruction of bone defects." PLoS One 6.

39. Triplett RG, Nevins M, Marx RE, et al. 2009. "Pivotal, randomized, parallel evaluation of recombinant human Bone Morphogenetic Protein-2/absorbable collagen sponge and autogenous bone graft for maxillary sinus floor augmentation." J Oral Maxillofac Surg 67: 1947-1960.

40. Friedlaender GE, Perry CR, Cole JD, et al. 2001. "Osteogenic protein-1 (bone morphogenetic protein-7) in the treatment of tibial nonunions." J Bone Joint Surg Am 83-A Suppl 1: S151-158.

41. Boden SD, Zdeblick TA, Sandhu HS, et al. 2000. "The use of rhBMP-2 in interbody fusion cages. Definitive evidence of osteoinduction in humans: a preliminary report." Spine 25: 376-381.

42. Howell TH, Fiorellini J, Jones A, et al. 1997. "A feasibility study evaluating rhBMP-2 absorbable collagen sponge device for local alveolar ridge preservation or augmentation." Int J Periodontics Restorative Dent 17: 125-&.

43. Carragee EJ, Hurwitz EL, Weiner BK. 2011. "A critical review of recombinant human bone morphogenetic protein-2 trials in spinal surgery: emerging safety concerns and lessons learned." Spine J 11: 471-491.

44. Salter EK, Goh BC, Hung BP, et al. 2012. "Bone tissue engineering bioreactors: a role in the clinic?" Tissue Eng 18: 62-75.

45. Meirelles Lda S, Fontes AM, Covas DT, et al. 2009. "Mechanisms involved in the therapeutic properties of mesenchymal stem cells." Cytokine Growth Factor Rev 20: 419-427.

46. Wenisch S, Trinkaus K, Hild A, et al. 2005. "Human reaming debris: a source of multipotent stem cells." Bone 36: 74-83.

47. Tydings JD, Martino LJ, Kircher M, et al. 1986. "The osteoinductive potential of intramedullary canal bone reamings." Curr Surg 43: 121-124.

48. Frölke JP, Van de Krol H, Bakker FC, et al. 2000. "Destination of debris during intramedullary reaming. An experimental study on sheep femurs." Acta Orthop Belg 66: 337-340.

49. Hammer TO, Wieling R, Green JM, et al. 2007. "Effect of re-implanted particles from intramedullary reaming on mechanical properties and callus formation. A laboratory study." J Bone Joint Surg Br 89: 1534-1538.

50. Kobbe P, Tarkin IS, Pape HC. 2008. "Use of the 'reamer irrigator aspirator' system for non-infected tibial non-union after failed iliac crest grafting." Injury 39: 796-800.

51. Cox G, McGonagle D, Boxall SA, et al. 2011. "The use of the reamer-irrigator-aspirator to harvest mesenchymal stem cells." J Bone Joint Surg Br 93B: 517-524.

52. Grayson WL, Zhao F, Izadpanah R, et al. 2006. "Effects of hypoxia on human mesenchymal stem cell expansion and plasticity in 3D constructs." J Cell Physiol 207: 331-339.

53. Correia C, Grayson WL, Park M, et al. 2011. "In vitro model of vascularized bone: synergizing vascular development and osteogenesis." PLoS One 6: e28352.

54. Wahl DA, Czernuszka JT. 2006. "Collagen-hydroxyapatite composites for hard tissue repair." Eur Cell Mater 11: 43-56.

55. Clarke KI, Graves SE, Wong ATC, et al. 1993. "Investigation into the formation and mechanical-properties of a bioactive material based on collagen and calcium-phosphate." J Mater Sci 4: 107-110.

56. Serre CM, Papillard M, Chavassieux P, et al. 1993. "In vitro induction of a calcifying matrix by biomaterials constituted of collagen and/or hydroxyapatite: an ultrastructural comparison of three types of biomaterials." Biomaterials 14: 97-106.

57. Yoneno K, Ohno S, Tanimoto K, et al. 2005. "Multidifferentiation potential of mesenchymal stem cells in three-dimensional collagen gel cultures." J Biomed Mater Res 75: 733-741.

58. Porter RM, Liu F, Pilapil C, et al. 2009. "Osteogenic potential of reamer irrigator aspirator (RIA) aspirate collected from patients undergoing hip arthroplasty." J Orthop Res 27: 42-49.

59. Jones EA, English A, Henshaw K, et al. 2004. "Enumeration and phenotypic characterization of synovial fluid multipotential mesenchymal progenitor cells in inflammatory and degenerative arthritis." Arthritis Rheum 50: 817-827.

60. Stolzing A, Jones E, McGonagle D, et al. 2008. "Age-related changes in human bone marrow-derived mesenchymal stem cells: consequences for cell therapies." Mech Ageing Dev 129: 163-173.

61. Khalyfa A, Vogt S, Weisser J, et al. 2007. "Development of a new calcium phosphate powder-binder system for the 3D printing of patient specific implants." J Mater Sci Mater Med 18: 909-916.

62. Inzana JA, Olvera D, Fuller SM, et al. 2014. "3D printing of composite calcium phosphate and collagen scaffolds for bone regeneration." Biomaterials 35: 4026-4034.

63. Williams JM, Adewunmi A, Schek RM, et al. 2005. "Bone tissue engineering using polycaprolactone scaffolds fabricated via selective laser sintering." Biomaterials 26: 4817-4827.

64. Eshraghi S, Das S. 2010. "Mechanical and microstructural properties of polycaprolactone scaffolds with one-dimensional, two-dimensional, and three-dimensional orthogonally oriented porous architectures produced by selective laser sintering." Acta Biomater 6: 2467-2476.

65. Luo Y, Wu C, Lode A, et al. 2013. "Hierarchical mesoporous bioactive glass/alginate composite scaffolds fabricated by three-dimensional plotting for bone tissue engineering." Biofabrication 5: 015005.

66. Serra T, Planell JA, Navarro M. 2013. "High-resolution PLA-based composite scaffolds via 3-D printing technology." Acta Biomater 9: 5521-5530.

67. Seyednejad H, Gawlitta D, Kuiper RV, et al. 2012. "In vivo biocompatibility and biodegradation of 3D-printed porous scaffolds based on a hydroxyl-functionalized poly(epsilon-caprolactone)." Biomaterials 33: 4309-4318.

68. Ang KC, Leong KF, Chua CK, et al. 2007. "Compressive properties and degradability of poly(epsilon-caprolactone)/hydroxyapatite composites under accelerated hydrolytic degradation." J Biomed Mater Res 80: 655-660.

69. Fraser JK, Wulur I, Alfonso Z, et al. 2006. "Fat tissue: an underappreciated source of stem cells for biotechnology." Trends Biotechnol 24: 150-154.

70. Gimble JM, Katz AJ, Bunnell BA. 2007. "Adipose-derived stem cells for regenerative medicine." Circ Res 100: 1249-1260.

71. Zuk PA, Zhu M, Mizuno H, et al. 2001. "Multilineage cells from human adipose tissue: implications for cell-based therapies." Tissue Eng 7: 211-228.

72. Hutton DL, Logsdon EA, Moore EM, et al. 2012. "Vascular morphogenesis of adipose-derived stem cells is mediated by heterotypic cell-cell interactions." Tissue Eng 18: 1729-1740.

73. Hutton DL, Moore EM, Gimble JM, et al. 2013. "Platelet-derived growth factor and spatiotemporal cues induce development of vascularized bone tissue by adipose-derived stem cells." Tissue Eng 19: 2076-2086.

74. Graham S, Leonidou A, Lester M, et al. 2009. "Investigating the role of PDGF as a potential drug therapy in bone formation and fracture healing." Expert Opin Investig Drugs 18: 1633-1654.

75. Gehmert S, Hidayat M, Sultan M, et al. 2011. "Angiogenesis: the role of PDGF-BB on adipose-tissue derived stem cells (ASCs)." Clin Hemorheol Microcirc 48: 5-13.

76. Lindahl P, Hellstrom M, Kalen M, et al. 1998. "Endothelial-perivascular cell signaling in vascular development: lessons from knockout mice." Curr Opin Lipidol 9: 407-411.

77. Lam CX, Hutmacher DW, Schantz JT, et al. 2009. "Evaluation of polycaprolactone scaffold degradation for 6 months in vitro and in vivo." J Biomed Mater Res 90: 906-919.

78. Saito E, Liao EE, Hu WW, et al. 2013. "Effects of designed PLLA and 50:50 PLGA scaffold architectures on bone formation in vivo." J Tissue Eng Regen Med 7: 99-111.

79. Yilgor P, Hasirci N, Hasirci V. 2010. "Sequential BMP-2/BMP-7 delivery from polyester nanocapsules." J Biomed Mater Res 93: 528-536.

80. Oliveira JM, Silva SS, Malafaya PB, et al. 2009. "Macroporous hydroxyapatite scaffolds for bone tissue engineering applications: physicochemical characterization and assessment of rat bone marrow stromal cell viability." J Biomed Mater Res 91: 175-186.

81. Azami M, Samadikuchaksaraei A, Poursamar SA. 2010. "Synthesis and characterization of a laminated hydroxyapatite/gelatin nanocomposite scaffold with controlled pore structure for bone tissue engineering." Int J Artif Organs 33: 86-95.

82. Umeda H, Kanemaru S, Yamashita M, et al. 2007. "Bone regeneration of canine skull using bone marrow-derived stromal cells and beta-tricalcium phosphate." Laryngoscope 117: 997-1003.

83. Nienhuijs MEL, Walboomers XF, Briest A, et al. 2010. "Healing of bone defects in the goat mandible, using COLLOSS (R) E and beta-tricalciumphosphate." J Biomed Mater Res 92B: 517-524.

84. Baas J, Elmengaard B, Bechtold J, et al. 2008. "Ceramic bone graft substitute with equine bone protein extract is comparable to allograft in terms of implant fixation: a study in dogs." Acta Orthopaedica 79: 841-850.

85. Hung BP, Salter EK, Temple J, et al. 2013. "Engineering bone grafts with enhanced bone marrow and native scaffolds." Cells Tissues Organs 198: 87-98.

86. Temple JP, Hutton DL, Hung BP, et al. 2014. "Engineering anatomically shaped vascularized bone grafts with hASCs and 3D-printed PCL scaffolds." J Biomed Mater Res 102: 4317-4325.

87. Sathyavathi R, Saha A, Soares JS, et al. 2015. "Raman spectroscopic sensing of carbonate intercalation in breast microcalcifications at stereotactic biopsy." Scientific Reports 5: 9907.

88. Hung BP, Babalola OM, Bonassar LJ. 2013. "Quantitative characterization of mesenchymal stem cell adhesion to the articular cartilage surface." J Biomed Mater Res 101: 3592-3598.

89. Reyes CD, Garcia AJ. 2003. "A centrifugation cell adhesion assay for high-throughput screening of biomaterial surfaces." J Biomed Mater Res 67: 328-333.

90. Sauermann W, Feuerstein TJ. 1998. "Some mathematical models for concentration-response relationships." Biometrical J 40: 865-881.

91. Feuerstein TJ, Limberger N. 1999. "Mathematical analysis of the control of neurotransmitter release by presynaptic receptors as a supplement to experimental data." Naunyn Schmiedebergs Arch Pharmacol 359: 345-359.

92. Estes BT, Diekman BO, Gimble JM, et al. 2010. "Isolation of adipose-derived stem cells and their induction to a chondrogenic phenotype." Nat Protoc 5: 1294-1311.

93. Hutton DL, Kondragunta R, Moore EM, et al. 2014. "Tumor Necrosis Factor improves vascularization in osteogenic grafts engineered with human adipose-derived stem/stromal cells." PLoS One 9: e107199.

94. Cowan CM, Shi YY, Aalami OO, et al. 2004. "Adipose-derived adult stromal cells heal critical-size mouse calvarial defects." Nat Biotechnol 22: 560-567.

95. Gupta DM, Kwan MD, Slater BJ, et al. 2008. "Applications of an athymic nude mouse model of nonhealing critical-sized calvarial defects." J Craniofac Surg 19: 192-197.

96. Mandair GS, Morris MD. 2015. "Contributions of Raman spectroscopy to the understanding of bone strength." BoneKEy reports 4: 620.

97. Taddei P, Tinti A, Reggiani M, et al. 2005. "In vitro mineralization of bioresorbable poly(epsilon-caprolactone)/apatite composites for bone tissue engineering: a vibrational and thermal investigation." Journal of Molecular Structure 744: 135-143.

98. Kister G, Cassanas G, Bergounhon M, et al. 2000. "Structural characterization and hydrolytic degradation of solid copolymers of D,L-lactide-co-epsilon-caprolactone by Raman spectroscopy." Polymer 41: 925-932.

99. Dalby MJ, Gadegaard N, Tare R, et al. 2007. "The control of human mesenchymal cell differentiation using nanoscale symmetry and disorder." Nat Mater 6: 997-1003.

100. McNamara LE, McMurray RJ, Biggs MJ, et al. 2010. "Nanotopographical control of stem cell differentiation." Journal of Tissue Engineering 2010: 120623.

101. Hung BP, Hutton DL, Grayson WL. 2013. "Mechanical control of tissue-engineered bone." Stem Cell Res Ther 4: 10.

102. Goldstein SA. 1987. "The mechanical properties of trabecular bone: dependence on anatomic location and function." J Biomech 20: 1055-1061.

103. Zein I, Hutmacher DW, Tan KC, et al. 2002. "Fused deposition modeling of novel scaffold architectures for tissue engineering applications." Biomaterials 23: 1169-1185.

104. Zhou YF, Hutmacher DW, Varawan SL, et al. 2007. "In vitro bone engineering based on polycaprolactone and polycaprolactone-tricalcium phosphate composites." Polymer International 56: 333-342.

105. Deligianni DD, Katsala ND, Koutsoukos PG, et al. 2001. "Effect of surface roughness of hydroxyapatite on human bone marrow cell adhesion, proliferation, differentiation and detachment strength." Biomaterials 22: 87-96.

106. Sawyer AA, Song SJ, Susanto E, et al. 2009. "The stimulation of healing within a rat calvarial defect by mPCL-TCP/collagen scaffolds loaded with rhBMP-2." Biomaterials 30: 2479-2488.

107. Wang YK, Yu X, Cohen DM, et al. 2012. "Bone morphogenetic protein-2-induced signaling and osteogenesis is regulated by cell shape, RhoA/ROCK, and cytoskeletal tension." Stem Cells Dev 21: 1176-1186.

108. Bhumiratana S, Grayson WL, Castaneda A, et al. 2011. "Nucleation and growth of mineralized bone matrix on silk-hydroxyapatite composite scaffolds." Biomaterials 32: 2812-2820.

109. Stoppato M, Carletti E, Sidarovich V, et al. 2013. "Influence of scaffold pore size on collagen I development: A new in vitro evaluation perspective." J Bioact Compat Pol 28: 16-32.

110. Suwanprateeb J, Sanngam R, Suvannapruk W, et al. 2009. "Mechanical and in vitro performance of apatite-wollastonite glass ceramic reinforced hydroxyapatite composite fabricated by 3D-printing." J Mater Sci Mater Med 20: 1281-1289.

111. Pountos I, Georgouli T, Henshaw K, et al. 2013. "Release of growth factors and the effect of age, sex, and severity of injury after long bone fracture. A preliminary report." Acta Orthopaedica 84: 65-70.

112. Caplan AI, Correa D. 2011. "PDGF in bone formation and regeneration: new insights into a novel mechanism involving MSCs." J Orthop Res 29: 1795-1803.

113. Yu X, Hsieh SC, Bao W, et al. 1997. "Temporal expression of PDGF receptors and PDGF regulatory effects on osteoblastic cells in mineralizing cultures." Am J Physiol 272: C1709-1716.

114. Park SY, Kim KH, Shin SY, et al. 2013. "Dual delivery of rhPDGF-BB and bone marrow mesenchymal stromal cells expressing the BMP2 gene enhance bone formation in a critical-sized defect model." Tissue Eng 19: 2495-2505.

115. Kratchmarova I, Blagoev B, Haack-Sorensen M, et al. 2005. "Mechanism of divergent growth factor effects in mesenchymal stem cell differentiation." Science 308: 1472-1477.

116. Gruber R, Karreth F, Kandler B, et al. 2004. "Platelet-released supernatants increase migration and proliferation, and decrease osteogenic differentiation of bone marrow-derived mesenchymal progenitor cells under in vitro conditions." Platelets 15: 29-35.

117. Tokunaga A, Oya T, Ishii Y, et al. 2008. "PDGF receptor beta is a potent regulator of mesenchymal stromal cell function." J Bone Miner Res 23: 1519-1528.

118. Vila OF, Martino MM, Nebuloni L, et al. 2014. "Bioluminescent and micro-computed tomography imaging of bone repair induced by fibrin-binding growth factors." Acta Biomater 10: 4377-4389.

119. Hollinger JO, Hart CE, Hirsch SN, et al. 2008. "Recombinant human platelet-derived growth factor: biology and clinical applications." J Bone Joint Surg Am 90 Suppl 1: 48-54.

120. Whitehead KA, Langer R, Anderson DG. 2009. "Knocking down barriers: advances in siRNA delivery." Nat Rev Drug Discov 8: 129-138.

121. Oh YK, Park TG. 2009. "siRNA delivery systems for cancer treatment." Adv Drug Deliv Rev 61: 850-862.

122. Semple SC, Akinc A, Chen J, et al. 2010. "Rational design of cationic lipids for siRNA delivery." Nat Biotechnol 28: 172-176.

123. Huang L, Liu Y. 2011. "In vivo delivery of RNAi with lipid-based nanoparticles." Annu Rev Biomed Eng 13: 507-530.

124. Spagnou S, Miller AD, Keller M. 2004. "Lipidic carriers of siRNA: differences in the formulation, cellular uptake, and delivery with plasmid DNA." Biochemistry (Mosc) 43: 13348-13356.

125. Adair JH, Parette MP, Altinoglu EI, et al. 2010. "Nanoparticulate alternatives for drug delivery." ACS Nano 4: 4967-4970.

126. Sutton D, Kim S, Shuai X, et al. 2006. "Efficient suppression of secretory clusterin levels by polymer-siRNA nanocomplexes enhances ionizing radiation lethality in human MCF-7 breast cancer cells in vitro." Int J Nanomedicine 1: 155-162.

127. Breunig M, Hozsa C, Lungwitz U, et al. 2008. "Mechanistic investigation of poly(ethylene imine)-based siRNA delivery: disulfide bonds boost intracellular release of the cargo." J Controlled Release 130: 57-63.

128. Giljohann DA, Seferos DS, Prigodich AE, et al. 2009. "Gene regulation with polyvalent siRNA-nanoparticle conjugates." J Am Chem Soc 131: 2072-2073.

129. Green JJ, Langer R, Anderson DG. 2008. "A combinatorial polymer library approach yields insight into nonviral gene delivery." Acc Chem Res 41: 749-759.

130. Bhise NS, Gray RS, Sunshine JC, et al. 2010. "The relationship between terminal functionalization and molecular weight of a gene delivery polymer and

transfection efficacy in mammary epithelial 2-D cultures and 3-D organotypic cultures." Biomaterials 31: 8088-8096.

131. Tzeng SY, Yang PH, Grayson WL, et al. 2012. "Synthetic poly(ester amine) and poly(amido amine) nanoparticles for efficient DNA and siRNA delivery to human endothelial cells." Int J Nanomedicine 6: 3309-3322.

132. Sunshine J, Green JJ, Mahon KP, et al. 2009. "Small-molecule end-groups of linear polymer determine cell-type gene-delivery efficacy." Adv Mater 21: 4947-4951.

133. Lee JS, Green JJ, Love KT, et al. 2009. "Gold, poly(beta-amino ester) nanoparticles for small interfering RNA delivery." Nano Lett 9: 2402-2406.

134. Jere D, Xu CX, Arote R, et al. 2008. "Poly(beta-amino ester) as a carrier for si/shRNA delivery in lung cancer cells." Biomaterials 29: 2535-2547.

135. Vandenbroucke RE, De Geest BG, Bonne S, et al. 2008. "Prolonged gene silencing in hepatoma cells and primary hepatocytes after small interfering RNA delivery with biodegradable poly(beta-amino esters)." J Gene Med 10: 783-794.

136. Singh N, Agrawal A, Leung AK, et al. 2010. "Effect of nanoparticle conjugation on gene silencing by RNA interference." J Am Chem Soc 132: 8241-8243.

137. LeDuc PR, Messner WC, Wikswo JP. 2011. "How do control-based approaches enter into biology?" Annu Rev Biomed Eng 13: 369-396.

138. Tzeng SY, Guerrero-Cazares H, Martinez EE, et al. 2011. "Non-viral gene delivery nanoparticles based on poly(beta-amino esters) for treatment of glioblastoma." Biomaterials 32: 5402-5410.

139. Sunshine JC, Akanda MI, Li D, et al. 2011. "Effects of base polymer hydrophobicity and end-group modification on polymeric gene delivery." Biomacromolecules 12: 3592-3600.

140. Bhise NS, Shmueli RB, Gonzalez J, et al. 2012. "A novel assay for quantifying the number of plasmids encapsulated by polymer nanoparticles." Small 8: 367-373.

141. Meister A, Anderson ME. 1983. "Glutathione." Annu Rev Biochem 52: 711-760.

142. Filipe V, Hawe A, Jiskoot W. 2010. "Critical evaluation of Nanoparticle Tracking Analysis (NTA) by NanoSight for the measurement of nanoparticles and protein aggregates." Pharm Res 27: 796-810.

143. Green JJ, Zhou BY, Mitalipova MM, et al. 2008. "Nanoparticles for gene transfer to human embryonic stem cell colonies." Nano Lett 8: 3126-3130.

144. Eltoukhy AA, Siegwart DJ, Alabi CA, et al. 2012. "Effect of molecular weight of amine end-modified poly(beta-amino ester)s on gene delivery efficiency and toxicity." Biomaterials 33: 3594-3603.

145. Yau WW, Rujitanaroj PO, Lam L, et al. 2012. "Directing stem cell fate by controlled RNA interference." Biomaterials 33: 2608-2628.

146. Chen Y, Cong L, Yin X, et al. 2011. "The culture of temporary tumor-like bone marrow mesenchymal stem cells (TT-BMSC) and the detection of cell biology property." Ann Transplant 16: 49-58.

147. Tao W, Davide JP, Cai M, et al. 2010. "Noninvasive imaging of lipid nanoparticle-mediated systemic delivery of small-interfering RNA to the liver." Mol Ther 18: 1657-1666.

148. Spelios M, Kearns M, Savva M. 2010. "From gene delivery to gene silencing: plasmid DNA-transfecting cationic lipid 1,3-dimyristoylamidopropane-2-[bis(2-dimethylaminoethane)] carbamate efficiently promotes small interfering RNA-induced RNA interference." Biochemistry (Mosc) 49: 5753-5759.

149. Andersen MO, Nygaard JV, Burns JS, et al. 2010. "siRNA nanoparticle functionalization of nanostructured scaffolds enables controlled multilineage differentiation of stem cells." Mol Ther 18: 2018-2027.

150. Jones DP, Carlson JL, Samiec PS, et al. 1998. "Glutathione measurement in human plasma. Evaluation of sample collection, storage and derivatization conditions for analysis of dansyl derivatives by HPLC." Clin Chim Acta 275: 175-184.

151. Anderson DG, Akinc A, Hossain N, et al. 2005. "Structure/property studies of polymeric gene delivery using a library of poly(beta-amino esters)." Mol Ther 11: 426-434.

152. Gary DJ, Puri N, Won YY. 2007. "Polymer-based siRNA delivery: perspectives on the fundamental and phenomenological distinctions from polymer-based DNA delivery." J Controlled Release 121: 64-73.

153. Luo D, Saltzman WM. 2000. "Synthetic DNA delivery systems." Nat Biotechnol 18: 33-37.

154. Hoon Jeong J, Christensen LV, Yockman JW, et al. 2007. "Reducible poly(amido ethylenimine) directed to enhance RNA interference." Biomaterials 28: 1912-1917.

155. Won YW, Yoon SM, Lee KM, et al. 2011. "Poly(oligo-D-arginine) with internal disulfide linkages as a cytoplasm-sensitive carrier for siRNA delivery." Mol Ther 19: 372-380.

156. Park K, Lee MY, Kim KS, et al. 2010. "Target specific tumor treatment by VEGF siRNA complexed with reducible polyethyleneimine-hyaluronic acid conjugate." Biomaterials 31: 5258-5265.

157. Jaiswal N, Haynesworth SE, Caplan AI, et al. 1997. "Osteogenic differentiation of purified, culture-expanded human mesenchymal stem cells in vitro." J Cell Biochem 64: 295-312.

158. Worster AA, Nixon AJ, Brower-Toland BD, et al. 2000. "Effect of transforming growth factor beta1 on chondrogenic differentiation of cultured equine mesenchymal stem cells." Am J Vet Res 61: 1003-1010.

159. Kozielski KL, Tzeng SY, Green JJ. 2013. "A bioreducible linear poly(beta-amino ester) for siRNA delivery." Chem Commun 49: 5319-5321.

160. Kozielski KL, Tzeng SY, De Mendoza BAH, et al. 2014. "Bioreducible cationic polymer-based nanoparticles for efficient and environmentally triggered cytoplasmic siRNA delivery to primary human brain cancer cells." ACS Nano 8: 3232-3241.

161. Yang X, Boehm JS, Salehi-Ashtiani K, et al. 2011. "A public genome-scale lentiviral expression library of human ORFs." Nat Methods 8: 659-661.

162. Mosna F, Sensebe L, Krampera M. 2010. "Human bone marrow and adipose tissue mesenchymal stem cells: a user's guide." Stem Cells Dev 19: 1449-1470.

163. Gronthos S, Franklin DM, Leddy HA, et al. 2001. "Surface protein characterization of human adipose tissue-derived stromal cells." J Cell Physiol 189: 54-63.

164. Kern S, Eichler H, Stoeve J, et al. 2006. "Comparative analysis of mesenchymal stem cells from bone marrow, umbilical cord blood, or adipose tissue." Stem Cells 24: 1294-1301.

165. Noel D, Caton D, Roche S, et al. 2008. "Cell specific differences between human adipose-derived and mesenchymal-stromal cells despite similar differentiation potentials." Exp Cell Res 314: 1575-1584.

166. Sakaguchi Y, Sekiya I, Yagishita K, et al. 2005. "Comparison of human stem cells derived from various mesenchymal tissues - Superiority of synovium as a cell source." Arthritis Rheum 52: 2521-2529.

167. Pachon-Pena G, Yu G, Tucker A, et al. 2011. "Stromal stem cells from adipose tissue and bone marrow of age-matched female donors display distinct immunophenotypic profiles." J Cell Physiol 226: 843-851.

168. Kim HJ, Im GI. 2009. "Chondrogenic differentiation of adipose tissue-derived mesenchymal stem cells: greater doses of growth factor are necessary." J Orthop Res 27: 612-619.

169. Liu TM, Martina M, Hutmacher DW, et al. 2007. "Identification of common pathways mediating differentiation of bone marrow- and adipose tissue-derived human mesenchymal stem cells into three mesenchymal lineages." Stem Cells 25: 750-760.

170. Boquest AC, Noer A, Collas P. 2006. "Epigenetic programming of mesenchymal stem cells from human adipose tissue." Stem Cell Rev 2: 319-329.

171. Arnsdorf EJ, Tummala P, Castillo AB, et al. 2010. "The epigenetic mechanism of mechanically induced osteogenic differentiation." J Biomech 43: 2881-2886.

172. Maes C, Kobayashi T, Selig MK, et al. 2010. "Osteoblast precursors, but not mature osteoblasts, move into developing and fractured bones along with invading blood vessels." Dev Cell 19: 329-344.

173. Mikos AG, Herring SW, Ochareon P, et al. 2006. "Engineering complex tissues." Tissue Eng 12: 3307-3339.

174. Carano RAD, Filvaroff EH. 2003. "Angiogenesis and bone repair." Drug Discovery Today 8: 980-989.

175. Giannoudis PV, Pountos I, Morley J, et al. 2008. "Growth factor release following femoral nailing." Bone 42: 751-757.

176. Allay JA, Dennis JE, Haynesworth SE, et al. 1997. "LacZ and interleukin-3 expression in vivo after retroviral transduction of marrow-derived human osteogenic mesenchymal progenitors." Hum Gene Ther 8: 1417-1427.

177. Dupont KM, Sharma K, Stevens HY, et al. 2010. "Human stem cell delivery for treatment of large segmental bone defects." Proc Natl Acad Sci U S A 107: 3305-3310.

178. Kang HW, Lee SJ, Ko IK, et al. 2016. "A 3D bioprinting system to produce human-scale tissue constructs with structural integrity." Nat Biotechnol.

179. Villa MM, Wang LP, Huang JP, et al. 2015. "Bone tissue engineering with a collagen-hydroxyapatite scaffold and culture expanded bone marrow stromal cells." J Biomed Mater Res 103: 243-253.

180. Contag CH, Bachmann MH. 2002. "Advances in in vivo bioluminescence imaging of gene expression." Annu Rev Biomed Eng 4: 235-260.

181. Boutroy S, Bouxsein ML, Munoz F, et al. 2005. "In vivo assessment of trabecular bone microarchitecture by high-resolution peripheral quantitative computed tomography." J Clin Endocrinol Metab 90: 6508-6515.

182. Cook CA, Hahn KC, Morrissette-McAlmon JB, et al. 2015. "Oxygen delivery from hyperbarically loaded microtanks extends cell viability in anoxic environments." Biomaterials 52: 376-384.

183. Anzai Y, McLachlan S, Morris M, et al. 1994. "Dextran-coated superparamagnetic iron oxide, an MR contrast agent for assessing lymph nodes in the head and neck." AJNR Am J Neuroradiol 15: 87-94.

184. So PW, Kalber T, Hunt D, et al. 2010. "Efficient and rapid labeling of transplanted cell populations with superparamagnetic iron oxide nanoparticles using cell surface chemical biotinylation for in vivo monitoring by MRI." Cell Transplant 19: 419-429.

185. Ngen EJ, Wang L, Kato Y, et al. 2015. "Imaging transplanted stem cells in real time using an MRI dual-contrast method." Scientific Reports 5.

186. Gruttner C, Muller K, Teller J, et al. 2007. "Synthesis and antibody conjugation of magnetic nanoparticles with improved specific power absorption rates for alternating magnetic field cancer therapy." J Magn Magn Mater 311: 181-186.

187. Chang YK, Liu YP, Ho JH, et al. 2012. "Amine-surface-modified superparamagnetic iron oxide nanoparticles interfere with differentiation of human mesenchymal stem cells." J Orthop Res 30: 1499-1506.

188. Terrovitis J, Stuber M, Youssef A, et al. 2008. "Magnetic resonance imaging overestimates ferumoxide-labeled stem cell survival after transplantation in the heart." Circulation 117: 1555-1562.

189. Sadikot RT, Blackwell TS. 2005. "Bioluminescence imaging." Proc Am Thorac Soc 2: 537-540, 511-532.

190. McMahon MT, Gilad AA, DeLiso MA, et al. 2008. "New "Multicolor" polypeptide diamagnetic chemical exchange saturation transfer (DIACEST) contrast agents for MRI." Magn Reson Med 60: 803-812.

191. Ward KM, Aletras AH, Balaban RS. 2000. "A new class of contrast agents for MRI based on proton chemical exchange dependent saturation transfer (CEST)." J Magn Reson 143: 79-87.

192. Gilad AA, McMahon MT, Walczak P, et al. 2007. "Artificial reporter gene providing MRI contrast based on proton exchange." Nat Biotechnol 25: 217-219.

193. Bar-Shir A, Liu GS, Greenberg MM, et al. 2013. "Synthesis of a probe for monitoring HSV1-tk reporter gene expression using chemical exchange saturation transfer MRI." Nat Protoc 8: 2380-2391.

194. Bar-Shir A, Liu GS, Liang YJ, et al. 2013. "Transforming thymidine into a magnetic resonance imaging probe for monitoring gene expression." J Am Chem Soc 135: 1617-1624.

195. Tzeng SY, Hung BP, Grayson WL, et al. 2012. "Cystamine-terminated poly(beta-amino ester)s for siRNA delivery to human mesenchymal stem cells and enhancement of osteogenic differentiation." Biomaterials 33: 8142-8151.

196. Hung BP, Hutton DL, Kozielski KL, et al. 2015. "Platelet-derived growth factor BB enhances osteogenesis of adipose-derived but not bone marrow-derived mesenchymal stromal/stem cells." Stem Cells 33: 2773-2784.

197. Lin P, Lin Y, Lennon DP, et al. 2012. "Efficient lentiviral transduction of human mesenchymal stem cells that preserves proliferation and differentiation capabilities." Stem Cells Transl Med 1: 886-897.

198. Liebergall M, Schroeder J, Mosheiff R, et al. 2013. "Stem cell-based therapy for prevention of delayed fracture union: a randomized and prospective preliminary study." Mol Ther 21: 1631-1638.

199. Hart R, Komzak M, Okal F, et al. 2014. "Allograft alone versus allograft with bone marrow concentrate for the healing of the instrumented posterolateral lumbar fusion." Spine J 14: 1318-1324.

200. Martino MM, Tortelli F, Mochizuki M, et al. 2011. "Engineering the growth factor microenvironment with fibronectin domains to promote wound and bone tissue healing." Sci Transl Med 3: 100ra189.

# Vita

Ben Pen Jui Hung, known as the very best, like no-one ever was, was born on November 19, 1987 in Taipei, Taiwan. He moved to the United States in 1990 and has lived in Alhambra, CA; Nogales, AZ; El Paso, TX; Huntley, IL; Cypress, TX; and Indianapolis, IN. He attended Cypress Creek High School in Houston, TX from 2001 to 2005 and developed an interest in many different scientific and mathematic fields. As such, upon acceptance into Cornell University at the end of high school, he chose to pursue biological engineering, an extremely interdisciplinary field that would encourage him to study and integrate the many different areas of science and mathematics.

During his time at Cornell University, he grew to believe in tissue engineering as a new technology that could revolutionize medicine. He was especially interested in cartilage engineering and, to that end, researched the potential of cell-based therapies against osteoarthritis in Lawrence Bonassar's laboratory from 2006 to 2010. In 2009 he graduated with a Bachelor's of Science in Biological Engineering with a Biomedical Engineering minor and then in 2010 he obtained his Master's of Engineering in Biomedical Engineering, also from Cornell University.

In 2010 he began his doctoral studies at Johns Hopkins University, choosing this institution due to its strong focus on clinically translatable technologies. He is set to graduate with a Doctor of Philosophy degree in Biomedical Engineering in 2016, having achieved the accomplishments chronicled within this dissertation.